

12-1-2017

AN EXPERIMENTAL STUDY OF THE
EFFECTS OF SUBSTRATE POROSITY,
MORPHOLOGY, AND FLEXIBILITY ON
THE EQUILIBRIUM THERMODYNAMICS
AND KINETICS OF ADSORPTION FOR
ATOMIC AND MOLECULAR ADSORBATES

Brice Adam Russell

Southern Illinois University Carbondale, brussell85@outlook.com

Follow this and additional works at: <http://opensiuc.lib.siu.edu/dissertations>

Recommended Citation

Russell, Brice Adam, "AN EXPERIMENTAL STUDY OF THE EFFECTS OF SUBSTRATE POROSITY, MORPHOLOGY, AND FLEXIBILITY ON THE EQUILIBRIUM THERMODYNAMICS AND KINETICS OF ADSORPTION FOR ATOMIC AND MOLECULAR ADSORBATES" (2017). *Dissertations*. 1490.

<http://opensiuc.lib.siu.edu/dissertations/1490>

This Open Access Dissertation is brought to you for free and open access by the Theses and Dissertations at OpenSIUC. It has been accepted for inclusion in Dissertations by an authorized administrator of OpenSIUC. For more information, please contact opensiuc@lib.siu.edu.

AN EXPERIMENTAL STUDY OF THE EFFECTS OF SUBSTRATE POROSITY, MORPHOLOGY, AND
FLEXIBILITY ON THE EQUILIBRIUM THERMODYNAMICS AND KINETICS OF ADSORPTION FOR
ATOMIC AND MOLECULAR ADSORBATES

by

Brice Adam Russell

B.S., Southern Illinois University, 2011

M.S., Southern Illinois University, 2013

A Dissertation

Submitted in Partial Fulfillment of the Requirements for the
Doctor of Philosophy Degree in Applied Physics

Department of Physics

in the Graduate School

Southern Illinois University Carbondale

December 2017

DISSERTATION APPROVAL

AN EXPERIMENTAL STUDY OF THE EFFECTS OF SUBSTRATE POROSITY, MORPHOLOGY, AND FLEXIBILITY ON THE EQUILIBRIUM THERMODYNAMICS AND KINETICS OF ADSORPTION FOR ATOMIC AND MOLECULAR ADSORBATES

By

Brice Adam Russell

A Dissertation Submitted in Partial
Fulfillment of the Requirements
for the Degree of
Doctor of Philosophy
in the Field of Applied Physics

Approved by:

Dr. Aldo D. Migone, Chair

Dr. Saikat Talapatra

Dr. M. Mercedes Calbi

Dr. Thushari Jayasekera

Dr. Dipanjan Mazumdar

Graduate School

Southern Illinois University Carbondale

July 2017

AN ABSTRACT OF THE DISSERTATION OF

BRICE ADAM RUSSELL, for the Doctor of Philosophy degree in APPLIED PHYSICS, presented on July 14 2017, at Southern University Carbondale.

TITLE: AN EXPERIMENTAL STUDY OF THE EFFECTS OF SUBSTRATE POROSITY, MORPHOLOGY, AND FLEXIBILITY ON THE EQUILIBRIUM THERMODYNAMICS AND KINETICS OF ADSORPTION FOR ATOMIC AND MOLECULAR ADSORBATES

MAJOR PROFESSOR: Dr. Aldo D. Migone

Five systems consisting of different sorbate-sorbent combinations were studied using experimental volumetric adsorption techniques. Multiple adsorption isotherms were measured at low temperatures and low pressures for all of the systems studied which included CO₂ adsorption on single walled carbon nanotubes (CO₂ – SWCNT), Ethane adsorption on closed carbon nanohorns (Ethane-cNH), Ar adsorption on open carbon nanohorns (Ar – oNH), CO₂ adsorption on zeolitic imidazolate framework-8 (CO₂ – ZIF-8), and O₂ adsorption on ZIF-8 (O₂ – ZIF-8). Each of these systems offers a unique study of the relationship between the physical properties of the adsorbate and substrate and the effects of these properties on the thermodynamics and kinetics of adsorption. In addition to being of fundamental interest, the thermodynamics and kinetics of adsorption are important to understand for practical considerations in research fields such as gas storage and gas separation via adsorption processes, among other applications.

CO₂ – SWCNT is a system with a small linear molecular adsorbate with a permanent quadrupole moment adsorbing on a substrate with quasi-1D grooves and convex outer adsorption sites. Ethane-cNH is a system with a linear alkane adsorbing on a substrate with conical pores and convex outer adsorption sites. Ar – oNH is a system with a spherical atom sorbing in a substrate with two different groups of conical adsorption sites and both convex and concave surface sites. CO₂ – ZIF-8 and O₂ – ZIF-8 are both systems with small linear molecules sorbing in a flexible microporous scaffold-like substrate.

Adsorption isotherms were analyzed to identify features corresponding to adsorbate-adsorbate and adsorbate-substrate interactions. Namely, the presence of substeps in the semi-logarithmic data were identified and interpreted to correspond to groups of adsorption sites of similar binding energy which likely depend on the morphology and/or structural flexibility of the substrates. All of the systems, with the exception of CO₂ - SWCNTs, yielded at least some isotherms with substeps at pressures below that corresponding to saturation. Effective specific surface areas for all adsorbent-substrate combinations were calculated using the BET and Point-B methods for the sake of comparison. These surface area measurements are very dependent on the porosity and morphology of the substrate as well as the size and shape of the adsorbate atoms/molecules and therefore the values vary greatly between the different systems. The isosteric heat of adsorption was calculated using isotherms over the full range of temperatures for each system. A variant of the Clausius-Clapeyron equation was used for this purpose and the results were analyzed based on adsorbate-adsorbate and adsorbate-substrate interactions. Plateaus in the isosteric heat data for Ethane – cNH and Ar – oNH were related to the morphology of the substrates and properties of the adsorbate species. For CO₂ – SWCNTs, the isosteric heat at all but the lowest coverages is below the latent heat of deposition. This is due to the quadrupole moment of CO₂. For both of the studies of adsorption on ZIF-8, the isosteric heat contains peaks in the data which likely are the result of the flexibility of the ZIF-8 structure. The kinetics of adsorption (or, the rates at which the adsorption systems approach equilibrium) were analyzed as functions of isotherm temperature and coverage, vapor pressure, and fractional uptake point by point along individual isotherms using the linear driving force model. Certain trends in the kinetics of adsorption are consistent for all the systems studied and others vary depending on the specific adsorbate-substrate combination. As with the thermodynamic results, trends in the kinetics of adsorption are discussed in terms of the effects of adsorbate-adsorbate and adsorbate-substrate interactions.

ACKNOWLEDGEMENTS

I must express utmost gratitude and appreciation to my research advisor, Professor Aldo Migone. Without his encouragement to do graduate research in his lab, I might never have even considered pursuing physics beyond the bachelor's degree. The skills and knowledge I've gained and the career opportunities that have potentially opened up to me as a result of my graduate studies are in large part due to his leadership.

Many other people have played a role in my success in graduate school which is particularly true for those who (in addition to Professor Migone) agreed to be in my dissertation committee: Professors Saikat Talapatra, Thushari Jayasekera, Dipanjan Mazumdar, and Maria Calbi (Denver University). Beyond that, many people in the Physics Department at SIUC (fellow students, faculty and staff) deserve some gratitude from me for all their various roles. I particularly appreciate the support from many in the department during a rough patch that I went through near the end of 2016.

My family has been patient, understanding, and supportive this whole time I've been in grad school and I must thank them for that. Unfortunately, my mother passed away in October of 2016. She was always there to encourage me to keep at it during times when my own motivation and enthusiasm began to wane. She won't be here to see me finish my degree, but I probably wouldn't be here if not for her support.

Thank you.

TABLE OF CONTENTS

ABSTRACT	I
ACKNOWLEDGEMENTS	III
TABLE OF CONTENTS	IV
LIST OF TABLES	VII
LIST OF FIGURES	VIII
CHAPTER 1 ADSORPTION	1
1.1 GENERAL CONTEXT	1
1.2 FUNDAMENTAL INTERACTIONS	3
1.3 MONOLAYER ADSORPTION ON PLANAR SUBSTRATES	7
1.4 MULTILAYER ADSORPTION ON PLANAR SUBSTRATES	9
1.5 ADSORPTION ON POROUS SUBSTRATES	12
CHAPTER 2 STATISTICAL MECHANICS AND THERMODYNAMICS OF ADSORPTION	15
2.1 THE CHEMICAL POTENTIAL AND THERMODYNAMIC EQUILIBRIUM	15
2.2 FREE ENERGY	17
2.3 ISOSTERIC HEAT OF ADSORPTION	18
2.4 ISOTHERMAL COMPRESSIBILITY	19
2.5 KINETICS OF ADSORPTION	20
CHAPTER 3 EXPERIMENTAL PROCEDURES	24
3.1 VOLUMETRIC ADSORPTION APPARATUS	24
3.2 PROCEDURE FOR MEASURING ADSORPTION ISOTHERMS	28
3.3 THERMO-MOLECULAR CORRECTION TO PRESSURE	33
3.4 TEMPERATURE CALIBRATION	35
3.5 EFFECTIVE SPECIFIC SURFACE AREA (ESSA) CALCULATION	37
3.6 ISOSTERIC HEAT CALCULATIONS	39
3.7 DERIVATIVE OF THE ISOTHERM CALCULATIONS	42
3.8 KINETICS OF ADSORPTION CALCULATIONS	43
3.9 ERROR ANALYSIS FOR PRESSURE MEASUREMENTS AND TEMPERATURE CALIBRATION	46

CHAPTER 4 SUBSTRATES	51
4.1 CARBON NANOTUBES	51
4.2 CARBON NANOHORNS	57
4.3 ZEOLITIC IMIDAZOLATE FRAMEWORK-8 (ZIF-8)	62
CHAPTER 5 CO ₂ ADSORPTION ON PURIFIED HIPCO SINGLE-WALL CARBON NANOTUBES	68
5.1 INTRODUCTION	68
5.2 EXPERIMENTAL DETAILS	69
5.3 ISOTHERMS	70
5.4 EFFECTIVE SPECIFIC SURFACE AREA	73
5.5 ISOSTERIC HEAT OF ADSORPTION	75
5.6 KINETICS OF ADSORPTION	78
CHAPTER 6 ETHANE ADSORPTION ON AS-PRODUCED DAHLIA-LIKE CARBON NANO HORN AGGREGATES	82
6.1 INTRODUCTION	82
6.2 EXPERIMENTAL DETAILS	82
6.3 ISOTHERMS	83
6.4 EFFECTIVE SPECIFIC SURFACE AREA	85
6.5 ISOSTERIC HEAT OF ADSORPTION	87
6.6 KINETICS OF ADSORPTION	90
CHAPTER 7 ARGON ADSORPTION ON CHEMICALLY OPENED DAHLIA-LIKE CARBON NANO HORN AGGREGATES	93
7.1 INTRODUCTION	93
7.2 EXPERIMENTAL DETAILS	93
7.3 ISOTHERMS	94
7.4 EFFECTIVE SPECIFIC SURFACE AREA	97
7.5 ISOSTERIC HEAT OF ADSORPTION	98
7.6 KINETICS OF ADSORPTION	100
CHAPTER 8 O ₂ ADSORPTION ON ZEOLITIC IMIDAZOLATE FRAMEWORK-8	106
8.1 INTRODUCTION	106
8.2 EXPERIMENTAL DETAILS	106
8.3 ISOTHERMS	107
8.4 EFFECTIVE SPECIFIC SURFACE AREA	109
8.5 ISOSTERIC HEAT OF ADSORPTION	110

8.6 KINETICS OF ADSORPTION	112
CHAPTER 9 CO ₂ ADSORPTION ON ZEOLITIC IMIDAZOLATE FRAMEWORK-8	115
9.1 INTRODUCTION	115
9.2 EXPERIMENTAL DETAILS	116
9.3 ISOTHERMS	116
9.4 EFFECTIVE SPECIFIC SURFACE AREA	117
9.5 ISOSTERIC HEAT OF ADSORPTION	118
9.6 KINETICS OF ADSORPTION	121
CHAPTER 10 SUMMARY AND CONCLUSIONS	123
10.1 ISOTHERMS	123
10.2 EFFECTIVE SPECIFIC SURFACE AREA	126
10.3 ISOSTERIC HEAT	126
10.4 KINETICS OF ADSORPTION	128
10.5 CONCLUDING REMARKS	130
REFERENCES	131
VITA	138

LIST OF TABLES

TABLE 3.1: COEFFICIENTS USED WITH EQUATION 3.9 FOR FIVE DIFFERENT GASES.	34
TABLE 3.2: LEAK RATE AND STANDARD ERROR ANALYSIS FROM EXPERIMENTAL PRESSURE DATA AT VARIOUS APPROXIMATE PRESSURES.	47
TABLE 10.1: LINEAR ISOTHERM TYPES BASED ON IUPAC DESIGNATIONS FOR ALL SYSTEMS AND C VALUES FOR SOME SYSTEMS USED IN THIS DISSERTATION. TEMPERATURE SCALED RELATIVE TO THE CRITICAL TEMPERATURE IS SHOWN IN PARENTHESES NEXT TO THE C VALUES.	124
TABLE 10.2: SUMMARY OF SURFACE AREA MEASUREMENTS. MONOLAYER DATA IS IN MMOLS/G AND ESSA DATA IS IN M ² /G. DATA USED IN THE CALCULATIONS WERE TAKEN FROM ISOTHERMS IN THE RANGE OF ROUGHLY 0.4 TO 0.54 T/T _c	126

LIST OF FIGURES

FIGURE 1.1: GENERAL FORM OF THE POTENTIAL ENERGY AS A FUNCTION OF DISTANCE DESCRIBED BY EQUATION 1.2. THE ADSORBATE WILL TEND TO SIT AT THE MINIMUM OF THE WELL.....6

FIGURE 1.2: THE GENERAL FORM OF THE THEORETICAL LANGMUIR ISOTHERM WHERE X_R IS THE RATIO OF THE NUMBER OF ADSORBED PARTICLES TO THE TOTAL NUMBER OF SITES AT ONE MONOLAYER.....8

FIGURE 1.3: DEPICTION OF LAYERS FORMING ON A PLANAR SURFACE ACCORDING TO THE BET THEORY. RED CIRCLES ARE ADATOMS AND THE BLACK LINE IS THE SURFACE OF THE ADSORBENT.....10

FIGURE 1.4: GENERAL FORM OF THE BET ISOTHERM WITH COVERAGE IN FRACTIONS OF MONOLAYER COVERAGE FOR C VALUES OF 1, 10, AND 100. COVERAGE SMOOTHLY DIVERGES AS IT APPROACHES A P/P_0 VALUE OF 1.10

FIGURE 1.5: THE SIX BASIC CLASSIFICATIONS OF SORPTION ISOTHERMS PROVIDED BY THE IUPAC (INTERNATIONAL UNION OF PURE AND APPLIED CHEMISTS). SOLID LINES ARE ADSORPTION CURVES AND DASHED LINES ARE DESORPTION CURVES.13

FIGURE 3.1: A SCHEMATIC OF THE GENERAL SETUP OF THE IN-HOUSE BUILT ADSORPTION SETUPS USED IN THIS DISSERTATION. BLACK LINES REPRESENT COPPER OR STEEL TUBING, WHILE BLUE LINES REPRESENT ELECTRICAL CONNECTIONS.....24

FIGURE 3.2: A SCHEMATIC OF THE CELL AND COLD HEAD SETUP. THE ADSORBENT IS LOADED INTO THE CELL WHICH IS WHERE ADSORPTION TAKES PLACE.....27

FIGURE 3.3: PRESSURE EVOLUTION IN THE DOSING VOLUME CORRESPONDING TO A POINT ON AN ISOTHERM FOR THREE GAUGES WITH DIFFERENT RANGES.....30

FIGURE 3.4: EXAMPLE ISOTHERMS FOR ARGON ADSORBED ON OPENED CARBON NANOHORNS AT 76.32 K.32

FIGURE 3.5: LIQUID/VAPOR SATURATION CURVES FOR A FEW ATOMIC AND MOLECULAR SPECIES.....37

FIGURE 3.6: DEMONSTRATION OF THE POINT-B METHOD USED FOR DETERMINING THE EFFECTIVE MONOLAYER CAPACITY.38

FIGURE 3.7: DEMONSTRATION OF THE METHOD USED TO FIND LNP VS. 1/T DATA FOR ISOSTERIC HEAT OF ADSORPTION CALCULATIONS. ISOTHERMS ARE FROM MEASUREMENTS OF ARGON ADSORBED ON OPEN CARBON NANOHORNS.....	40
FIGURE 3.8: DEMONSTRATION OF ISOSTERIC HEAT OF ADSORPTION CALCULATION	41
FIGURE 3.9: LINEAR FORCE MODEL PLOTS APPLIED TO EXPERIMENTAL PRESSURE DATA. THE FRACTIONAL COVERAGE (θ) IS THE AMOUNT ADSORBED AT TIME T DIVIDED BY THE AMOUNT ADSORBED AT EQUILIBRIUM.	44
FIGURE 3.10: ISOTHERMS CALCULATED USING EQUILIBRIUM PRESSURE AS P_F (FILLED SQUARES) AND PRESSURE AT A FRACTIONAL UPTAKE OF $\theta = 0.99$ AS P_F (OPEN SQUARES).	46
FIGURE 3.11: STANDARD ERROR IS CALCULATED FROM THE DATA OF THE LOWEST SCALE GAUGE FOR THE APPROXIMATE DOSING VOLUME PRESSURE BEING CONSIDERED.....	48
FIGURE 4.1: BOTH IMAGES ARE REPRODUCED FROM REFERENCE [48].....	52
FIGURE 4.2: GENERIC HOMOGENEOUS SWCNT BUNDLE	54
FIGURE 4.3: TEM MICROGRAPHS OF DAHLIA-LIKE NANOHORN AGGREGATES REPRODUCED FROM REF [61]	59
FIGURE 4.4: SCHEMATIC NANOHORN FIGURES.....	61
FIGURE 4.5: STRUCTURE OF ZIF-8 REPRODUCED FROM REFERENCE [13].....	64
FIGURE 4.6: STRUCTURE OF ZIF-8 REPRODUCED FROM REFERENCE [69].....	66
FIGURE 5.1: SEMI-LOGARITHMIC ISOTHERMS OF CO ₂ ADSORBED ON PURIFIED HIPCO SWCNT BUNDLES.	71
FIGURE 5.2: LINEAR ISOTHERMS OF CO ₂ ADSORBED ON PURIFIED HIPCO SWCNT BUNDLES. ISOTHERMS ARE OF TYPE II WITH A BROAD KNEE.	72
FIGURE 5.3: EFFECTIVE MONOLAYER CAPACITY USING DATA FROM THE ISOTHERM AT 158 K ($T/T_c = 0.52$).	74
FIGURE 5.4: ISOSTERIC HEAT (Q_{ST}) AS A FUNCTION OF COVERAGE. THE RED DASHED LINE INDICATES BULK LATENT HEAT.....	76
FIGURE 5.5: NATURAL LOGARITHM OF EQUILIBRIUM PRESSURE VS THE INVERSE OF TEMPERATURE. EACH LINE IS AT A CONSTANT COVERAGE, SHOWN ON THE RIGHT IN UNITS OF MMOLS/G.....	77
FIGURE 5.6: KINETICS OF ADSORPTION DATA FOR SELECT POINTS ALONG 146 K ISOTHERM. THE POINT NUMBERS ARE GIVEN IN THE LEGEND, WITH COVERAGE IN PARENTHESES IN UNITS OF MMOLS/G.....	79

FIGURE 5.7: SUMMARY OF ADSORPTION KINETICS DATA FOR FOUR ISOTHERMS. WAIT TIME VS. EQUILIBRIUM COVERAGE.	81
FIGURE 6.1: SEMI-LOGARITHMIC ISOTHERMS OF ETHANE ADSORBED ON AS-PRODUCED DAHLIA-LIKE CARBON NANO HORN AGGREGATES.....	84
FIGURE 6.2: LINEAR ISOTHERMS FOR ETHANE ADSORBED ON AS-PRODUCED DAHLIA-LIKE CARBON NANO HORN AGGREGATES.	85
FIGURE 6.3: DETERMINATION OF EFFECTIVE MONOLAYER CAPACITY USING DATA FROM THE ISOTHERM AT 164 K	86
FIGURE 6.4: ISOSTERIC HEAT (Q_{ST}) AS A FUNCTION OF COVERAGE. THE RED DASHED LINE INDICATES BULK HEAT OF CONDENSATION FOR ETHANE.....	88
FIGURE 6.5: NATURAL LOGARITHM OF EQUILIBRIUM PRESSURE VS THE INVERSE OF TEMPERATURE. EACH LINE IS AT A CONSTANT COVERAGE, SHOWN ON THE RIGHT IN THE LEGEND IN MMOLS/G.	89
FIGURE 6.6: KINETICS PLOTS FOR SELECT POINTS ALONG THE 164 K ISOTHERM. POINT NUMBERS ARE INDICATED IN THE RESPECTIVE LEGENDS WITH THE CORRESPONDING COVERAGE IN PARENTHESES IN MMOLS/G.....	90
FIGURE 6.7: KINETICS FOR POINTS ALONG SELECT ISOTHERMS AS FUNCTIONS OF EQUILIBRIUM COVERAGE.	91
FIGURE 7.1: SEMI-LOGARITHMIC ISOTHERMS OF AR ADSORBED ON OPENED DAHLIA-LIKE SWCNH AGGREGATES .	95
FIGURE 7.2: LINEAR ISOTHERMS OF AR ADSORBED ON OPENED DAHLIA-LIKE SWCNH AGGREGATES	96
FIGURE 7.3: THE THREE HIGHEST TEMPERATURE ISOTHERMS FROM FIGURE 7.1, IN MORE DETAIL.....	96
FIGURE 7.4: EFFECTIVE MONOLAYER CAPACITY USING DATA FROM THE ISOTHERM AT 82.07 K ($T/T_c = 0.54$).	97
FIGURE 7.5: ISOSTERIC HEAT AS A FUNCTION OF COVERAGE FOR AR-ONH	99
FIGURE 7.6: NATURAL LOGARITHM OF EQUILIBRIUM PRESSURE VS THE INVERSE OF TEMPERATURE. EACH LINE IS AT A CONSTANT COVERAGE, SHOWN ON THE RIGHT IN THE LEGEND IN MMOLS/G.	100
FIGURE 7.7: TIME TO REACH $\theta = 0.999$ FOR POINTS ALONG SELECT ISOTHERMS AS FUNCTIONS OF EQUILIBRIUM COVERAGE.	102
FIGURE 7.8: NEON DATA.....	103
FIGURE 8.1: SEMI-LOG PLOTS OF ISOTHERMS OF OXYGEN ADSORBED ON ZIF-8	108

FIGURE 8.2: LINEAR PLOTS OF ISOTHERMS OF OXYGEN ADSORBED ON ZIF-8. THE ISOTHERMS HERE ARE OF TYPE I, INDICATING MICROPOROSITY.	108
FIGURE 8.3: ISOTHERM DATA AT 62.96 K USED TO DETERMINE THE EFFECTIVE MONOLAYER CAPACITY FOR THE O ₂ – ZIF-8 SYSTEM (T/T _c = 0.41).	109
FIGURE 8.4: OXYGEN DATA.	110
FIGURE 8.5: LINEAR DRIVING FORCE PLOTS FOR SELECT POINTS ALONG THE 70.48 K ISOTHERM. THE POINT NUMBERS CORRESPONDING TO THE ISOTHERM IN FIGURE 8.1 (WITH COVERAGE IN PARENTHESES IN MMOLS/G) ARE GIVEN IN THE LEGEND. ONLY EVERY 20 TH POINT IS PRESENTED IN EACH PLOT FOR CLARITY.	113
FIGURE 8.6: KINETICS OF ADSORPTION FOR POINTS ALONG SELECT ISOTHERMS FOR O ₂ – ZIF-8. FOR THE SAKE OF CLARITY, ONLY THREE ISOTHERMS WERE CHOSEN TO BE DISPLAYED.	114
FIGURE 9.1: SEMI-LOG PLOTS OF ISOTHERMS OF CARBON DIOXIDE ADSORBED ON ZIF-8	117
FIGURE 9.2: ISOTHERM DATA AT 133.22 K (T/T _c = 0.44) USED TO DETERMINE THE EFFECTIVE MONOLAYER CAPACITY FOR THE CO ₂ – ZIF-8 SYSTEM.	118
FIGURE 9.4: KINETICS OF ADSORPTION DATA FOR SELECT POINTS ALONG THE 133.22 K ISOTHERM.	122
FIGURE 10.1: ISOSTERIC HEAT VS. FRACTION OF THE EFFECTIVE MONOLAYER CAPACITY FOR ALL OF THE STUDIES IN THIS DISSERTATION.	127

CHAPTER 1

ADSORPTION

Adsorption is the exothermic process in which atoms or molecules from a vapor state adhere to the surface of a solid. The process can be thought of as a 1st order phase transition involving a type of latent heat which in many ways is similar to the vapor to bulk liquid or solid transition. Generally speaking, at low surface coverage, the adsorbing particles will form a quasi-2D film on the surface of the solid. The mixture of vapor and film is known as the *adsorbate*. The solid (assumed to be stable) in an adsorbing system is known as the *adsorbent*, or *substrate*. Given the similarities of the words *adsorbate* and *adsorbent*, the term *substrate* will typically be favored over the term *adsorbent*, in this dissertation.

1.1 General Context

Adsorption has practical and fundamental applications spanning the disciplines of physics, chemistry, and engineering. A couple of specific applications which rely on adsorption processes to a large extent include those concerning the topics of gas storage and gas mixture separation.

Materials can be used as adsorbents for the purpose of capturing and storing gases. For instance, much research effort is being devoted to the adsorption of carbon dioxide [1] [2], methane [3], and molecular hydrogen [4]. Carbon dioxide is a greenhouse gas and contributes to global warming and the adsorption of CO₂ is part of a larger research effort more broadly known as “Carbon Capture and Storage.” More information on CO₂ adsorption/storage is discussed in section 5.1 of this dissertation as an introduction to the study of CO₂ adsorption on HiPCo carbon nanotubes. Methane is the prominent component of natural gas which is a fuel source that might replace conventional fossil fuels such as

gasoline in certain applications. Currently, storage of methane/natural gas is achieved by compressing it and putting it in high pressure tanks in vapor form. That method is costly and sorption on/in a porous framework in principle could allow for storage of methane/natural gas in a way that is lower in pressure and cheaper. A few materials that have been studied for the purpose of methane storage include activated carbon, carbon nanotubes, various metal-organic frameworks, and MCM-41 [3]. Like methane storage, hydrogen storage via adsorption is related to the energy problem because hydrogen is a potential alternative to fossil fuels. Storage of hydrogen in sufficient quantities is an important requirement in hydrogen energy applications. The qualities that make hydrogen compelling as an energy carrier include its abundance (the most abundant element in the universe), its high energy density per unit mass, and the fact that it burns clean and only produces water as a by-product [4]. Though there are many hurdles to its successful application, hydrogen's potential as an energy carrier continues to inspire much research interest. Materials that have been studied for the purpose of hydrogen sorption/storage include carbon nanotubes, fullerenes, graphene, mesoporous silica, MOFs, IRMOFs, COFs, and clathrates [4].

Adsorption can provide the basis for gas separation in air purification, and various processes in the petrochemical and chemical industries [5]. Pressure swing adsorption is a technique which might be used for separations as an alternative to cryogenic distillation in certain conditions [5]. An example of a system in which adsorption makes a viable alternative to distillation is the separation of ethane and ethene since those two chemical species are thermodynamically similar [6]. Materials that have been used for gas separation in industry and laboratory settings include activated carbons, carbon nanotubes, zeolites, and metal-organic frameworks (MOFs) [7]. MOFs are being studied as sorbents in the separation of xenon and krypton in radioactive nuclear waste [8].

A few other applications for adsorption processes include molecular filtration systems and nano-electronic devices [9], chemical sensing [10], molecular sieving [11], drug delivery [12] and catalysis [13].

Adsorption studies such as those presented in this dissertation can help shed light upon the suitability of materials for various applications. The focus in this dissertation is on thermodynamics and kinetics of adsorption, and these two topics are presented together for each adsorbate-substrate combination in the experimental data chapters. It will be seen that these two topics are very inter-dependent which compels studying them together. This helps fill an apparent void in the scientific literature since there appears to be few studies which consider both the adsorption thermodynamics and kinetics together.

1.2 Fundamental Interactions

A distinction must be made between *chemical* adsorption and *physical* adsorption. In physical adsorption, no chemical bonds are formed between the adsorbate and the substrate. As a result, the electronic states of the adsorbate and substrate remain largely unaffected [14]. In chemical adsorption this is not the case, as strong bonds can form between adsorbate and substrate. A somewhat arbitrary distinction is that the adsorption binding energy (the energy needed to remove an adsorbed particle from the substrate) for a physically adsorbed particle is less than about 0.5 eV, and for chemical adsorption is greater than about 0.5 eV [15].

Owing to the zero-point motion of electrons, a neutral atom will possess instantaneous multipole moments. Two neutral atoms that are well separated will interact via these instantaneous moments and the fields they produce. The most important of these interactions are the induced dipole-induced dipole moments which give rise to attractive forces known as London Dispersion Forces, which are a type of Van der Waals force. This attractive force will bring the two neutral particles together, until a short-range repulsion takes over. The short-range repulsion is a result of electronic wave overlap and the Pauli Exclusion Principle since electrons are fermions. Explaining this attraction and repulsion in

fundamental detail is a problem of quantum mechanics using first principles [14], and is beyond the scope of this dissertation.

Sufficient understanding of the interaction between adsorbate and substrate can be attained from considering semi-empirical methods such as that of atom-atom sums. The potential energy can be written as [14] [16]:

$$V(\{\vec{R}_\alpha\}) = \sum_{\alpha, j_\beta} \varphi_{\alpha, \beta}(\vec{R}_\alpha - \vec{R}_{j_\beta}), \quad 1.1$$

where the adsorbate, with atomic components α , is interacting with a substrate, with atomic components β , at site j_β . The form of $\varphi_{\alpha, \beta}$ is assumed, and the most widely used form is given by the Lennard-Jones potential [14] [16]:

$$\varphi(r) = 4\epsilon \left[\left(\frac{\sigma}{r} \right)^{12} - \left(\frac{\sigma}{r} \right)^6 \right], \quad 1.2$$

where the constants ϵ and σ are related to the binding energy, and size of the adsorbate, respectively. Values for ϵ and σ can be determined from measurements of viscosity, thermal conductivity, and deviations from the ideal gas law (2nd virial coefficients) [17]. If the values of ϵ and σ are needed for the case of the interaction between two different molecular/atomic species, the geometric mean of ϵ and arithmetic mean of σ can be used [17]:

$$\epsilon_{12} = \sqrt{\epsilon_1 \epsilon_2}, \quad \sigma_{12} = 1/2(\sigma_1 + \sigma_2). \quad 1.3$$

The subscripts 1 and 2 in equation 1.3 refer to the two different molecular/atomic species that are interacting.

Although an exponential dependence would be more accurate [14], the positive term raised to the 12th power in equation 1.2 represents the short-range overlap repulsion. The negative term raised to the 6th power represents the longer range attractive London Dispersion force due to induced dipole-induced dipole interactions. Induced dipole-induced quadrupole and induced quadrupole-induced quadrupole terms can also be included in the expression for $\phi(r)$, however those terms fall off much faster with increasing r and the induced dipole-induced dipole interaction dominates [17].

The form for the Lennard Jones Potential shown in equation 1.2 describes an interaction between individual atoms/molecules. If the surface of the substrate is approximated as a uniform continuum (and as a result, the sum in equation 1.1 changes to an integral), the interaction between a gas atom and the surface becomes [16]:

$$u(r) = 4\pi\epsilon n_s \left[\left(\frac{\sigma^{12}}{45r^9} \right) - \left(\frac{\sigma^6}{6r^3} \right) \right]. \quad 1.4$$

The atomic density of the solid surface is given by n_s , and r is the distance between surface and the particle in the gas phase.

A potential energy of the form given by equation 1.2 and 1.4 is shown in figure 1.1. The potential energy (red line) has a minimum at slightly greater than one atomic diameter (σ_0 in the figure). The value for $\sigma_0 = 2^{1/6}\sigma$ can be calculated mathematically by simply setting the derivative of $\phi(r)$ equal to 0 and solving for σ [17]. At r values greater than the minimum, the potential energy results in an attractive force which approaches zero asymptotically as r increases. At r values less than the minimum, the slope of the potential curve is negative which corresponds to a repulsive force due to electron overlap. The depth, and r -value, of the potential minimum (ϵ), and the value at which the plot crosses the r -axis (σ) in the repulsive regime, will vary depending upon where the adatom sits horizontally above

the surface of the substrate. This is due to the variation of the potential with respect to horizontal displacements along the surface even though equation 1.4 assumes a continuum. A consequence of the atomic structure of the solid adsorbent is a corrugation of the potential felt by the adsorbing particles [14] [16].

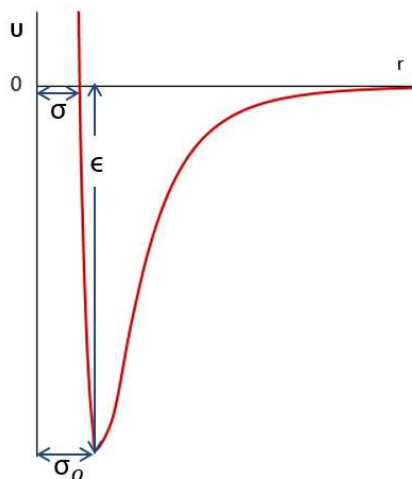


Figure 1.1: General form of the potential energy as a function of distance described by equation 1.2. The adsorbate will tend to sit at the minimum of the well.

Thus far, dispersion forces and close range repulsive forces have been described for neutral adsorbates and their interaction with neutral surfaces. In many systems, electrostatic fields from the substrate, and permanent adsorbate polarity, can have consequential effects [14]. Near an ionic surface, such as zeolites, there are strong electric fields and electric field gradients. Adsorbing molecules with permanent dipole, or quadrupole, moments can interact with these fields, or with other adsorbates. Even neutral atoms can become polarized in the vicinity of strong electric fields near an ionic surface. This can give rise to heats of adsorption on zeolites up to twice the heats of adsorption on the surface of neutral graphite [17].

1.3 Monolayer Adsorption on Planar Substrates

The Langmuir Isotherm is often used as a theoretical starting point for understanding monolayer film formation that follows from a gas being exposed to a clean planar substrate. It is a conceptually easy to understand model that can be derived using elementary methods of statistical mechanics and/or kinetic theory, following certain simplifying assumptions. Those assumptions are [18]:

1. There are N_s identical adsorption sites.
2. Each adsorption site contributes a binding energy of ϵ_0 (ϵ_0 is negative with respect to the potential energy of an adatom at an infinite separation).
3. Adsorbed particles do not interact laterally with each other.
4. There is only 1 adatom per adsorption site.

Following these somewhat artificial assumptions, a statistical mechanical [19], or kinetic [18], derivation leads to an equation relating the pressure of the vapor phase to the coverage of adsorbed atoms on the substrate. This equation can be written as:

$$P = \left[\frac{2\pi m}{h^2} \right]^{3/2} (kT)^{5/2} \left[\frac{x_r}{1 - x_r} \right] e^{(-\epsilon_0/kT)} \quad 1.5$$

where P is the pressure of the vapor phase, m is the mass of the adsorbing atom, h is Planck's constant, k is Boltzmann's constant, T is the isotherm temperature, and x_r is the ratio of the number of adsorbed particles to the total number of sites at one monolayer. The coverage dependent term (in brackets containing x_r) is the part that is actually known as the Langmuir Isotherm. A plot of x_r vs. P will show that P diverges as x_r approaches unity, as can be seen in the figure below.

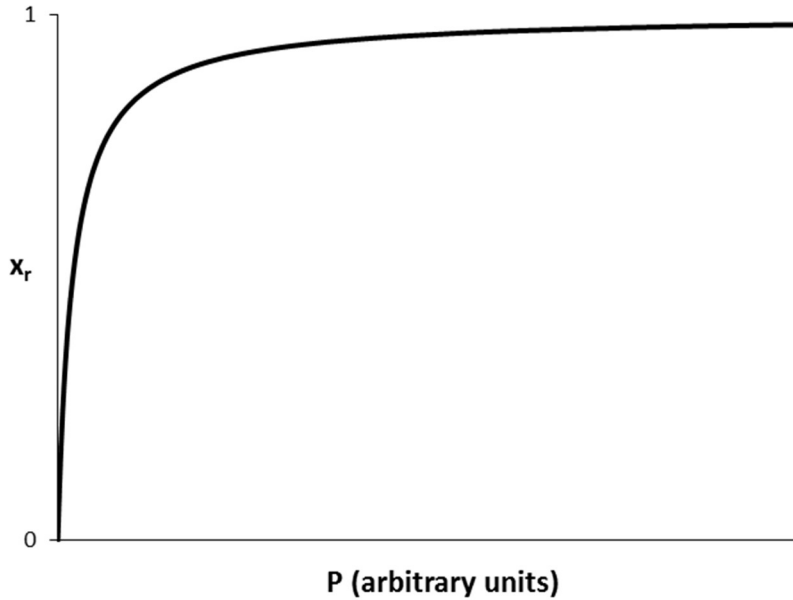


Figure 1.2: The general form of the theoretical Langmuir isotherm where x_r is the ratio of the number of adsorbed particles to the total number of sites at one monolayer.

Though the assumptions followed for the derivation of the Langmuir isotherm are somewhat artificial, insight can be gained by studying equation 1.5 and figure 1.2. For instance, the lowest coverages and pressures in figure 1.2 indicate an almost linear relationship known as Henry's law. Henry's law can be stated as the following equation [15],

$$P = k_H \left(\frac{N_f}{A} \right). \quad 1.6$$

where k_H is a constant which depends on the adsorption potential, and (N_f/A) is the 2D density of adsorbed particles on the surface. In this linear, low coverage regime, the most important interactions are between the surface and the adsorbate [19]. The pressure at higher coverages begins to diverge as a monolayer ($x_r=1$) is approached. This is due to most of the adsorption sites being occupied and the inability of more atoms to adsorb. However, the divergence of P towards infinity in figure 1.2 is purely an artifice of the model; in a real system, the highest value of pressure is limited by adsorbate bulk saturation. The general shape of the isotherm in figure 1.2 is called a Type I isotherm [20] and is

summarized with other isotherm types in figure 1.5. In real systems, a Type I isotherm is often indicative of chemical adsorption (which typically only occurs in one layer), or physical adsorption on microporous substrates. Physical adsorption on planar substrates often occurs in layers yielding a Type VI isotherm (figure 1.5) and so the Langmuir model is insufficient to describe such real systems.

1.4 Multilayer Adsorption on Planar Substrates

Following Langmuir, the B.E.T. method [21] extends the theory of adsorption to the multilayer regime. The assumptions made in the kinetic derivation of the B.E.T. equation [22] include the same assumptions for the derivation of the Langmuir isotherm, in addition to the following:

1. The heat of adsorption for every layer after the first is equal to the latent heat of condensation for the bulk 3D condensed phase of the adsorbate.
2. The rates of evaporation and condensation at every layer beyond the first are identical.

The picture of multilayer adsorption in the B.E.T. method is shown in figure 1.3.

Following the kinetic derivation which is based on the rates of evaporation and condensation at each of the layers, the following equation is arrived at [22]:

$$\frac{p}{x(p_o - p)} = \frac{1}{x_m c} + \frac{c - 1}{x_m} \left(\frac{p}{p_o} \right) \quad 1.7$$

In equation 1.7, p is the vapor pressure of the adsorbing species, p_o is the saturated vapor pressure of the adsorbing species, x is the amount adsorbed, x_m is the amount adsorbed at one monolayer, and c is a constant which is interpreted as the ratio of the lifetime of adatoms in the first layer to that of higher layers (lifetimes at higher layers are equal, according to assumption 2). Higher values of c can be interpreted as indicating stronger binding energies for the adsorbate on the substrate. Plotting x/x_m vs.

p/p_0 gives the shape of the B.E.T. isotherm. This can be seen more clearly, mathematically, by solving equation 1.7 for x/x_m and rearranging. The shape of the B.E.T. isotherm, which can be seen in figure 1.4, depends on the value taken for c .

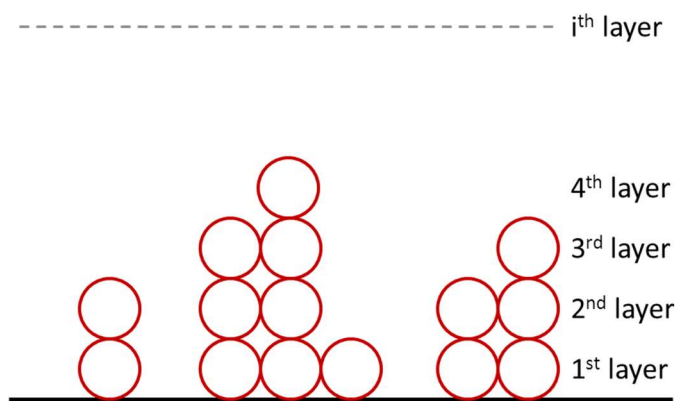


Figure 1.3: Depiction of layers forming on a planar surface according to the BET theory. Red circles are adatoms and the black line is the surface of the adsorbent.

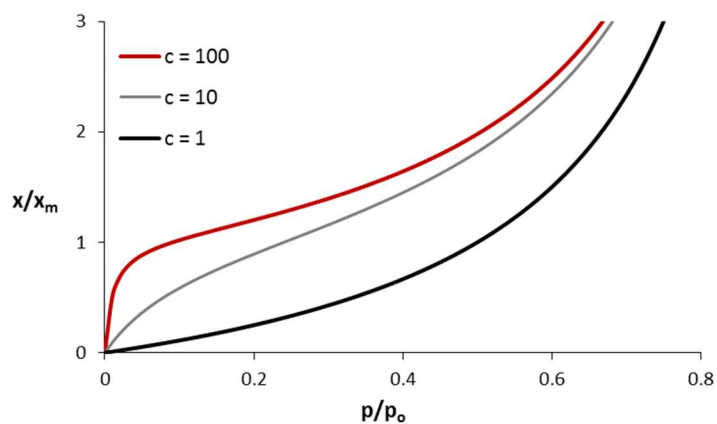


Figure 1.4: General form of the BET isotherm with coverage in fractions of monolayer coverage for c values of 1, 10, and 100. Coverage smoothly diverges as it approaches a p/p_0 value of 1.

For c values on the order of 100 or greater, the B.E.T. isotherm has a region at low pressure and coverage which corresponds to the Henry's law regime, similar to the Langmuir isotherm. After the "knee" in the region near one monolayer, the theoretical B.E.T. isotherm begins a long gradual ascent of increasing slope as the film grows in excess of the monolayer and saturated vapor pressure is approached. This is known as a Type II isotherm (see figure 1.5), and is indicative of a strong interaction between the adsorbate and a planar substrate in the Henry's law regime. For c values on the order of 10 or less, no steep region or sharp bend in the isotherm can be easily identified at low coverage which indicates weaker adsorbate-substrate interactions. Isotherms of this general shape are called Type III isotherms (see figure 1.5).

A weakness in the B.E.T. theory is highlighted by the experimental fact that, for many adsorbates, multilayer adsorption on a sufficiently energetically homogeneous surface results in an isotherm displaying clear steps corresponding to the formation of successive layers [23], a feature not present in figure 1.4 for any c value even though the surface is assumed to be perfectly homogeneous. The reason for the absence of steps in the BET isotherm is the assumption that all layers after the first have a heat of adsorption equal to the bulk heat of condensation. Clear examples of real stepwise isotherms are seen in the adsorption of krypton adsorbed on graphitized carbon black [23], and on exfoliated graphite [15].

However, the B.E.T. method is still useful as a means for gaining an elementary understanding multilayer adsorption, in the same way that the Langmuir method is useful for gaining an understanding of monolayer adsorption. In addition, the BET method can be used to estimate values of the effective specific surface areas for certain sorbate-substrate combinations.

1.5 Adsorption on Porous Substrates

So far, only planar substrates have been considered when describing adsorption processes and film formation. Many substrates possess varying degrees of porosity. Porosity is defined as the ratio of the empty volume *within* a solid (yet still accessible from the outside) to the total volume of the solid. Pores in substrates are generally divided up into three categories [24]: micropores are those with a width of 20 Å or less, macropores possess diameters with widths greater than 200 Å, and those with widths in between 20 and 200 Å are termed transitional pores, or sometimes mesopores. Diameter might be a misleading term considering that pores aren't always going to be cylindrical, or have circular openings, but the designations of pore width are still useful. In particular, the relations between the widths of pores, the diameters of adsorbates, and the mean free paths of adsorbates, will play a role in sorption and diffusion on and into the substrate.

Adsorption on solids with pore widths in the range of tens to hundreds of Å (roughly in the transitional and macropore range) will often show isotherms categorized as Type IV [25]. Type IV isotherms (shown in figure 1.5) are similar to Type II, with the addition of an extra near vertical riser at pressures and coverages intermediate between the first bend, and the approach to saturation.

If desorption is allowed to occur, the path followed as the vapor pressure is decreased will deviate from the adsorption path, resulting in a hysteresis loop (indicated by the dashed line in figure 1.5). The hysteresis is a result of capillary condensation, or, the formation of a bulk-like fluid phase which forms within the pores during the final stages of adsorption, before saturated vapor pressure is reached. By using a method based on the Kelvin Equation [25] and the data of an adsorption isotherm of Type IV, estimations of the pore size distribution for the substrate can be attained [25]. Additionally, the total pore volume can be calculated fairly straightforwardly by the assumptions that the density of the condensate is the same as the bulk liquid, and that the region in the isotherm immediately prior to saturated vapor pressure corresponds to pores that are completely filled up with liquid-like sorbate.

Another classification of isotherm than can result from sorption on a substrate with roughly transitional pores, or macropores, is that of Type V [25]. Type V isotherms (figure 1.5) have the same relationship to Type III isotherms that Type IV has to Type II, in that they are similar at the lowest and highest coverages and pressures but also include an extra near vertical riser in the intermediate region. Type V isotherms also include a hysteresis desorption loop as a result of capillary condensation although methods for estimating pore size distributions from such data are problematic due to large uncertainties.

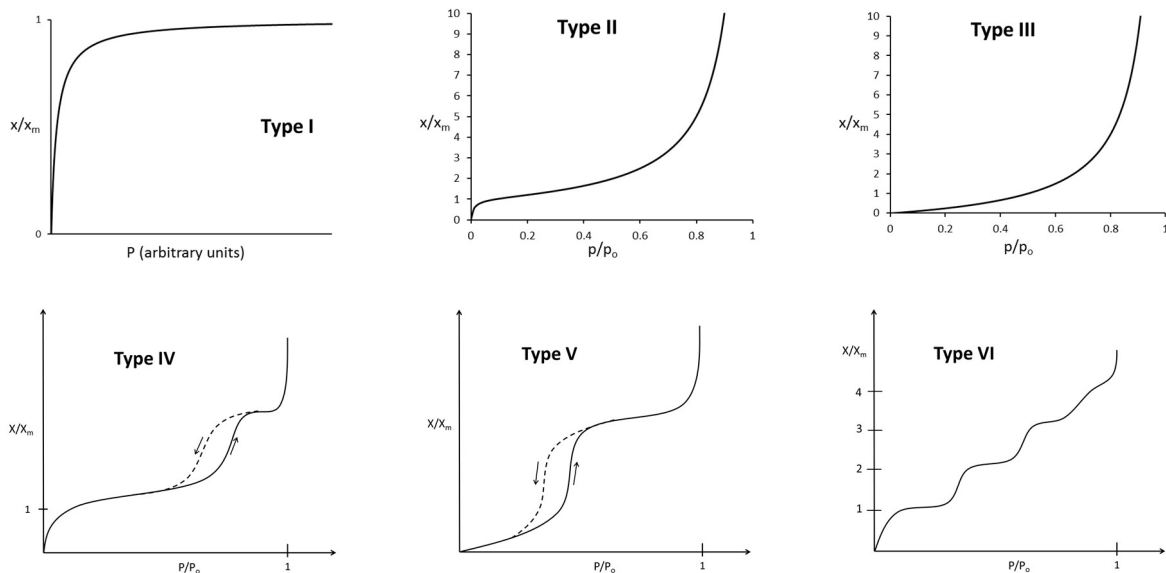


Figure 1.5: The six basic classifications of sorption isotherms provided by the IUPAC (International Union of Pure and Applied Chemists). Solid lines are adsorption curves and dashed lines are desorption curves.

- Type I – Langmuir isotherm (section 1.3).
- Type II – BET multilayer isotherm with strong interaction: $c = 100$ (section 1.4).
- Type III – BET multilayer isotherm with weak interaction: $c = 1$ (section 1.4).
- Type IV – Adsorption/desorption on porous substrate with capillary condensation. Strong sorbate-substrate interaction (section 1.5).
- Type V – Adsorption/desorption on porous substrate with capillary condensation. Weak sorbate-substrate interaction (section 1.5).
- Type VI – Stepwise isotherm resulting from formation of adsorbate layers on planar substrate (section 1.4).

Adsorption on microporous substrates often yields Type I isotherms [20]. The typical interpretation is that for an adsorbate on a microporous substrate, the plateau in the region of the isotherm after the bend corresponds to micropores filled with a fluid-like phase [20], which can allow for estimations of total pore volume in a manner similar to that for Type IV isotherms. Hysteresis has been identified in many Type I isotherms for microporous substrates [20] but is usually far less noticeable than the hysteresis in Type IV isotherms.

CHAPTER 2

STATISTICAL MECHANICS AND THERMODYNAMICS OF ADSORPTION

As stated in the Chapter 1 introduction, the adsorbate has two phases (film and vapor), while the substrate is the solid which acts as the adsorbent. In more general statistical and thermodynamic theories of adsorption, the three phases (film, vapor, and substrate) are not considered separately, but rather are considered all parts of one mixed, interacting, system [26]. However, the separation of film, vapor, and substrate into separate phases allows for useful approximations. For example, the 2D spreading pressure of the film (ϕ) and the 3D pressure of the vapor can each be considered separately even though the properties of the vapor phase will affect the properties of the film and vice versa [26].

The following sections offer a brief review of some of the relevant statistical mechanics and thermodynamics of adsorption that will help with interpretation of the experimental data presented later in the dissertation.

2.1 The Chemical Potential and Thermodynamic Equilibrium

There are two conditions for thermodynamic equilibrium between film and vapor: equality of the respective chemical potentials, and equality of temperature [27]. Experimentally, since temperature (T), volume (V), and the number of particles (N) are controlled, this condition of equilibrium is satisfied when the vapor pressure (P) has reached a constant value with respect to time. When this happens we can say that the chemical potential (μ) of the film and vapor are equal, or

$$\mu_{vapor} = \mu_{film}. \quad (2.1)$$

If the vapor pressure is not constant in time, there will necessarily be a net flow of particles between the film and vapor, and the chemical potentials will not be equal. Assuming the vapor to be ideal (which is an excellent approximation for vapors at low density and high temperature [28]), we can write [29],

$$\mu_{vapor} = \mu_{film} = -kT \ln \left[\frac{kT}{P \lambda_{th}^3} \right], \quad (2.2)$$

where k is Boltzmann's constant, and λ_{th} is the DeBroglie thermal wavelength. The right side of equation 2.2 is a commonly derived expression for the chemical potential of an ideal gas, and it shows that the equilibrium chemical potential of the film and vapor are proportional to the natural logarithm of the pressure. Experimentally, all measurements of the pressure come from the dosing volume which is held at room temperature. No measurements are taken directly from the adsorbed film. As a result, it is important to allow the system to reach thermodynamic equilibrium so we can relate our measurements of the gas in the dosing volume to the vapor and film in the cell which are in equilibrium.

An alternative way of stating the condition of thermodynamic equilibrium between film and vapor is obtained from the method of Gibbs [30], and is given by the equation [26],

$$ad\phi = vdP \quad (2.3)$$

where a and v are the specific area and specific volume of the film and vapor, respectively, and ϕ is the 2D spreading pressure of the film. Equation 2.3 is equivalent to equation 2.1, and will be used to derive an expression for the isothermal compressibility (see section 2.4) which will allow it to more easily be used in conjunction with experimental adsorption isotherm data

As stated in the discussion of the B.E.T. isotherm (section 1.4), adsorption on an energetically homogeneous surface will result in a stepped isotherm, where each step corresponds to an adsorbed layer. The near vertical risers in the steps of the figures cited in that discussion correspond to regions

where the vapor pressure (horizontal axis) is constant as coverage (vertical axis) increases. A glance at equation 2.2 shows that if the pressure is constant for regions of an isotherm, the chemical potential is also constant over that region. The binding energy within a layer is roughly constant, but decreases with each layer that is added because each progressive layer that forms is farther from the substrate. The pressure and chemical potential at which each layer forms (and hence, the location of the steps in the isotherm) is controlled, in part, by the binding energy [23]. A relatively high binding energy corresponds to a step at relatively low pressure and chemical potential, and vice versa.

Adsorption on a heterogeneous surface with a spread of binding energies will have a tendency to smear out the steps in the stepwise isotherms being discussed here. For isotherms of adsorption on porous substrates, this smearing is commonplace given that most porous substrates are effectively heterogeneous. The locations of steps (or substeps) in such isotherms correspond less to the formation of layers of adsorbate, and more to adsorption on groups of roughly similar binding energy sites on, and within, the substrate.

2.2 Free Energy

The Helmholtz free energy ($F = U - TS$) is a minimum at equilibrium [29]. For an adsorbate, the individual components (film and vapor) of the free energy can be summed [31]:

$$F = F_f + F_v \quad (2.4)$$

where the subscripts refer to film and vapor respectively. There is a very direct relationship between free energy and chemical potential [26]:

$$\mu_i = \left(\frac{\partial F_i}{\partial N_i} \right)_{T, V \text{ or } A} \quad (2.5)$$

where the subscript i refers to the phase (vapor or film), N refers to the number of particles in the phase. Large changes in the free energy of the film ($\Delta F = \Delta U - T\Delta S$) from point to point along an isotherm can result in additional smearing of substeps. This can happen for steps in an isotherm corresponding to adsorption on groups of sites with similar binding energy if the change in entropy ($T\Delta S$ term) is large. This can occur if linear adsorbates undergo rearrangement as isotherm coverage increases. The combination of energetically heterogeneous surfaces and large changes in the entropy per adsorbed particle can lead to isotherm substeps which are smeared out and barely discernible, if at all.

2.3 Isothermic Heat of Adsorption

Much like the condensation and deposition of bulk matter, adsorption is an exothermic process. The heat released during the condensation, or deposition, of a particle is the latent heat. Similarly, the heat released during the adsorption of a particle from the vapor phase to the film is the heat of adsorption. Various heats of adsorption exist [26] depending on the particular experimental conditions, and the one that is most relevant to the current dissertation is the isosteric (constant coverage) heat of adsorption given by [26],

$$q_{st} = kT^2 \left[\frac{\partial \ln P}{\partial T} \right]_{N_f, A} \quad (2.6)$$

where k is Boltzmann's constant, N_f is the amount of adsorbate in the film, A is the area of the film, and q_{st} is the isosteric heat of adsorption. Only a part of the heat released is reflected in the change in the energy per particle during the phase changes described, for latent heats [32], and for the heat of adsorption [26]. The isosteric heat is only equal to the binding energy at the limits of absolute zero temperature and zero surface coverage [26]. At finite values of T , and coverage, the isosteric heat will

also include terms which depend on the state of the film. The actual relationship between isosteric heat and binding energy can be stated as,

$$q_{st} = E_b + \gamma kT \quad (2.7)$$

where E_b is the binding energy, and γ is a constant which depends on the dimensionality of the film and vapor (see, for example, equations 5.1.6, and 5.2.11 in [19], and equation 4 in [33]).

The general form of the solution to equation 2.6 is the following,

$$\ln(P) = -\frac{q_{st}}{K_b T} + b \quad (2.8)$$

where it can be seen that if $\ln(P)$ is plotted vs. the inverse of temperature, the slope of the resulting line will be the negative of the isosteric heat of adsorption divided by Boltzmann's constant. The usefulness of equation 2.8 (as opposed to equation 2.6) is in the ease with which it can be applied to sets of experimentally obtained adsorption isotherms. Equation 2.8 becomes the Clausius-Clapeyron equation (equation 3.11) when it is applied to bulk phase changes, in which case q_{st} becomes the latent heat of the phase transition.

2.4 Isothermal Compressibility

In three dimensions, the isothermal compressibility is a measure of how the volume of a substance changes as pressure is varied, and can be written as the following [34],

$$K_T = -\frac{1}{v} \left(\frac{\partial v}{\partial P} \right)_T \quad (2.9)$$

where K_T is the isothermal compressibility, and little v is the volume per particle, or specific volume. The isothermal compressibility will diverge during phase transitions [34]. The two dimensional version of the

isothermal compressibility (K_{2D}) replaces v with a (specific area of adsorbed particles), and P with ϕ (2D spreading pressure of the film) [35], and is a measure of how the area of a film changes with respect to changes in spreading pressure:

$$K_{2D} = -\frac{1}{a} \left(\frac{\partial a}{\partial \phi} \right)_T \quad (2.10)$$

We can write the differential of specific area as,

$$da = -\frac{A}{N_f^2} dN_f \quad (2.11)$$

while equation 2.3 can be arranged as,

$$d\phi = \frac{N_f V}{A N_v} dP. \quad (2.12)$$

Substituting equations 2.3, 2.11, and 2.12 into equation 2.10 allows us to arrive at,

$$K_{2D} = \frac{1}{A} \frac{V}{N_v} \left(\frac{dN_f}{dP} \right)_T \quad (2.13)$$

which is a useful form of the isothermal compressibility. In particular, the term in parentheses can be calculated along an isotherm, point to point, to bring out certain features that might not be as apparent otherwise.

2.5 Kinetics of Adsorption

The kinetics of adsorption refers to how the rates of adsorption, and the times to reach equilibrium (relaxation times), are affected by the adsorption process. A gas that is exposed to a surface with available adsorption sites, will have a finite relaxation time. This relaxation time can be on the

order of seconds, minutes, hours, days, or even weeks depending on the complexity of the adsorption system, and the pressures and binding energies involved in the process.

For spherical, or effectively spherical, adsorbates with no permanent electric polarity on an energetically homogeneous surface where the surface is exposed directly to the gas, the equilibrium adsorption kinetics trends have been described theoretically by the following equation [36] [37]:

$$\tau_{eq} = k_{des} e^{\beta E} (1 - n_{eq}) \quad (2.14)$$

where τ_{eq} is the equilibrium time, k_{des} is a characteristic time for the process of desorption, $\beta = 1/k_B T$, E is the binding energy, and n_{eq} is the equilibrium fractional coverage. From equation 2.14 it is seen that the time to reach equilibrium: decreases as fractional coverage increases, increases as binding energy increases, and decreases as temperature increases. These trends can all be related to the pressure [36], which, as discussed previously, is proportional to the exponential of the chemical potential. As fractional coverage increases, so too does the vapor pressure which means that there are more adsorbate particles in the gas phase available to adsorb and the process is faster. The explanation for binding energy dependence is similar; as the binding energy of the adsorbate on the substrate increases, the pressure needed for adsorption to occur at a specific coverage decreases. This leads to fewer adsorbate particles in the gas phase being available for adsorption at that coverage and therefore slower kinetics. Likewise, increasing temperature leads to increasing pressure which, again, leads to more adsorbate particles being available for adsorption and therefore faster kinetics.

The trends in the adsorption kinetics are more complicated when considering adsorption of linear molecules, or sorbates with permanent electric moments on heterogeneous surfaces, or on substrates possessing porosity. All of the systems studied in this dissertation are more complicated than the simple case of spherical (or effectively spherical), non-polar sorbates on planar substrates and most of the kinetic results presented in later chapters will reflect that.

Diffusion of the adsorbate on the surfaces, and within the pores, of a porous substrate can play a role in the kinetics of adsorption. A convenient mathematical representation of diffusion is given by Fick's first equation [38],

$$J = -D(c) \frac{\partial c}{\partial r} \quad (2.15)$$

where J is the flux, $D(c)$ is the diffusion constant, c is the concentration of the diffusing particles, and r is position. The interpretation of equation 2.15 is that particles will tend to diffuse in the direction of the largest gradient of concentration. The flux, J , is also proportional to the gradient of chemical potential [38] [39], which is a more statistical way of thinking about Fick's law.

The presence of an adsorbate on macropores will involve diffusional processes. At least four different mechanisms are identified and they are [38]: molecular, Knudsen, Poiseuille, and surface diffusion. Another form of Fick's first law is defined for the case of macropore diffusion [38],

$$J = -\epsilon_p D_p \frac{\partial c}{\partial r} \quad (2.16)$$

where ϵ_p is the porosity as defined in section 1.5, and D_p is the pore diffusivity which is defined as the ratio of the diffusivity (D) to the tortuosity factor (τ). The tortuosity is a geometric factor that is generally proportional to the inverse of the porosity. Having D_p defined in such a way is necessitated by the fact that most pores aren't straight perfect cylinders, but rather involve some randomness in their geometry. Essentially, the more meandering the path of a pore is, the higher the tortuosity factor will be, and the pore diffusivity will be lowered.

For adsorbates in micropores, diffusion is a slow, activated process [38]. The activation energy depends on the size of the adsorbate in cases where the microporous window opening is similar in size

to the adsorbate. The temperature dependence of the diffusion constant in microporous diffusion can generally be described by a typical equation for activated processes [38]:

$$D = D_* e^{-E/RT} \quad (2.17)$$

where D_* is the pre-exponential factor, E is the activation energy, and R is the universal gas constant.

Several models exist for analyzing the kinetics of adsorption. A model based on Fickian diffusion [40] provides a means for relating fractional uptakes to quantities depending in part on diffusion constants. Alternatives to the Fickian Diffusion (FD) model are the Linear Driving Force (LDF) model and the Quadratic Driving Force (QDF) model [39]. The LDF model in particular has been shown to be essentially equivalent to the relatively more rigorous but mathematically cumbersome FD model for adsorption on heterogeneous surfaces [39]. The LDF model may be summarized by the following equation [41],

$$\theta = 1 - e^{-kt} \quad (2.18)$$

where θ is the fractional uptake (mass adsorbed at time t divided by mass adsorbed at equilibrium), k is a constant which is proportional to the diffusion constant, and t is time. By rearranging equation 2.18, it can be seen that a graph of $\ln(1-\theta)$ vs. t will yield a plot with slope k . Given that a heterogeneous substrate will not always have a single diffusion constant [39], an LDF plot for adsorption on such a substrate will often involve more than one rate constant, and will not be linear over the entire coverage range.

CHAPTER 3

EXPERIMENTAL PROCEDURES

3.1 Volumetric Adsorption Apparatus

Adsorption isotherms were measured using in-house built setups, an example of which is shown schematically in figure 3.1.

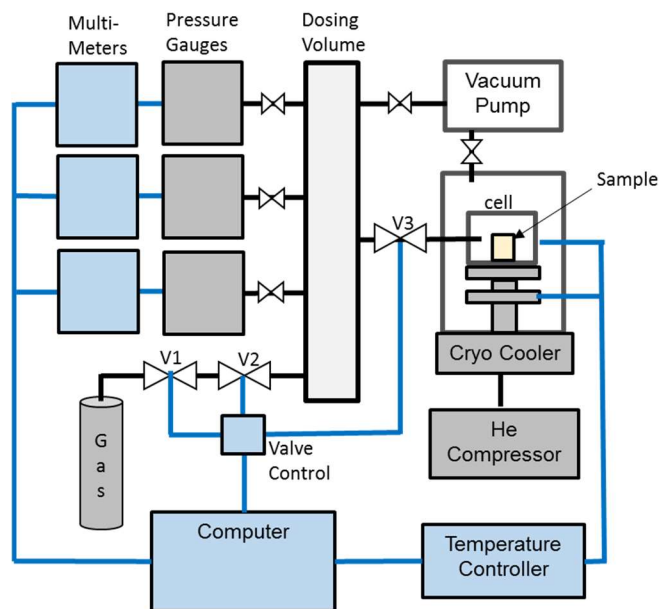


Figure 3.1: A schematic of the general setup of the in-house built adsorption setups used in this dissertation. Black lines represent copper or steel tubing, while blue lines represent electrical connections.

High vacuum levels (on the order of 10^{-7} Torr), in the experimental volumes of the setups described here, are achieved using combinations of multiple vacuum pumps in series. One such pumping station consists of a mechanical pump and an oil diffusion pump. The mechanical pump is used as a

roughing pump to achieve low vacuum (on the order of 10^{-3} Torr) in the experimental volumes and in the diffusion pump. The diffusion pump cannot operate without the aid of the roughing pump. Once a low vacuum is reached, the oil diffusion pump may be used to achieve high vacuum. Another pumping station variation is one that includes a diaphragm mechanical pump and turbo-molecular pump in series. The diaphragm pump is used for the purpose of roughing the volumes down to low vacuum and the turbo-molecular pump is used to achieve high vacuum. Similar to the diffusion pump, the turbo-molecular pump cannot operate on its own and must be used in conjunction with a roughing pump.

The dosing volume (V_d) is part of the experimental volume which is made up of copper tubing sections and consists of a volume of anywhere between approximately 80 and 250 cc depending on the particular setup. It is connected to one of the previously described pumping stations and is typically pumped to high vacuum levels for a period of at least 24 hours prior to the start of an isotherm measurement. This is necessary to ensure that as much atmospheric gas as possible, given practical limitations, is evacuated from the experimental volumes. In a sense, the dosing volume is the central “hub” of the experimental apparatus. It is connected not only to the pumping station, but also to the pressure gauges, sample-containing cell, gas tank (via a two-stage regulator), and to any additional ports that are included for the purpose of leak detection.

Connected to the dosing volume are three MKS Baratron capacitance pressure gauges. All three gauges have outputs in the voltage range 0 to 10 V, and the range of pressures are, respectively, 0 to 1 Torr, 0 to 10 Torr, and 0 to 1000 Torr. Having three gauges at different sensitivities allows for precise measurements throughout the whole range of pressures from about 1000 Torr down to the 10^{-3} Torr range. Connected to each pressure gauge is a Keithley 2000 Multi-Meter which can be used to monitor the voltage, and hence the pressure, and communicate with the computer via a National Instruments data acquisition board.

The gas tank is connected to the dosing volume via a two-stage regulator and two electro-pneumatic valves, labeled V1 and V2 in figure 3.1. A third electro-pneumatic valve, labeled V3, connects the dosing volume to the cell which contains the sample. These electro-pneumatic valves are controlled either manually or automatically through a switch-board connected to the computer. The cell sits atop a cold head refrigerator and is housed inside a vacuum sealed can. Similar to the dosing volume, the cell and can are pumped to high vacuum levels for a period of at least 24 hours prior to starting the experiment. The cell is evacuated for the same reason that the dosing volume is pumped, so that the experiment can be run with as little interference from the other chemical species present in air as possible. The can is pumped out for a different reason. Since the adsorption experiments are carried out at low temperature, the temperature of the cell needs to be kept as constant as is practically possible. Achieving a low temperature would be near impossible if the cell were sitting at room pressure. Pumping out the can ensures that there is as little thermal connection as possible with atmospheric gas by way of convection and conduction of heat, allowing the refrigerator to cool the cell.

A schematic of the sample-containing cell, located within the vacuum pumped can, is shown in figure 3.2. Low temperatures are achieved for the cell using a combination of a helium compressor and Model 22 Refrigerator, both made by CTI Cryogenics. The cooling system by itself will cool the cell down to approximately 20K. Heat must be supplied to bring the temperature of the cell back up to a level needed for the isotherm being measured. This is achieved using two temperature controllers each of which is a Lakeshore Model 331, 332, or 340.

Temperature is monitored and controlled in two stages within the can. The bottom stage is connected directly to the cold head of the cryo-cooler and the temperature here is monitored using a diode sensor. The cold head heater consists of a cylindrical piece of copper around which is wound a wire with a resistance of approximately 50 ohms per foot. This high resistance wire is soldered to copper wire which is connected to the cold head temperature controller. The top stage is the cell itself, which

contains the sample. The temperature of the cell is monitored by another temperature controller using a platinum resistance sensor. For heating, a high resistance wire is wound around the cell itself and is connected to the cell temperature controller. The cold head and cell are connected via thin strips of copper. The amount of current supplied to the heater wires by each respective temperature controller is determined using an algorithm with three variables. The value of these variables are user controlled. The combination of two stages connected by low thermal conductivity metal, and user controlled variables for the output to the heaters, allows for very stable temperature control which is constant to a hundredth of a Kelvin.

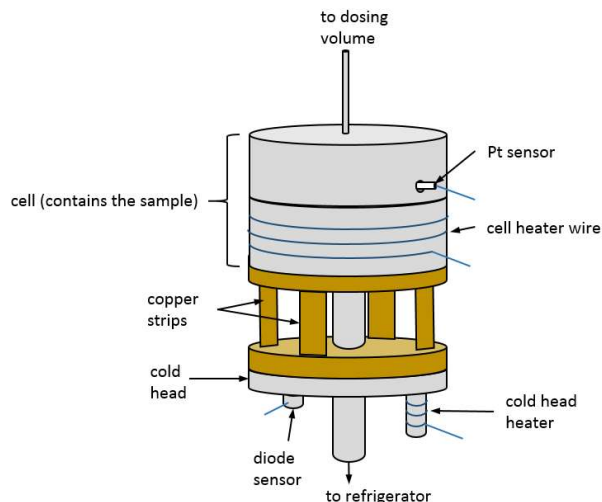


Figure 3.2: A schematic of the cell and cold head setup. The adsorbent is loaded into the cell which is where adsorption takes place.

To ensure that the experimental volumes are as leak tight as possible, extra ports are typically included, which are attached to the dosing volume. These ports allow for the use of a helium leak detector. The leak detector itself is used to vacuum pump the experimental volumes. Once a sufficient vacuum level is reached, low purity helium is sprayed around the experimental volumes while the leak detector is still attached and pumping on the volumes. If a leak is present in the experimental volume, sprayed helium will make its way through the leak and into the leak detector. There is very little He in

the atmosphere under normal conditions, so if the leak detector detects high amounts of helium, it must necessarily have come from that which was sprayed. If a leak is identified and located, steps must be taken to ensure the system is leak tight again. Sometimes fixing a leak is as simple as tightening a nut but sometimes parts of the system (such as valve mechanisms) must be replaced entirely.

3.2 Procedure for Measuring Adsorption Isotherms

A brief discussion of units must occur prior to the description of the procedure. The unit of pressure given by the pressure gauges described in the previous section is Torr, with 1 Torr equal to approximately 0.0013 atm, or 133.322 Pa. Since volumes are measured in units of cubic centimeters, and temperature in Kelvin, it becomes convenient to use the unit of cc-Torr at 273 K (“cc-Torr” for short) to indicate the amount of a substance:

$$1 \text{ cc} - \text{Torr} = 3.54 \times 10^{16} \text{ molecules.} \quad 3.1$$

1 cc-Torr is the amount of a substance in the gas phase required to fill a volume of 1 cc to a pressure of 1 Torr at a temperature of 273 K. This can be shown explicitly using the ideal gas law,

$$N = \frac{PV}{k_B T} = \frac{(133.322 \text{ Pa})(10^{-6} \text{ m}^3)}{(1.381 \times 10^{-2} \frac{\text{m}^2 \text{kg}}{\text{s}^2 \text{K}})(273 \text{ K})} = 3.54 \times 10^{16}. \quad 3.2$$

Using units of cc-Torr is purely a matter of convenience which slightly simplifies the calculations in the following section. Converting to other units for number or amount is a simple matter if and when it is necessary.

Using the setup shown schematically in figure 3.1 and described in section 3.1, adsorption isotherm measurements are conducted. After pumping out the can, cell, and dosing volume for at least 24 hours using the high vacuum pumps previously described, the valve to the cell (V3) is closed and the cooling station is turned on and allowed to achieve the required cell temperature (T_c). This can take anywhere from a few hours to a day depending on how low the temperature needs to be. A manual valve between the pumping station and dosing volume is closed prior to starting the experiment. The can, however, is pumped out continuously to help ensure a constant T_c during the entire duration of the experiment.

With V3 closed, gas is dosed into the dosing volume using V1 and V2, in the following manner. First, V1 is opened for a short period to let gas into the small volume (less than 1 cc) between V1 and V2. Then V1 is closed. After V1 is closed, V2 is opened to let the small shot of gas into the dosing volume (V_d). Then V2 is closed and the cycle repeats as many times as necessary in order to reach the required pressure. This pressure is recorded by the computer with a program written in LabView as the initial pressure, or P_i . This method of dosing gas in small shots is used because it allows for very fine control of the amount of gas that is let into the system. Sometimes this very fine control is needed to obtain isotherms with sufficient detail, especially at low pressures. The valves can be controlled either manually or automatically with a program written in LabView. Another LabView program is used to continuously record the pressure in the dosing volume and the cell temperature in user specified intervals (1 minute is a typical interval). Once P_i is recorded, V3 is opened which allows the gas to diffuse to the cell through a 1/16th in. outside diameter stainless steel tube where it is free to adsorb onto the sample. The pressure in the dosing volume is monitored continuously as the gas adsorbs onto the sample. Eventually, the vapor phase and adsorbed film reach a state of thermodynamic equilibrium and the pressure becomes constant, within a certain reasonable variation due to noise. This final equilibrium pressure is recorded as P_f .

An example of a pressure plot recorded by all three gauges including initial and final values of pressure is shown in figure 3.3. The plot on the left shows the overall evolution of the pressure after the opening of V3 at $t=0$. The initial value of pressure in this case must come from the gauge with the highest range (1000 Torr gauge) because the value of $P_i=65$ Torr is beyond the range of the other two, which are both maxed out at roughly 1.4 and 14 Torr, respectively. The plot on the right is the same set of data with the pressure axis expanded greatly. This is to show in more detail the attainment of thermodynamic equilibrium and how at such low pressures, the lower range gauges are more appropriate for choosing a value of P_f which in this example is somewhat less than 0.01 Torr. The 1000 Torr gauge shows considerably more noise and systematic error at this low pressure range. Additionally, it can be seen that the value of equilibrium pressure isn't reached until somewhere in the vicinity of 5 or 6 hours.

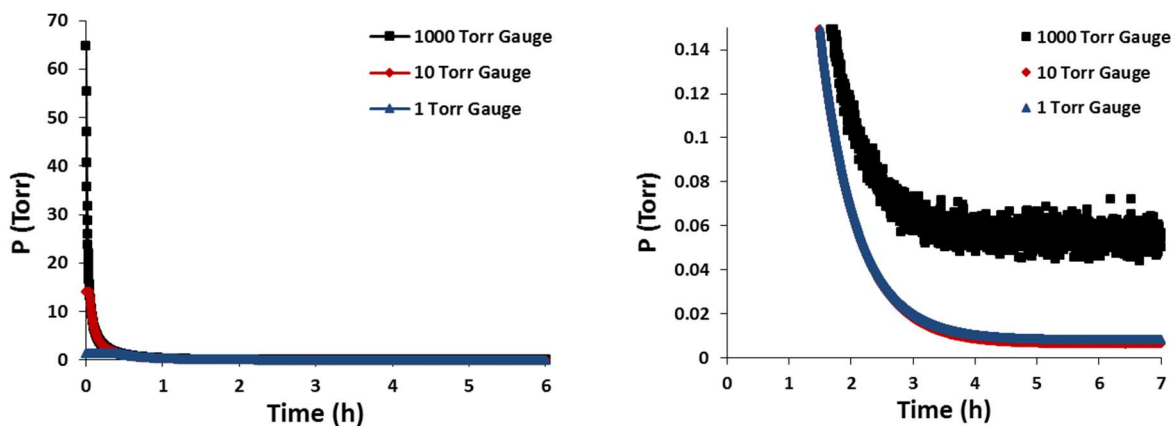


Figure 3.3: Pressure evolution in the dosing volume corresponding to a point on an isotherm for three gauges with different ranges.

After the first dose of gas reaches equilibrium, the amount adsorbed (in units of cc-Torr) for this first point can be calculated. The amount of gas that effectively leaves the dosing volume and makes its way into the cell after V3 is opened is denoted A_{in} and is calculated by using the following equation,

$$A_{in} = (P_i - P_f)V_d * \frac{273K}{T_r}, \quad 3.3$$

where V_d is the dosing volume, and T_r is room temperature (T_r is assumed to be constant at a typical value of 295 K). The amount of gas that effectively makes its way into the cell, but does NOT adsorb onto the sample, is termed the vapor phase. The amount in the vapor phase is denoted A_{vap} , and is calculated by using the equation,

$$A_{vap} = P_f * V_c * \frac{273K}{T_c}, \quad 3.4$$

where V_c is the volume of the cell not occupied by the sample (typically between 5 and 10 cc), and T_c is the temperature of the cell. The amount adsorbed at this first point is simply the difference between the above two equations, or,

$$A_{ads,1} = A_{in,1} - A_{vap,1} \quad 3.5$$

where A_{ads} denotes the amount adsorbed onto the sample, and the subscript 1 refers to the first point.

After the amount adsorbed is recorded for point 1, the process is repeated, i.e., V3 is closed and the dosing in of gas through V1 and V2 proceeds as before. A new P_i , and P_f will be attained for point 2.

To calculate the amount adsorbed at point 2 and beyond, the following equation is used,

$$A_{ads,n} = A_{sum} - A_{vap,n}. \quad 3.6$$

where A_{sum} is the total amount of gas that has effectively left the dosing volume and made its way to the cell for every point in the isotherm up to, and including, the current point. A_{sum} can be expressed simply as,

$$A_{sum} = \sum A_{in} \quad 3.7$$

For each point, a P_f and A_{ads} pair will be respectively measured and calculated. An adsorption isotherm is a plot of A_{ads} vs. P_f (or $\ln(P_f)$). An example of each one of these types of isotherms is shown in figure 3.4, for the case of argon adsorption on chemically opened carbon nanohorns at 76.32 K. The amounts adsorbed indicated by the vertical axes for these isotherms have been converted from cc-Torr to millimols (mmols). These isotherms are part of a larger data set and will be discussed more in later sections.

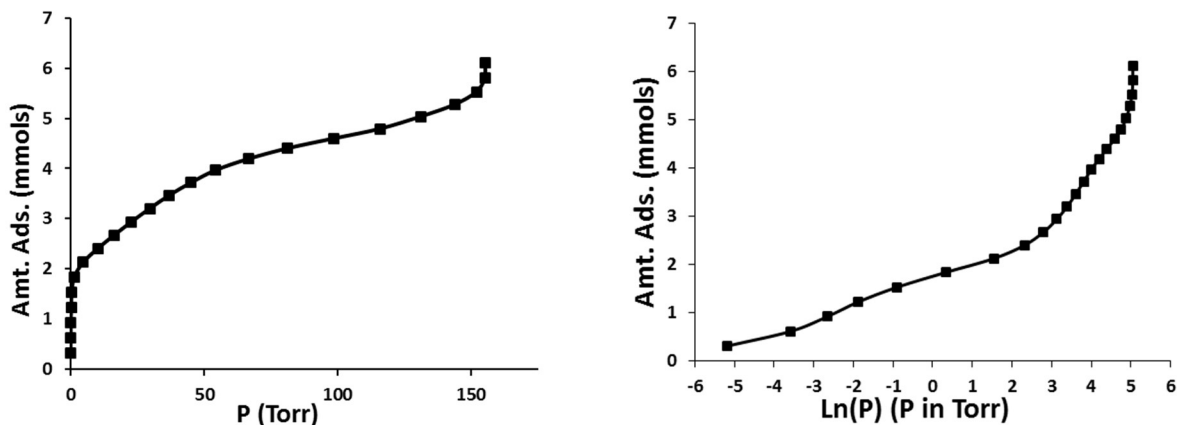


Figure 3.4: Example isotherms for argon adsorbed on opened carbon nanohorns at 76.32 K.

3.3 Thermo-molecular Correction to Pressure

Corrections to the final pressures (P_f) measured in the dosing volume during the measurement of an adsorption isotherm are necessary. This is due to an effect called thermal transpiration, or the gradual movement of particles in an unevenly heated container from the colder side to the warmer side [42]. If there are two containers at different temperatures with the same gas, and if those two containers are connected by a small opening with a diameter several times smaller than the mean free path of the particles in the gas, thermal transpiration will occur. This diffusion happens even if the initial pressure of the gas in both containers is the same, and will continue until the following condition is met [42]:

$$\frac{P_1}{P_2} = \left[\frac{T_1}{T_2} \right]^{1/2}, \quad 3.8$$

where P , and T , are pressure and temperature respectively, and the subscripts refer to the two different containers.

A similar situation arises if the two containers are connected by a long tube with a diameter on the order of several times smaller than the mean free path of the gas. This is due to thermal transpiration and to a process called thermal creep [43]. In the experimental setups used to measure adsorption isotherms, the dosing volume (where pressure measurements are made) is connected via a small 1/16th inch outer diameter tube (inner diameter is 1/16th – 0.02 inches) to the cell which is held at lower temperature. This constitutes a situation in which thermal transpiration needs to be taken into account for the attainment of accurate measurements of the pressure inside the cell.

As stated, the effect of thermal transpiration occurs in the case where the connecting diameter hole is smaller than the mean free path of the particles in the gas. The mean free path is inversely

proportional to the density of the gas and so this effect is more noticeable as pressure is lowered. The correction is given as the following empirical relation [44],

$$P_{corr} = P_{exp} * \left[\frac{\sqrt{T_c/T_r} - 1}{AX^2 + BX + C\sqrt{X} + 1} + 1 \right], \quad 3.9$$

where P_{corr} is the corrected pressure, and P_{exp} is the experimentally measured pressure. The coefficients A, B, and C are empirically determined for each gas, and the values for select gases are shown in table 3.1. X is given by the following relation [44]:

$$X = \frac{2P_{exp}d}{T_{cell} + 295K}, \quad 3.10$$

where d is the diameter of the connecting tube (1.1 mm in the present case).

Table 3.1: Coefficients used with equation 3.9 for five different gases.

Gas	A (K/mmTorr) ²	B (K/mmTorr)	C (K/mmTorr) ^(1/2)
Ar	10.8 x 10 ⁵	8.08 x 10 ²	15.6
O ₂	8 x 10 ⁵	17.5 x 10 ²	-
Ethane	30 x 10 ⁵	1.5 x 10 ²	90
Propane	40 x 10 ⁵	6 x 10 ²	120
CO ₂	17 x 10 ⁵	8 x 10 ²	64

3.4 Temperature Calibration

Although the temperature of the cell can be controlled precisely to one hundredth of a Kelvin, the actual temperature in the cell might differ from that which is read by the temperature controllers. As a result of this, the actual temperature must be calibrated through other means. The method of doing this is based on the fact that a gas will condense to solid, or liquid, at a known pressure based on the temperature of the gas [32]. The pressure at which the phase change occurs is known as the saturated vapor pressure. It occurs at a point on the P-T phase diagram which means that the pressure and temperature are both constant during the phase transition. If the saturated vapor pressure can be measured in an isothermal process, the temperature can be determined unambiguously by comparison to known saturation data, or by using an equation which relates temperature to the saturated vapor pressure.

The slope of the saturation curves for both liquid condensation and solid deposition is determined by the Clausius-Clapeyron equation [34]:

$$\frac{dP_{\sigma}}{dT} = \frac{L}{T\Delta v}, \quad 3.11$$

where P_{σ} is the coexistence pressure, L is the latent heat per particle, T is the temperature, and Δv is the difference in volume per particle (specific volume) between the vapor phase and condensed phase. The Clausius-Clapeyron equation applies generally to all 1st order phase transitions with a latent heat [34]. Various semi-empirical equations have been developed in order to best relate coexistence vapor pressure and temperature experimentally and many of them are based on the Clausius-Clapeyron equation [45]. The most widely used vapor-pressure/temperature relationship is the Antoine Equation [45],

$$\log(P) = A - \frac{B}{T + C} \quad 3.12$$

where P is the vapor pressure at equilibrium with the condensed phase, T is the temperature, and the A , B , and C coefficients are constants which are specific to the chemical species and temperature range. If the saturated vapor pressure of an isotherm is measured and substituted for P in the Antoine equation, then the temperature can be determined, provided good values of the coefficients are known for that specific gas and temperature range. Antoine equation coefficients are typically obtained from the Chemistry WebBook at the NIST (National Institute of Standards and Technology) website [46]. Additionally in the Chemistry WebBook at the NIST website are tabulated vapor-pressure/temperature coexistence curves which can be used to calibrate the isotherm temperatures in the case that inadequate Antoine coefficients are provided. A few liquid/vapor coexistence curves taken from data in the Chemistry WebBook website are shown in figure 3.5 below for the case of some common gases used in adsorption studies. Relatively small, weakly binding atoms/molecules tend to be on the left of this type of plot at colder temperatures, while relatively large, strongly binding atoms/molecules tend to be on the right at higher temperatures.

The saturated vapor pressure is identified in adsorption isotherms at the highest coverage where the isotherm shows a vertical riser, or step. This is demonstrated in figure 3.4 at, and above, coverages of about 5.5 mmols. In those isotherms, the pressure at this vertical step is identified as the saturated vapor pressure for Ar at the isotherm temperature (which would be determined by one of the above methods).

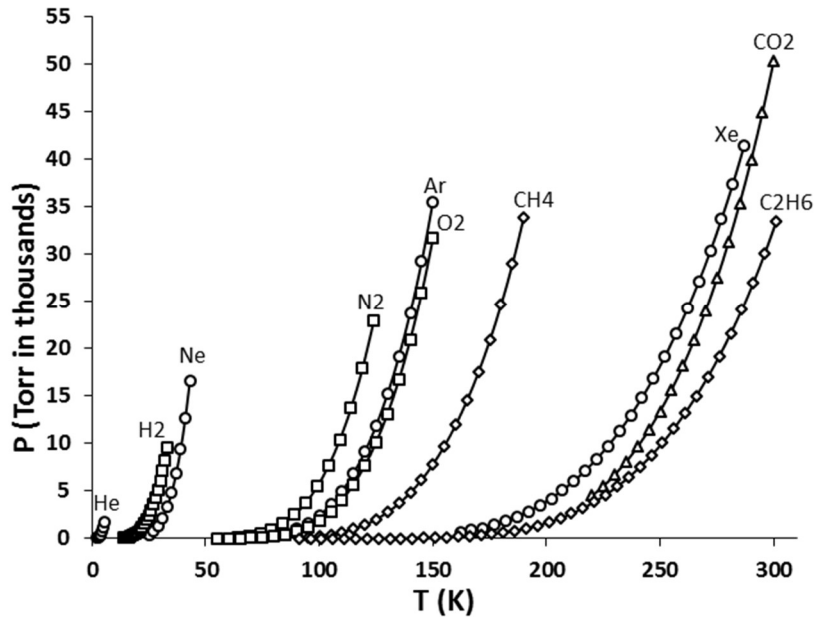


Figure 3.5: Liquid/Vapor saturation curves for a few atomic and molecular species.

3.5 Effective Specific Surface Area (ESSA) Calculation

Adsorption isotherms can be used to find the amount of adsorbate on a perfectly planar substrate which makes up the first layer. If the amount of adsorbate in one monolayer is known, and if the amount of area taken up by each individual adsorbed particle is also known, the surface area for that planar substrate can be calculated. The surface area in this case is simply the area of each adsorbate multiplied by the number of adsorbed particles at one monolayer. Typically, the surface area calculated this way is divided by the mass of the substrate in grams to give the specific surface area (SSA), which allows for a more convenient way of comparing the surface areas calculated in different experiments.

A simple, empirical method for determining monolayer capacity is the Point-B method [22] [47]. The Point-B method relies on being able to identify a sharp bend in certain isotherms which corresponds to the formation of a monolayer (or, as we shall see, an *effective* monolayer). This applies to isotherms

of types I, II, and IV, for the case of adsorption on substrates with strong interactions between substrate and adsorbate. In figure 3.6a, the dotted red line is used to help identify where the linear region after the bend begins and where the isotherm deviates from linearity. Point-B is located where the dotted red line and the isotherm separate. Monolayer capacity is taken to be the coverage at which Point-B is attained, and is indicated by the arrow.

The Point-B method can be used for isotherms resulting from adsorption on porous substrates [20] [25], which indicates the *effective* monolayer capacity. In such porous systems, the *effective* qualifier indicates that Point-B actually corresponds to a coverage which includes surface area but is mainly comprised of fully or partially filled pore volumes. Again, the isotherm in figure 3.6a is taken from a larger set of experimental data and is of an isotherm of argon adsorbed on chemically opened carbon nanohorns (a *very* porous substrate) at 82.07 K. This Point-B coverage can be used to calculate the effective specific surface area (ESSA) provided the mass of the substrate, and a good estimate for the amount of area taken up by an argon atom sorbed, are known. The ESSA, while obviously not an actual surface area, is still useful for obtaining a measure of the sorptive capacity of the substrate.

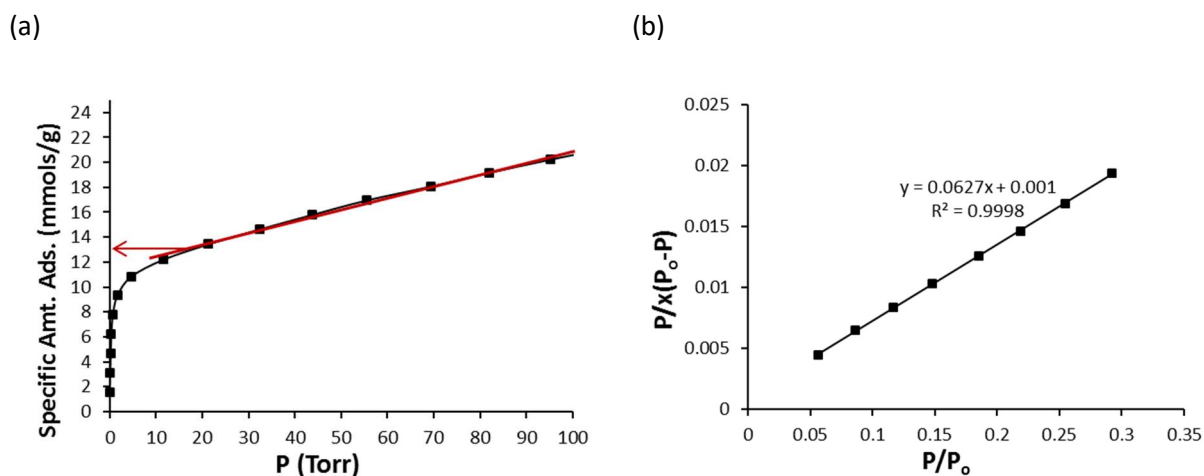


Figure 3.6: Demonstration of the Point-B method used for determining the effective monolayer capacity.

- (a) Isotherm from data of argon adsorbed on open carbon nanohorns at 82.07 K.
- (b) Point B linear plot for the same isotherm.

The BET method also provides a means for obtaining surface areas from experimental adsorption isotherms [22]. A glance at equation 1.7 shows that a graph of $P/x(P_o-P)$ vs. P/P_o should result in a plot with a slope (s) of $(c-1)/(x_m c)$ and an intercept (i) of $1/x_m c$ (see figure 3.6b). In many isotherms, within a relative pressure range of 0.05 and .35, this plot is linear (sometimes the region of linearity extends beyond that relative pressure range). By substituting in data from this pressure range of the isotherm, the values of (effective) monolayer capacity can be calculated as:

$$x_m = \frac{1}{s + i} \quad 3.13$$

The BET method of obtaining monolayer capacity and surface area measurements provides the most accurate values in cases where the substrate is planar and there is a sharp bend in the isotherm near Point B. This corresponds to a case where the value of c is large which occurs when the heat of adsorption is relatively high. Nitrogen is an example of an adsorbate which shows a sharp knee in many isotherms and is the most widely used adsorbate for the BET method of surface area determination [22].

The agreement between the Point-B and BET methods varies [22]. The best agreement seems to be in cases where Point-B is sharply (unambiguously) identified and occurs within the pressure range corresponding to the linear BET plot.

3.6 Isothermic Heat Calculations

Equation 2.8 is easily applied to experimental adsorption isotherms. We start by looking at the values of the natural logarithm of the equilibrium vapor pressure at chosen values of coverage for each isotherm. This is aided by the dotted lines displayed in figure 3.7, which shows two isotherms of argon

adsorbed on opened carbon nanohorns at temperatures of 76.32 and 82.07 K. The values of coverage indicated in the figure are 1, 3, and 5 mmols.

For each coverage, the values of $\ln(P)$ are then plotted vs the inverse of temperature of the corresponding isotherm, which is shown in figure 3.8a. The slope of these $\ln(P)$ vs. $1/T$ lines (each of which corresponds to a constant coverage) are multiplied by the negative of Boltzmann's constant (0.08617 meV/K) to arrive at the isosteric heat as a function of coverage, seen in figure 3.8b. These argon isotherms are part of a larger data set (as with figure 3.4) and will be included in more involved calculations in a later chapter.

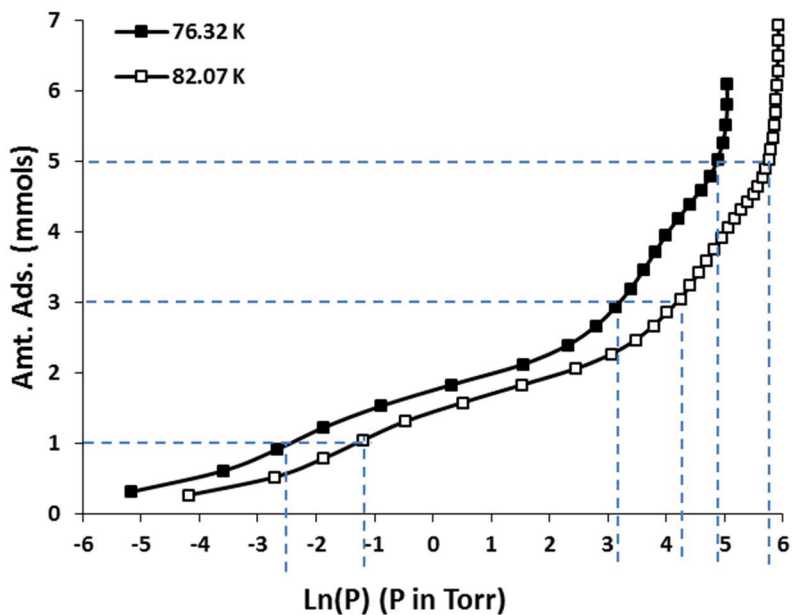


Figure 3.7: Demonstration of the method used to find $\ln P$ vs. $1/T$ data for isosteric heat of adsorption calculations. Isotherms are from measurements of argon adsorbed on open carbon nanohorns.

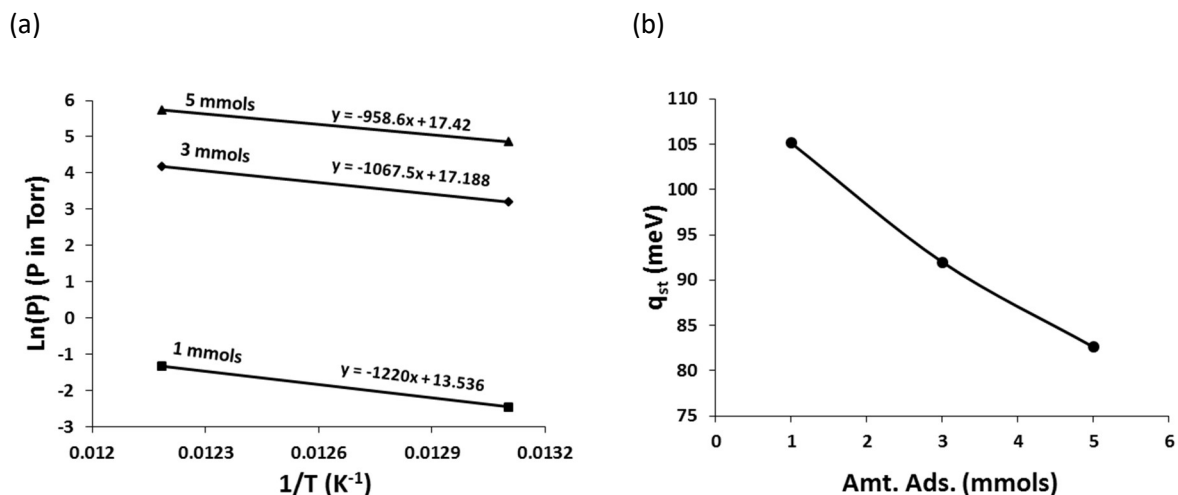


Figure 3.8: Demonstration of isosteric heat of adsorption calculation

- (a) $\ln P$ vs. $1/T$ data calculated from the isotherms in figure 3.8.
- (b) Isosteric heat as a function of coverage calculated from data in (a).

Typically, more than two isotherms and more than three coverages are used in these types of calculations. Adding more isotherms to the calculation results in values of q_{st} that are much more reliable. Similarly, adding more coverages results in a plot of q_{st} vs. coverage that is much more detailed which allows for the identification of features (typically, plateaus) corresponding to similar binding energy sites. At higher temperature ranges, the $\ln p$ vs $1/T$ lines at finite coverages might show lower slopes, indicating that an isosteric heat vs. coverage plot will be lower in magnitude as the average temperature increases. This due to an increase in the internal energy of the adsorbate and a corresponding decrease in the amount of energy given off (isosteric heat) as adsorption occurs.

Error bars can be generated for the isosteric heat vs. coverage plot by successively removing points from the $\ln(P)$ vs. $1/T$ plot and noting by how much the slope changes. The maximum and minimum attained by the isosteric heat calculation after such a procedure is the min/max of the error bars.

At the highest coverages, the isosteric heat calculation should yield the bulk heat of condensation, or deposition, of the adsorbate species depending upon whether or not the temperature range is above or below the triple point temperature. If our calculated bulk heat of condensation/deposition isn't within an acceptable proximity to the known value then we need to double check our methods.

The general shape of an isosteric heat plot involving an adsorption system with strong interaction between substrate and adsorbate will result in a plot which (overall) decreases as coverage increases as in figure 3.8b. The heat of condensation/deposition will be the high coverage, lowest energy limit. This dependence of the heat of adsorption on coverage can sometimes be reversed in situations where the interaction between adsorbate molecules is larger than the interaction between adsorbate and substrate, as will be seen in the case of CO₂ adsorption.

3.7 Derivative of the Isotherm Calculations

The term in parentheses in equation 2.13 can be obtained using adsorption isotherm data. The expression is approximated as,

$$\left(\frac{dN}{dP}\right) = \left(\frac{N_i - N_{i-1}}{P_i - P_{i-1}}\right) \quad 3.14$$

where the subscript i denotes the current point along the isotherm. Essentially the amount adsorbed of the previous point is subtracted from the amount adsorbed at the current point to approximate dN.

Similarly, the value of equilibrium vapor pressure at the previous point is subtracted from the current point to approximate dP. Equation 3.14 can be thought of as the derivative of the isotherm, and is

proportional to the isothermal compressibility. Plotting dN/dP (or sometimes the logarithm of dN/dP) vs. coverage allows for certain features in the isotherm to be shown with more clarity than they would be by just looking at an isotherm of coverage vs. pressure (or the natural log of pressure).

3.8 Kinetics of Adsorption Calculations

As detailed in section 3.2, the location of each point along an isotherm is calculated partly from an initial and final pressure value (all other quantities are held constant). The rate of change of the pressure vs. time plot (figure 3.3), and the time it takes for the pressure to reach a constant value corresponding to equilibrium, vary according to the adsorbate-substrate combination, as well as other variables (section 2.5).

The Linear Driving Force (LDF) model of equation 2.18 is useful for analyzing the kinetics of adsorption. Figure 3.9 shows plots of $\ln(1-\theta)$ vs. time, using the same pressure data from figure 3.3. To calculate the fractional uptake ($\theta=M(t)/M_{eq}$), the final equilibrium value of pressure is first used to find the equilibrium coverage (M_{eq}) via equation 3.5. For the mass loading at time t ($M(t)$), equation 3.5 is also used but with P_f replaced by the value of pressure at time t . This has been done for all three gauges and is shown in figure 3.9a. The steep region at the initial times is a result of gas rushing into the cell after the opening of V3 and the initial stage of adsorption. The steep drop at the very end of each plot is a result of equilibrium being attained as θ approaches 1 which causes the LDF plot to lose meaning since $\ln(0)$ is undefined. The time to reach equilibrium is different depending upon which gauge is chosen, and as a result, the lowest (most sensitive) gauge is usually used to determine the time it takes to reach the equilibrium value of pressure. In this case, the 1 Torr gauge is used to determine that the time to reach equilibrium is roughly 6 hours, or a little less.

The 1000 Torr gauge is less accurate and shows more noise at the lowest pressures, although it tracks pretty well with the 1 and 10 Torr gauges up until about 2 or 3 hours. In addition, the 1000 Torr gauge includes higher values of pressure in the initial region which are beyond the range of the lower gauges, allowing it show more detail in that initial time region. As a result, the 1000 Torr gauge is adequate to investigate values of the constant k of equation 2.18, if such information is useful. Whether the 1, 10, or 1000 Torr gauges are used to analyze this sort of kinetic data is dependent upon the specific adsorbate-substrate combination being studied and the pressures involved.

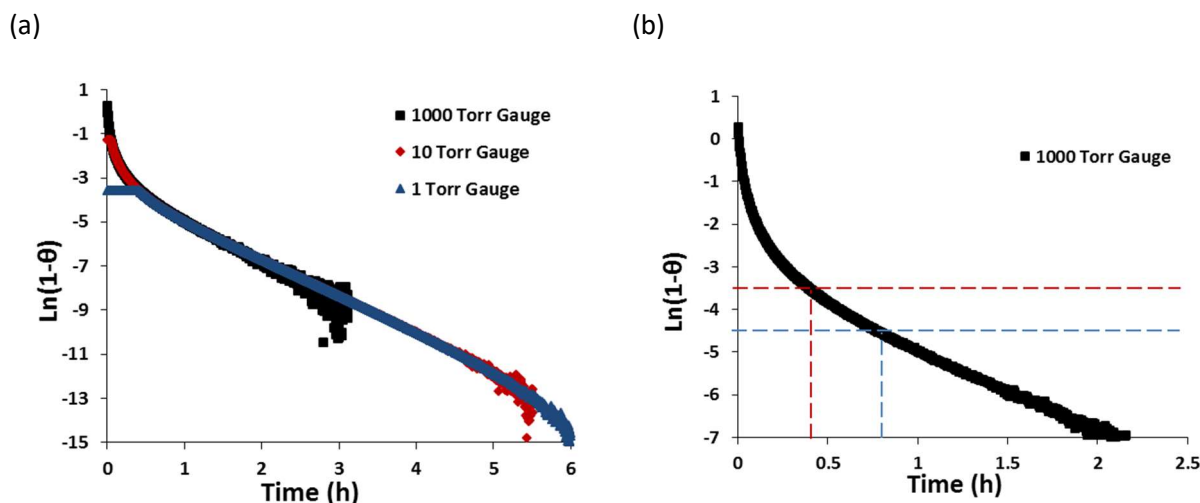


Figure 3.9: Linear Force Model plots applied to experimental pressure data. The fractional coverage (θ) is the amount adsorbed at time t divided by the amount adsorbed at equilibrium.

- (a) LDF plots for the full range of pressure corresponding to a point on an isotherm. Data was measured using all available pressure gauges.
- (b) LDF plot corresponding to the 1000-Torr gauge isolated. The red dotted line corresponds to $\theta = 0.97$ while the blue dashed line corresponds to $\theta = 0.99$.

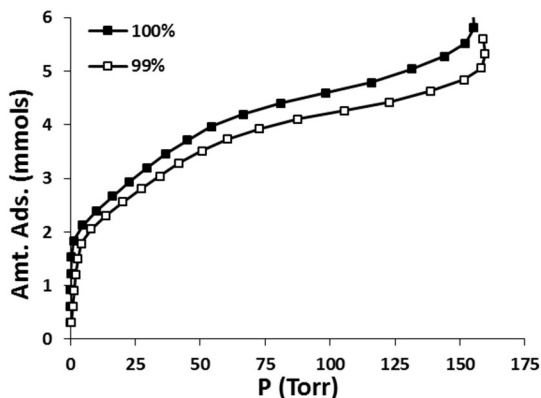
In certain cases, it is useful to know how long it takes to reach values of fractional loading that are 99% (or any other %) of the equilibrium loading. A method for doing this is demonstrated in figure 3.9b using data from the 1000 Torr gauge. The value of $\ln(1-\theta)$ when 99% of the mass has been adsorbed at a point is about -4.61 and is indicated by the horizontal blue dotted line. It can be seen that the time

to reach this 99% value of fractional uptake is somewhat over 0.75 h. Finding the time it takes to reach 97% of the equilibrium loading is similar and is indicated by the red dotted lines. A reason for doing this is that in some cases, the trends for the kinetics of adsorption for reaching full equilibrium differ from the trends pertaining to these “almost” equilibrium kinetics. Additionally, the closer the pressure comes to equilibrium, the more susceptible it is to variations due to electrical noise or room temperature variation. Sometimes this error makes the minimum time to reach equilibrium difficult to pinpoint.

For this particular example taken from argon adsorption on open nanohorns data a full 99% of the mass is adsorbed in less than 1 hour. However, it takes another 5 hours for the last 1% of mass to adsorb and for the system to reach thermodynamic equilibrium. For accurate adsorption isotherm measurements, it is necessary to wait this extra time to allow the system to come to complete equilibrium.

The question of whether or not waiting for just 99% of the mass to be adsorbed at a point and then prematurely moving on to the next point is addressed by considering figure 3.10 below. In the figure, isotherms of argon adsorbed on open carbon nanohorns at 76.32 K, are shown plotted linearly with pressure (on the left) and semi-logarithmically (on the right). The “100%” isotherms (filled squares) were calculated from equilibrium pressure values for all points. The “99%” isotherms (open squares) were calculated from the values of vapor pressure at only 99% of equilibrium loading for all points. The discrepancy is obvious for both plots. Any conclusions drawn from the location and pressure ranges of substeps in the “99%” data would be suspect. Additionally, certain calculations based on the data from these isotherms (isosteric heat, for instance), would likely be inaccurate if data from the “99%” isotherms were used. In such systems, it is better to wait for full thermodynamic equilibrium at all points along the isotherms depending upon what kind of information is to be extracted from the data.

(a)



(b)

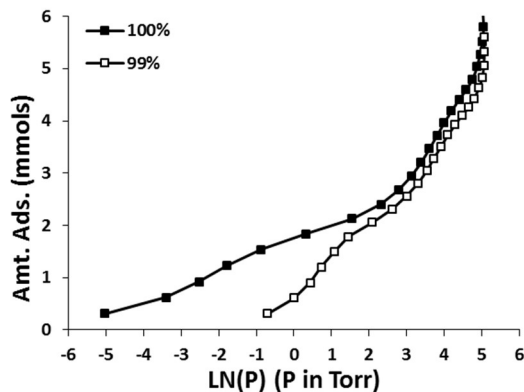


Figure 3.10: Isotherms calculated using equilibrium pressure as P_f (filled squares) and pressure at a fractional uptake of $\theta = 0.99$ as P_f (open squares).

(a) Linear isotherm

(b) Semi-logarithmic isotherm

Another useful quantity for displaying kinetics of adsorption data is the fractional pressure change (FPC). It is simply defined as the difference between the pressure at time t and the equilibrium pressure, divided by the equilibrium pressure. The plots of FPC vs. time will look very similar to the pressure vs. time plots such as those of figure 3.3. The usefulness of FPC plots is that they allow more data to be shown with clarity in the same graph for the sake of comparison of kinetics of adsorption calculations. Often they will be plotted with the FPC axis displaying arbitrary units; the individual curves will be displaced either upward or downward for the sake of clarity, and comparisons of equilibration times.

3.9 Error Analysis for Pressure Measurements and Temperature Calibration

The pressure measurements, like those of figure 3.3, are subject to a certain amount of electrical noise, room temperature variations, and other instrumental errors. Additionally, pressure

measurements at low pressure will be subject to systematic error based on any minute outgassing within the system, or leaking to or from the atmosphere.

The error analysis was carried out as follows: First, an amount of atmosphere was let into the dosing volume of only of one of the setups (the air was not exposed to an adsorbent). The pressure was then recorded over a roughly 24 hour period, with the data points recorded at 1 minute intervals. This process was repeated for systematically increasing pressures starting at roughly 0.01 Torr and ending at room pressure. Leak rates and standard errors were then calculated using the lowest scale pressure gauge that was in range. The standard error was calculated using the “standard error of estimate” function (=steyx) in Excel. The standard error of estimate is essentially a more general form of standard deviation, and is a measure of the spread of values about the curve or line of best fit. The results are summarized in table 3.2 and figure 3.11.

Table 3.2: leak rate and standard error analysis from experimental pressure data at various approximate pressures.

<u>Approximate Pressure (Torr)</u>	<u>Leak Rate (Torr/h)</u>	<u>Std. Error (Torr)</u>
0.01	+ 0.0002	±0.00005
0.1	+ 0.0001	±0.00004
1	+ 0.00008	±0.0002
10	-	±0.002
100	-	±0.016
760	-	±0.1

It can be seen in table 3.2 that leak rates were only resolvable at the three lowest pressures, all using the 1-Torr gauge. This, of course, does not imply that there is no leaking at higher pressures, just that the higher scale gauges don’t resolve the leak rates which are negligible at those pressures anyway. A leak rate of approximately 0.1 to 0.2 milli-Torr per hour is small but does introduce a measure of

systematic error at low enough pressures. For most adsorption experiments, this systematic error is a small deviation. It is, however, not always negligible for adsorbing systems with longer than usual equilibration times which can occur when linear adsorbates are adsorbing on highly porous substrates.

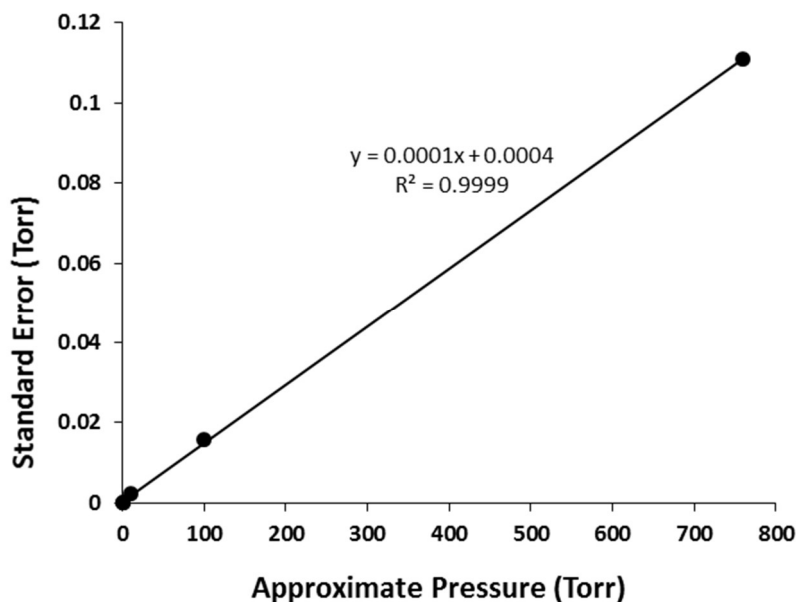


Figure 3.11: Standard error is calculated from the data of the lowest scale gauge for the approximate dosing volume pressure being considered.

The standard error is shown graphically figure 3.11. Standard error increases linearly as the pressure of the system increases up to roughly room pressure (about 760 Torr). The trend line equation (with y being the standard error and x being the approximate pressure) can be used to determine the standard error at pressures intermediate between the data points given the R^2 value of 0.9999. As an example, a recorded equilibrium pressure of 214.884 Torr from the 1000-Torr gauge would have a standard error of ± 0.02 Torr, using the equation in figure 3.11 and keeping one significant digit. Additionally, the equipment manual for the MKS Baratron Type 220D pressure transducers that we use, gives a value of accuracy (accuracy includes non-linearity, hysteresis, and non-repeatability) of ± 0.32

Torr. Taken together with the standard error above, the overall uncertainty is ± 0.34 Torr. Thus, the pressure of 214.884 Torr would perhaps be more appropriately reported as 214.88 ± 0.34 Torr.

This uncertainty has implications for the calibration of isotherm temperatures. For instance, if the pressure of 214.88 ± 0.34 Torr was a measure of the saturated vapor pressure of an adsorbing system, the standard error would have to be carried through the calculation of the isotherm temperature. As an example, I performed this calculation using the Antoine Equation (equation 3.12) with the pressure stated above as saturated vapor pressure with one of the sets of Antoine Equation coefficients provided for the case of propane vapor/liquid from the NIST website. By working through the calculation and carefully keeping track of significant figures I came up with a temperature of 205.93 ± 0.03 K: an uncertainty of about 30 mK.

We can see the effect of using a lower pressure (and lower scale gauge) by considering a saturated vapor pressure of 2.1488 instead of 214.88 Torr. A measurement of 2.1488 Torr from the 10-Torr gauge gives a standard error from the equation in figure 3.11 as ± 0.0006 Torr. The uncertainty in accuracy for the 10-Torr gauge from the manual is calculated as ± 0.0032 Torr (the same as the 1000 Torr gauge for the calculation in the previous paragraph). Thus, the pressure with total uncertainty is 2.1488 ± 0.0038 Torr. Performing the same calculation as from the previous paragraph with the Antoine Equation using the new pressure yields a temperature value of 155.04 ± 0.01 K.

For the sake of completeness we can take this to the high extreme: near the pressure limit of the 1000-Torr gauge. For a hypothetical saturated vapor pressure measurement of 1000.0 Torr, the uncertainty from the equation in figure 3.11 is ± 0.1 Torr. From specifications in the manual, the systematic uncertainty in accuracy is calculated as ± 1.5 Torr, so the pressure with total uncertainty is 1000.0 ± 1.6 Torr. Carrying through the same calculation as above using the same coefficients for propane gives a temperature of 237.41 ± 0.04 K.

To recap all of this, the uncertainty in the calibrated temperatures decreased from 40 mK, to 30 mK, and finally to 10 mK, for hypothetical saturated vapor pressures of 1000.0 ± 1.6 Torr, 214.88 ± 0.34 Torr, and 2.1488 ± 0.0038 Torr, respectively. It should be noted that these uncertainty measurements for the temperatures are for the specific case of one set of Antoine coefficients for the propane. Using a different set of coefficients for the same gas, or for a different gas, might yield different uncertainties.

Alternatively, liquid/vapor saturation data plots are available from NIST, and using such a plot might lead to different levels of uncertainty in the temperature. A method for determining uncertainty in temperature by using the data plots from NIST is to find the temperature at the maximum and minimum values of the saturated vapor pressure and to use that range of values as the uncertainty in temperature. I did this for propane data using the value for saturated vapor pressure of 214.88 ± 0.34 Torr from above, and came up with a temperature value of 205.90 ± 0.03 K; the same 30 mK of uncertainty as above.

With the way I've calculated it here, most of the uncertainty originates in the systematic error that is inherent in the MKS Baratron Type 220D pressure transducers, even at the highest pressures where the calculated standard error from experimental data in table 3.9 is the highest.

CHAPTER 4

SUBSTRATES

4.1 Carbon Nanotubes

Although carbon nanotubes might have been unintentionally produced as early as the late 19th century [9], Sumio Iijima is often credited as the first researcher to produce and identify their structure [9] [48], using an electric arc discharge apparatus [49] [50] in 1991. Carbon nanotubes are a form of single layer hexagonal carbon (graphene sheets) arranged in a hollow cylinder formation, as shown schematically in figure 4.1. Two types of carbon nanotubes are multi-walled carbon nanotubes (MWCNTs) and single wall carbon nanotubes (SWCNTs). MWCNTs are comprised of more than one cylindrically arranged concentric layer of graphene with a separation between layers of 0.34 nanometers (slightly greater than the typical spacing between layers in graphite) [48]. They can be up to several microns in length with an outer diameter of anywhere between 2 and 25 nanometers depending upon the number of layers present [48]. SWCNTs are composed of only one cylindrical sheet of graphene. These can be up to several microns in length with a typical diameter of between 1 and 2 nm [48]. In their as-produced forms, both MWCNTs and SWCNTs are blocked at the ends by hemispherical caps.

At least three major methods exist to produce carbon nanotubes [9]. The arc discharge method (used by Iijima) involves producing an arc between two carbon electrodes packed with a transition metal and graphite powder in an inert gas environment. The arc vaporizes the carbon and the nanotubes deposit on the negative electrode. Laser ablation is another method which involves using a laser (often CO₂ or YAG) to vaporize carbon which can then deposit as nanotubes on a substrate. The laser is focused on a target composite consisting of carbon doped with catalytic metals in an inert gas environment. Chemical vapor deposition (CVD) is a method in which a chemical reaction of a mixture of carefully

selected vapors (one of which is a hydrocarbon) also results in the deposition of carbon nanotubes on a substrate. CVD seems to be the simplest and most economically feasible method for producing large quantities of either type of nanotube: multi-walled or single-wall [9].

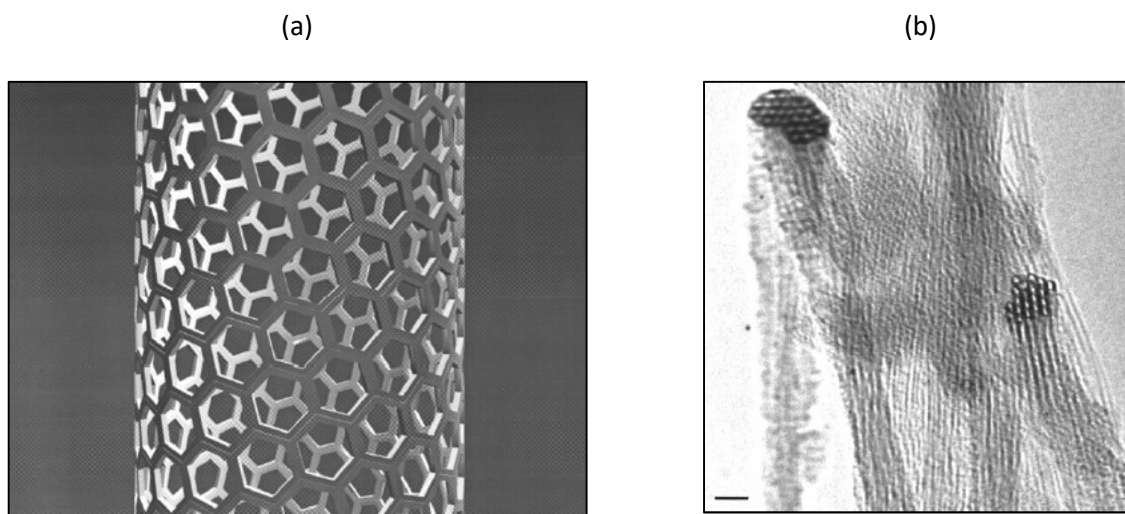


Figure 4.1: Both images are reproduced from reference [48].

(a) Schematic of a SWCNT showing the hexagonal carbon arrangement.

(b) TEM image of SWCNT bundles. The scale bar in the bottom left corner is 5nm long.

Owing to the existence of van der Waals interactions, SWCNTs will often form bundles of up to 200 nanotubes [51]. Within these bundles, the individual nanotubes will mostly be parallel to each other and arranged in a triangular array when viewed end on as seen in figure 4.1. A schematic of a perfectly homogeneous SWCNT bundle is shown in figure 4.2. The two black disks in the upper left corner are to show the kinetic diameters of He (0.26 nm) and Xe (0.48 nm), which are roughly to scale if the generic SWCNTs depicted in the figure are assumed to be 1.5 nm in diameter.

In addition to being of fundamental physical interest for adsorption studies, the potential applications of carbon nanotubes are many due to their electronic, mechanical, thermal, and magnetic properties [9]. Some of these uses include gas storage, molecular filtration systems, chemical sensors,

and nano-electronic devices [9]. For chemical sensing in particular, adsorption and desorption of gas molecules are often integral parts of the process [10]. One method for chemical sensing via adsorption/desorption processes is based on the fact that for carbon nanotubes, the electrical properties (resistance, density of states, thermoelectric power) can change when the material is immersed in a different chemical environment [10]. Methods can be employed to measure the changes in those electrical properties. Several criteria are important when considering a material for gas sensing applications and these criteria include molecule sensitivity and selectivity, and response and recovery times [10]. Those gas sensing criteria can be investigated via adsorption experiments.

Four potential binding energy sites are depicted in figure 4.2 which are indicated by the arrows and labels. The nanotube interiors are not available for adsorption in the as produced form. However, the ends of the nanotubes can be opened making the interiors available for adsorption to certain adsorbates if the nanotubes are subject to appropriate chemical or mechanical treatment. Further heating is needed after the purification to remove functional groups that attach during the purification process [52]. The interstitial channels are the spaces in between the nanotubes and are unavailable for adsorption in the case of homogeneous, pure, bundles [53]. The interstitial channels can become available for adsorption if defects are present, or if the nanotube bundles are inhomogeneous with regard to their individual diameters. Either scenario can cause a portion of the interstitial channels to increase in effective diameter, allowing sufficiently small guest particles to adsorb within. The groove sites are located at the intersection of two external nanotubes and are generally available for adsorption. Along these groove sites (which constitute the highest binding energy sites when the interstitial channels and interior of the nanotubes are inaccessible) quasi 1-D films can form [51]. Experimental realization of matter confined in one dimension is of fundamental interest [51]. An example of quasi 1-D confinement in the groove phase can be seen in figure 4.2b for the case of a hypothetical adsorbate indicated by the red disks. The convex outer surfaces of the individual nanotubes

on the periphery of the bundles are also available for adsorption. Adsorption will occur on these convex outer surfaces line by line starting at the site nearest the groove phase and moving outward until a monolayer is built up. The number of lines that can form along the outer convex region of the nanotubes in a bundle before the monolayer is complete depend on the size of the adsorbate [54]. For instance, Xenon forms at least three lines on the outer convex region of the nanotubes while Argon can form up to six lines [54]. CF_4 , on the other hand, has been shown to only form two lines along the outer convex surface before the completion of one effective monolayer [55].

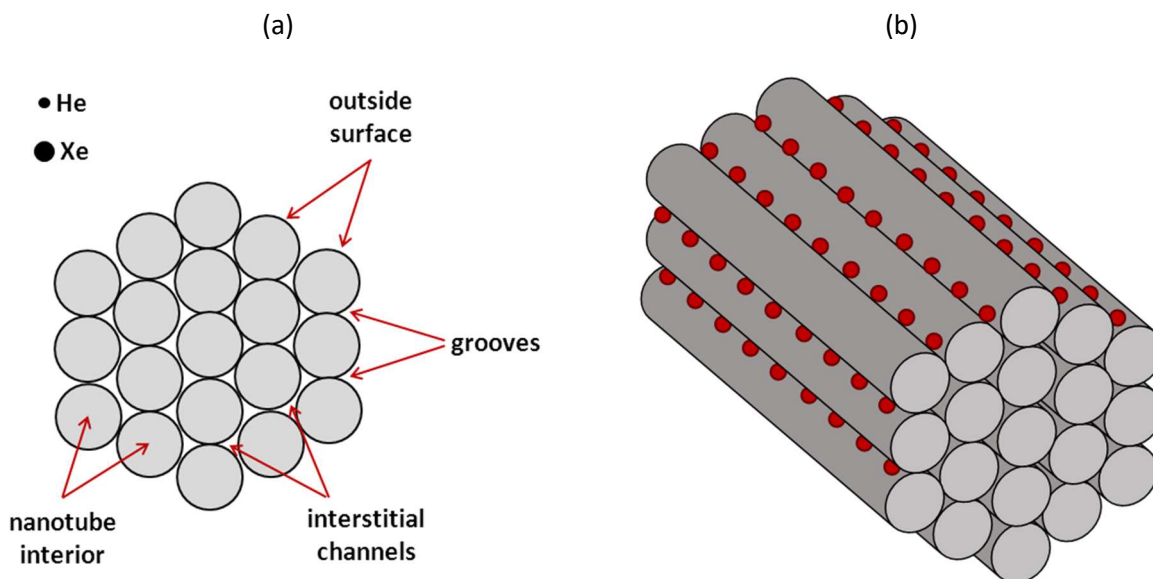


Figure 4.2: Generic homogeneous SWCNT bundle

- (a) Bundle viewed end-on. He and Xe are shown roughly to scale by the black disks. Four adsorption sites are labeled and indicated by the arrows.
 (b) An adsorbate (red circles) filling the quasi-1D groove layer.

SWCNT bundles constitute an energetically heterogeneous system possessing a degree of porosity which depends largely on whether or not the interstitial channels and nanotube interiors are available for adsorption. When the ICs and interiors are unavailable for adsorption, specific surface area

measurements will give similar values for adsorbates of different cross-sectional areas measured at similar reduced temperatures [56], indicating that they occupy the same sites (i.e., the grooves and outer convex surfaces) regardless of their size. For instance, Ne, Ar, CH₄, and Xe give values for effective specific surface area of 450, 468, 464, and 455 m²/g, respectively, when adsorbed on SWCNTs [56]. These values are all in very good agreement despite the size difference of the adsorbates used in that study. Having surface area measurements in agreement like that is similar to the way in which adsorbates of different sizes should yield similar values for surface area when they adsorb on the same planar substrate, although I should stress again that SWCNT bundles are far from being planar.

Semi-logarithmic isotherms of many adsorbates reveal at least two easily resolvable substeps corresponding to the binding energies of the adsorption sites being occupied [51]. Assuming the ICs and interiors are again unavailable for adsorption, the lowest-pressure/highest-energy substep corresponds to adsorption on the grooves while the higher-pressure/lowest-energy substep corresponds to adsorption on the outer convex surfaces [51]. Adsorbates for which semi-log isotherm substeps are easily resolvable include Xe [54], Ar [54] [57], Ne [56], CF₄ [55], H₂ [57], and O₂ [57]. Other adsorbates, however, show isotherms with smoothed out substeps or no substeps at all when adsorbed on SWCNTs. This can be for various reasons such as effects due to adsorbate linearity as is the case for propane and longer alkanes [58]. Effects due to permanent electric moments of adsorbates can also cause isotherm substep smoothing which is the case for carbon dioxide [57].

The isosteric heat of adsorption has been measured as a function of coverage for many adsorbates on SWCNTs. The trend for most is that the energy decreases as coverage increases until the value corresponding to the bulk heat of condensation or deposition is reached. This is true for a series of linear alkanes (ethane, propane, and butane) [58], H₂, D₂, O₂, Ar, CH₄ [57], and CF₄ [55]. A notable exception to that trend is for the case of CO₂ in which the energy *increases* as coverage increases towards the bulk value [57]. That fact will be discussed more thoroughly later in this dissertation and our

experimental results will be compared to those from the Bienfait study [57]. For adsorbates which form distinguishable phases corresponding to adsorption on the groove and outer surface sites (Xe and Ar, for example) the heats of adsorption for the groove sites are greater than those for graphite, while the heats of adsorption for the outer convex sites are less than those for graphite [51].

Trends for adsorption kinetics on carbon nanotubes have been explored for many adsorbates. For adsorption of H₂ and CF₄ on the grooves and external surfaces of nanotube bundles [37], equilibration times were shown to decrease with increasing coverage for individual isotherms. Also, for a set of isotherms of the same adsorbate-substrate combination, equilibration times decrease as temperature increases for a given coverage. Similar kinetic trends were also observed for Ar and CH₄ adsorption on close ended SWCNTs [59]. Additionally, wait times decrease as the binding energy of the adsorbate decreases since the lower the binding energy, the more pressure is needed for a given site to be filled [37]. Essentially, higher pressure means more atoms or molecules are available for adsorption and so the sites get filled faster.

Somewhat different trends occur for adsorption kinetics of linear alkanes on close ended SWCNTs [60]. Kinetics for methane and ethane follow the same trends just discussed in the previous paragraph. The trends for propane and butane, however, are reversed in some aspects; for those two longer alkanes, the time to reach equilibrium *increases* as coverage increases along an isotherm. The reason for this reversal, speculated in that same reference, is that longer adsorbates (such as pentane and butane) pack less efficiently which leaves open potential adsorption sites and the adsorbate must reorient as coverage increases for more molecules to fit into those available sites.

4.2 Carbon Nanohorns

Single wall carbon nanohorns (SWCNHs) are another form of graphitic carbon similar in many ways to SWCNTs. They were first produced by Iijima using a laser ablation technique similar to that which was used to produce carbon nanotubes with the exception that no metal catalyst was present for the case of nanohorn production [61]. A nanohorn can be thought of as a horn shaped nanotube which ends in a roughly 20 degree taper, rather than a half hemispherical cap as in close ended SWCNTs. The length of a typical nanohorn is 30 to 50 nm, while the width of the cylindrical region away from the tapered tip is 2 to 5 nm (slightly wider and more irregular in diameter than a typical SWCNT). Much like the way in which SWCNTs form bundles, SWCNHs can form into one of at least four different varieties of aggregates: dahlia-like [62], bud-like [62], seed-like [11], and petal-like [63]. Each has a slightly different morphology.

Dahlia-like, and Bud-like aggregates can both be formed by a procedure involving a CO₂ laser vaporization technique [62]. In that technique, a graphite rod 50 mm long and 30 mm in diameter is focused on by a CO₂ laser of wavelength 10.6 μm. Nanohorn aggregates form in the vapor that is produced. The vaporization experiments are executed at room temperature but a buffer gas is run through the chamber at a controlled pressure. The variety of aggregate that is produced is dependent upon the gas and pressure used in the experiment. If Ar is used as the buffer gas at a pressure of 760 Torr, dahlia-like aggregates form with a yield of 95% (the other 5% being bud-like). If He, or N₂ gas is used at a pressure of 760 Torr, bud-like aggregates form with yields of 70 and 80%, respectively.

Dahlia-like aggregates (figure 4.3) are spherical [61] [62], and are arranged such that the ends of the nanohorns stick out and are roughly situated in a radial manner. The overall diameter of a typical dahlia-like aggregate is 80-100 nm. The regions in between the individual nanohorns in the aggregates are roughly conical, and the walls of the nanohorns are largely intact in the as-produced form.

Bud-like aggregates are similar [62] with the exception that the individual nanohorns do not protrude outward from the aggregate and remain encapsulated within the sphere.

Petal-like aggregates have been observed to form as a result of a modified CO₂ laser vaporization technique [63] which increased the yield of nanohorns to 1 kg/day. Petal-like aggregates are similar in size to dahlia-like aggregates. The defining characteristic of petal-like aggregates is that they contain up to 10 or more graphite-like plates which resemble the petals of a flower protruding from the spherical aggregate. These plates are up to 50 nm wide and 2 to 3 nm thick and are made of 5 to 10 graphene sheets.

Seed-like aggregates are characterized by a nanohorn tubule shape which is thin and bumpy [11].

Holes can be formed in the nanohorns by a procedure involving oxidation in air followed by hydrogen peroxide treatment [64]. The oxidation is carried out by slow combustion. This involves a slow increase in temperature up to between 300 and 600°C in air. The drawing in of carbonaceous dusts is a concern for adsorption experiments since it would reduce the surface area available for sorption. This method of slow combustion has been shown to generate few of these carbonaceous dusts [64].

The conical morphology of the porous regions in both open and closed dahlia-like nanohorns (figure 4.4) is fairly unique. This makes them an interesting adsorbent since it allows researchers to study the physics and chemistry of matter confined in conical pores. There are various applications for carbon nanohorns as well. Changing the size of the holes in opened nanohorns allows them to be used as molecular sieves [11]. Other uses include supporting chemical catalysts, doping with Pt and using them as electrodes in fuel cells, and as nano-sized reaction chambers [11]. One particularly interesting application is drug delivery. Chemically opened nanohorns have a size and shape well suited to drug delivery applications and in particular can carry and supply the anti-cancer drug cisplatin to cancerous

tissue [12]. A material's use as a drug carrier depends on its ability to retain the drug as a guest particle within its structure and hold on to the drug long enough to reach the unhealthy tissue for delivery [12]. In principle, adsorption experiments such as those presented later in this dissertation can shed light on such material properties.

Four potential adsorption sites have been identified in aggregates of dahlia-like SWCNHs (which is the type of aggregate used in the experimental studies in this dissertation) and they are shown in figure 4.4 in an idealized manner. The aggregates constitute a very heterogeneous substrate and in reality, the division into four clear and distinct adsorption sites is a simplification. The binding energy can vary smoothly between the conical regions and the surfaces and a real image of an aggregate shows a much more chaotic arrangement [61], as seen in figure 4.3.

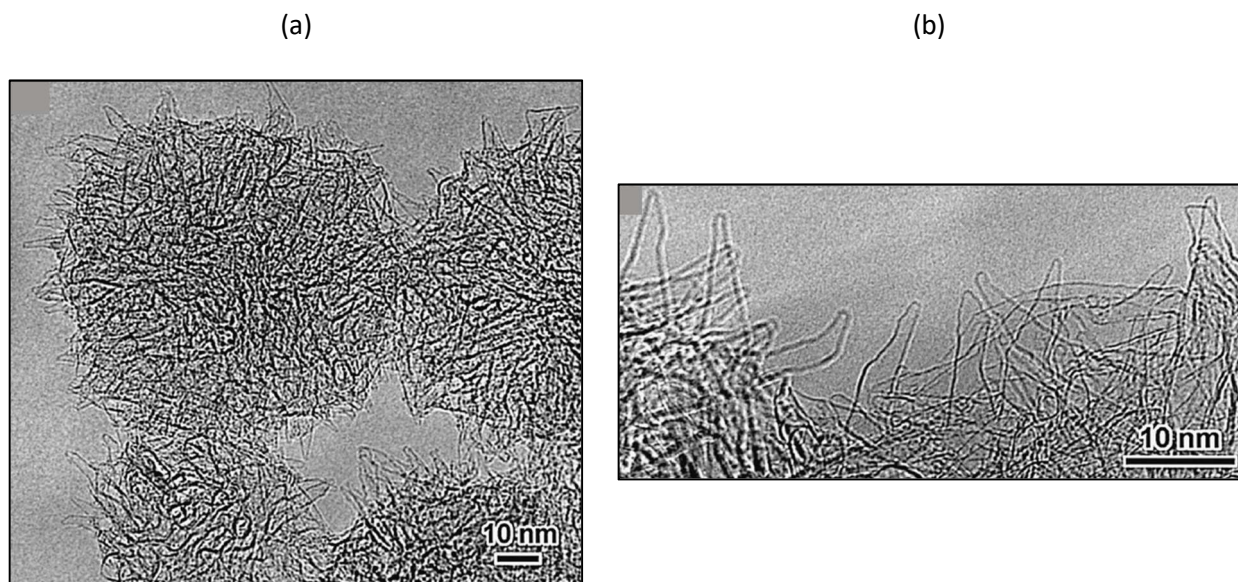


Figure 4.3: TEM micrographs of dahlia-like nanohorn aggregates reproduced from ref [61]

- (a) A few spherical aggregates
- (b) Close up of individual nanohorns sticking out from the aggregates.

In the closed (as-produced) form of dahlia-like nanohorn aggregates, two of the adsorption sites of figure 4.4 are accessible by adsorbates: the interstitial pores and the exterior surfaces. In a comparative theoretical and experimental study involving Ne and CF₄ adsorption on closed nanohorns, these two different adsorption sites were modeled theoretically as having two different discrete binding energies [65]. Though an approximation, this resulted in favorable comparisons between the theoretical and experimental isotherms which showed that there are two substeps in the isotherms corresponding to the two different adsorption sites accessible to Ne and CF₄. A low coverage/high binding energy substep corresponded to adsorption in the interstitial pores while a high coverage/lower binding energy substep corresponded to adsorption on the external surface sites. This was true for both Ne and CF₄ even though their sizes are different which was attributed to the roughly conical morphology possessed by the nanohorn aggregates [65].

In the chemically opened variety in which holes have been formed in the nanohorns, all of the adsorption sites of figure 4.4 are potentially accessible by adsorbates. However, experimental semi-logarithmic isotherms of Ne on opened nanohorn aggregates still only show two substeps corresponding to binding energy sites [66]. This is because the binding energy for the intra-nanohorn pores and the interstitial pores are similar, and therefore both regions become occupied by adsorbate at roughly the same pressure. The interior and exterior surfaces also have similar binding energies and therefore also get filled by adsorbate at roughly the same pressure.

Unlike bundles of as produced SWCNTs, nanohorn aggregates are highly porous and will show different effective surface areas depending upon the size of the adsorbate. The pores are conical, and therefore smaller adsorbates will be able to fill the deeper regions more effectively, and will give higher values of effective specific surface area relative to larger adsorbates. This applies to both opened and closed nanohorns since the pores are conical in either case. For the closed nanohorns, ESSA values have been reported for the adsorption of Ne, CO₂, and CF₄, as 393, 358, and 288 m²/g, respectively [67]. These

values were calculated from effective monolayer capacity measurements taken from isotherms at a relative temperature of roughly 0.57 (in those studies, the critical temperature was the scaling factor). Neon has the highest ESSA of those three because it is the smallest adsorbate here, while CF_4 has the smallest ESSA because it is a larger molecule than the other two. On chemically *opened* nanohorns, values of the ESSA for Ne, and CO_2 have been reported as 1077, and 850 m^2/g , respectively [66]. The increase of a factor of roughly 2.5 in the ESSA of opened nanohorn aggregates compared to closed aggregates is readily understandable given the additional adsorption sites that are available as a result of the opening of the nanohorns.

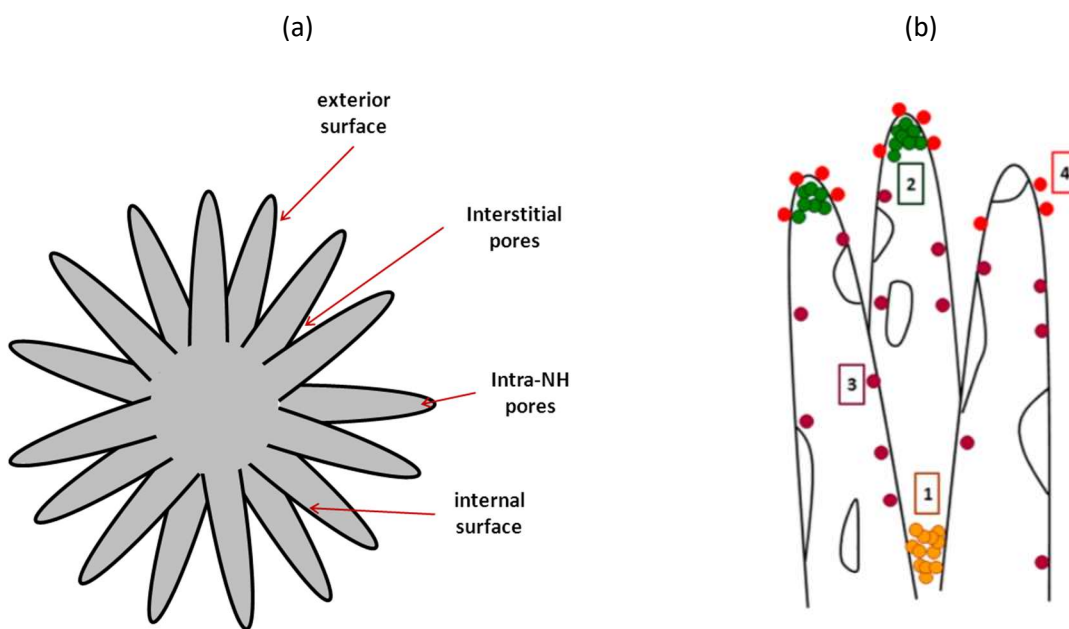


Figure 4.4: Schematic Nanohorn Figures

- (a) Schematic of a cross-section of a generic dahlia-like nanohorn aggregate. Adsorption sites are labeled and indicated by the arrows.
- (b) Hypothetical adsorbate occupying the different adsorption sites:
1. Interstitial Pores
 2. Intra-Nanohorn Pores
 3. Internal Surface
 4. External Surface

Isosteric heat as a function of coverage measurements have also been obtained from the same references in the previous paragraph. For Ne and CF₄ on closed nanohorns, the isosteric heat decreases as coverage increases and both plots display plateaus corresponding to binding energy sites and bulk latent heat. For CO₂, the isosteric heat is less than the bulk latent heat for most of the coverage range which is a behavior seen in many studies involving CO₂ adsorption. This is discussed in more detail in the section concerning CO₂ adsorption on SWCNTs in this dissertation. For Ne and CO₂ adsorption on open nanohorns, the same trends are observed as in the closed nanohorns, with the exception that Ne shows a clearer substep at lower loading corresponding to high binding energy sites.

Kinetic results have only been obtained thus far for the case of Ne and CO₂ adsorption on open nanohorns [66]. In that reference, neon adsorption kinetics show that as the coverage increases, the time to reach equilibrium decreases. This is a common trend for gases adsorbed on planar substrates because as the pressure increases (at higher coverages) more adsorbate is available for adsorption and the sites get filled faster. For CO₂ the trend was reversed; the time to reach equilibrium *increased* as the coverage increased. The change in kinetics in that reference was attributed to the difference in the relative strength of the adsorbate-adsorbate and adsorbate-substrate interaction. The adsorbate-substrate interaction for CO₂ is effectively reduced due to the effects of its permanent quadrupole moment.

4.3 Zeolitic Imidazolate Framework-8 (ZIF-8)

Metal organic frameworks (MOFs) are materials with crystalline structures consisting of alternating metal units and organic ligands [68]. These materials are made using a process called reticular synthesis which involves constructing the material piece by piece using molecular building blocks [68]. This method is more directed than most other methods which historically depended in large

part on happenstance. Using reticular synthesis, MOFs can be tailored to have specific predetermined physical and chemical properties such as high stability, tunable metrics, organic functionality, and porosity. As many as 11,000 or more varieties of MOF exist [68]. The robustness and the scaffold-like nature of many MOFs yields structures with very high porosity. For instance, effective surface areas have been reported as high as 2900 m²/g [68].

A particular variety of MOF are the zeolitic imidazolate frameworks (ZIFs) [13]. In ZIF materials, imidazolate (C₃H₃N₂) is the organic linker which connects tetrahedral metal units. In ZIFs, the metal-imidazolate-metal bond angle is close to 145° which is similar to the bond angle of Si-O-Si in zeolite materials. Zeolites are crystalline porous materials used in industrial applications such as petrochemical cracking, and ion-exchange. The synthesis of ZIFs is part of the effort to incorporate transition metals and organic units into the zeolite structure [13]. One property of ZIFs that makes them unique amongst the MOF materials is that they possess exceptional chemical and thermal stability, and a promising application for ZIF materials is in the field of catalysis [13].

The imidazolate linkers and tetrahedral metal units of ZIFs can be combined into many different topologies [13]. For instance, a few varieties of ZIFs (ZIF-7, ZIF-8, and ZIF-9) possess a structure similar to the mineral sodalite [13]. This sodalite structure is shown for ZIF-8 in figure 4.5a. In ZIF-8, the metal in the tetrahedra is zinc and the individual cells shown in figure 4.5a are connected by 4 membered rings (red squares) and 6 membered rings (blue hexagons). Figure 4.5b shows one of the cells of ZIF-8 with more detail. From single crystal x-ray analysis of ZIF-8, the 6 membered rings are 3.4 Å in diameter while the 4 membered rings are of much smaller diameter [13]. The open space within the cages (indicated by the yellow sphere in figure 4.5b) are 11.6 Å in diameter [13]. As with many MOFs, the scaffold-like nature of ZIF-8 which leads to large porosity yields large values for the effective surface area calculated from adsorption isotherms. For ZIF-8 this value of surface area based on Type I nitrogen isotherms (indicating microporosity) and the BET method gives a value of 1,947 m²/g [13]. The pore volume is

given as $0.663 \text{ cm}^3/\text{g}$ [13]. The thermal and chemical stability of ZIF-8 have also been shown to be remarkable [13]. Thermal stability refers to the material's ability to retain its structure as the ambient temperature is increased; it can be determined by thermal gravimetric analysis. Chemical stability can be determined by placing the material in various solutions (such as water, benzene, or methanol) at temperatures near the boiling points for those respective substances and measuring how long the material retains its structure.

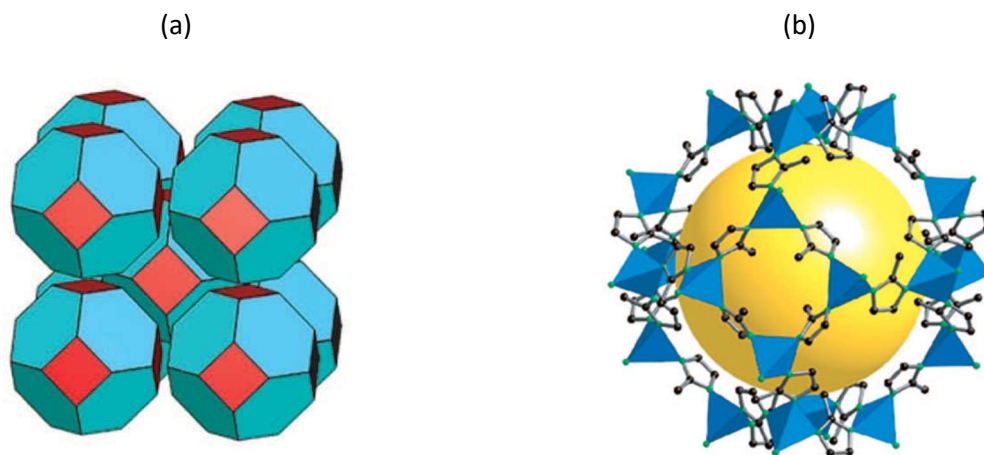


Figure 4.5: Structure of ZIF-8 reproduced from reference [13].

(a) Tiling diagram showing the sodalite structure.

(b) Single cage with ZnN_4 tetrahedra in blue. Imidazole linkers are in between the tetrahedra.

High pressure diamond-anvil experiments demonstrated that ZIF-8 has a flexible framework [69]. It was reported that while ZIF-8 was submerged in a hydrostatic medium consisting of methanol and ethanol at a pressure of 1.4 GPa and at room temperature, the organic imidazolate ligands reoriented themselves causing an increase in the size of the channels linking the individual cages of ZIF-8. The result of this is an increase in the effective pore volume as it allows for the passage of particles through the six-membered windows that would otherwise be too large to fit. Since there are two different structures depending upon the experimental conditions, ZIF-8 is referred to by two different

names: ZIF-8 AP for the as-produced structure at room temperature and pressure, and ZIF-8 HP for the high pressure structure with increased pore volume and effective surface area. Diagrams of both structures of ZIF-8 can be seen in figure 4.6. This rotation of the organic imidazolate linkers and the corresponding increase in available pore volume has been termed “gate-opening.”

Evidence is presented in various studies [70] [71] [72] [73] that the gate-opening effect in ZIF-8 can also be induced by sorption at low temperatures and pressures. In one study by Ania et al. [70], adsorption studies were conducted on ZIF-8 at two temperatures (77.3 and 90.2 K) for four different gases: Ar, O₂, N₂ and CO. Multiple substeps were reported in the isotherms for all the studied gases at pressures below that of the respective saturated vapor pressures. One low coverage substep was attributed to adsorption on ZIF-8 AP for all gases. For Ar and O₂, an extra substep was present before saturation which was attributed to adsorption on the ZIF-8 HP structure. Essentially, for a given temperature, gate opening occurs at a certain threshold pressure or degree of sorbent loading for each gas which causes a sudden increase in available pore volume and results in increased uptake and a substep in the isotherm. For N₂ and CO there was also reported a substep corresponding to adsorption on the ZIF-8 HP structure as well as a third substep. This third substep was located at a coverage intermediate between those corresponding to adsorption on the AP and HP structures and was attributed to rearrangement of adsorbed particles as a result of electrostatic effects due to the polar nature of N₂ and CO [70] Desorption data was also provided in the study by Ania, et. al. [70], for all of the gases studied. It was remarked that the pressures at which the desorption branches depart from and reunite with the adsorption branches are not consistent with capillary condensation in mesopores and is likely due to the occurrence of gate opening [70].

A temperature dependence of the structural transition was hinted at in the study by Ania et al. [70]. This temperature dependence has been further explored in a few other studies [73] [72]. Gallaba et al. measured seven isotherms of Xe adsorbed on ZIF-8 at temperatures between 95 and 160 K. Of those

isotherms, the five measured below 148 K showed a clear gate-opening related substep. As temperature increased, the G.O. substep moves progressively closer to the step corresponding to saturated vapor pressure until it disappears entirely at and above 148 K. In the paper, the authors discuss the possibility that the structural transition is still occurring even at pressures at which the isotherms do not show the G.O. related substep. The isosteric heat of adsorption was also measured as a function of sorbent loading. The isosteric heat displayed a clear peak in the data in the region of the G.O. substep. Based on that heat of adsorption data, arguments were presented to suggest that an upper bound for the heat of the gate opening transition is roughly 36 meV. The kinetics of adsorption were also reported on in that study and showed that the time to reach equilibrium was unusually non-monotonic. At first, the time decreased as coverage increased. Then in the region of the G.O. substep, the wait times jumped to a higher value. Then at higher coverages, beyond the G.O. substep, the wait times decreased again. The authors attributed this unusual behavior to gate opening and subsequent filling of the additional pore volume that becomes available.

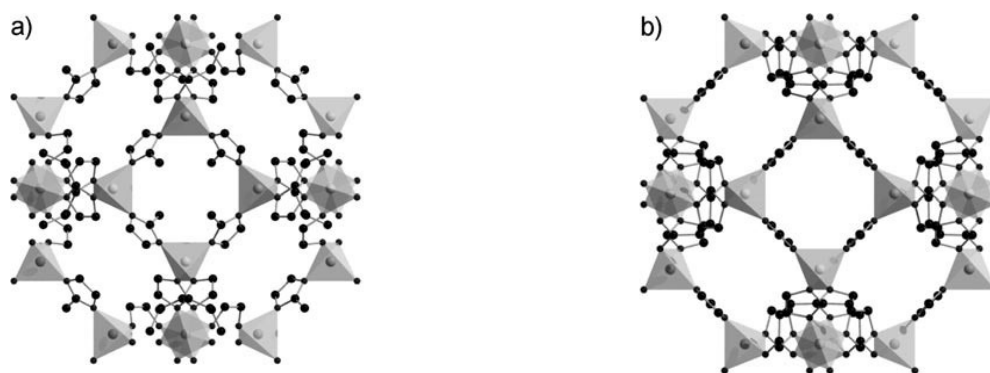


Figure 4.6: Structure of ZIF-8 reproduced from reference [69].

(a) ZIF-8 AP

(b) ZIF-8 HP with the reoriented imidazolate linkers.

Studies of other gases adsorbed on ZIF-8 found isotherms do not show substeps. One study by Fairen-Jiminez et al., [74] compares simulations with experimental isotherms for CH₄, CO₂, ethane, butane, and propane. For CH₄ and CO₂, two isotherms were measured at different temperatures: 125 and 300 K for CH₄, 196 and 273 K for CO₂. For each of the linear alkanes, only one isotherm was measured at 273 K. None of the gases in that study showed an isotherm with resolvable gate opening related substep at the temperatures measured; on the other hand, results from the simulations suggest that the gate opening effect is likely still taking place for all these gases. This is because the authors needed two different configurations of the simulated ZIF-8 structure (one for the AP structure, and one for the HP structure) in order to accurately predict the experimental isotherms. Isothermic heats of adsorption vs. coverage plots were also reported for CH₄ and CO₂. Both plots show the heat of adsorption increase linearly as coverage increases but the coverage range is somewhat limited and only goes up to 10 mmols/g for CH₄, and 8 mmols/g for CO₂.

CHAPTER 5

CO₂ ADSORPTION ON PURIFIED HIPCO SINGLE-WALL CARBON

NANOTUBES

5.1 Introduction

Research on adsorption of CO₂ is a very active field given the warming effect that CO₂ has on the atmosphere. A method for limiting the amount of CO₂ that gets into the atmosphere is to capture it from the flue gas of fossil-fuel based power plants. Strategies for doing this which involve sorption in some way include post-combustion capture, pre-combustion capture, and oxy-fuel capture technologies [1]. Various solid sorbents have been used for such carbon capture techniques including activated carbons [1] [2], zeolites [1] [2], mesoporous silica [2], and metal-organic frameworks [1] [2]. Certain criteria are useful in evaluating the suitability of sorbent materials in carbon capture technologies. These criteria are adsorption capacity, CO₂ selectivity, heat of adsorption, substrate stability under extreme conditions, adsorption/desorption kinetics, and cost [1]. Although power plants tend to operate at high pressures and temperatures, the volumetric adsorption setups in our lab are well suited to study most of these criteria at a research level.

Of fundamental relevance in the case of CO₂ adsorption is the fact that the molecule is linear and has a relatively large permanent electric quadrupole moment of 0.65 Q/e [75], where e is the electron charge. To put that value in perspective, the permanent quadrupole moments of N₂ and CO are, respectively, 0.27 and 0.34 Q/e, while those of O₂ and H₂ are somewhat less than about 0.1 Q/e [75]. The relatively large quadrupole moment of CO₂ accounts for up to 50% of the cohesive interaction between CO₂ molecules in the solid phase [76], and in an adsorption experiment it can result in

adsorbate-adsorbate interactions that are stronger than adsorbate-substrate interactions [77]. This can have drastic effects on the adsorption properties of CO₂. In fact, due to this enhanced adsorbate-adsorbate interaction, CO₂ does not wet the surface of graphite at temperatures below about 100 K [76]. This means that a film doesn't form on graphite below this temperature because the formation of bulk CO₂ is energetically favored. Additionally, the heat of adsorption on graphite at most coverages is smaller than the bulk heat of condensation/sublimation for CO₂ on graphite [76].

Two studies of CO₂ adsorption on carbon nanotubes that are relevant here exist with some contradictory results. In one study the isosteric heat of adsorption was reported to be about 234 meV for adsorption in the groove phase [57], while in the other the isosteric heat was reported to be about 24 meV [78]. The most reasonable explanation for the discrepancy is that a factor of ten was simply left out of one of the calculations by Cinke, et al. since a value of 24 meV is much too low for adsorption (24 meV is smaller than the heat of adsorption for neon on the same substrate). In any case, the rather large discrepancy is additional motivation for further study.

5.2 Experimental Details

The substrate used in this experiment was 0.1106 grams of purified HiPco SWCNTs. HiPco stands for high pressure carbon monoxide and refers to a chemical vapor deposition process which is used to produce SWCNTs [79]. Though the SWCNTs were subject to purification, they were not heated sufficiently to remove any functional groups. Consequently, the internal regions of the individual nanotubes are not accessible for adsorption. The substrate was only *mildly* heated under vacuum to remove any adsorbed particles prior to starting the experiment. Additionally, the nanotubes were expected to be mostly homogeneous, and so the interstitial channels should not be available for adsorption, with the exception of potential defects.

The experimental apparatus and procedure described in chapter 3 was used for all adsorption studies in this dissertation

5.3 Isotherms

Semi-logarithmic and linear isotherms for CO₂ adsorbed on purified HiPco nanotubes are presented in figures 5.1 and 5.2, respectively. Specific amounts adsorbed are shown in units of mmols/g. Six isotherms were measured in a temperature range approximately between 146 and 207 K. Two of those isotherms, at approximately 146 and 158 K, were measured at pressures high enough to include the saturated vapor pressure and they were used for temperature calibration in the manner described in chapter 3. The bulk triple point temperature of carbon dioxide is 216.58 K [80], which is higher than the temperatures of all the isotherms reported here. Consequently, the near vertical steps at the highest coverages for the 146 and 158 K isotherms correspond to the formation of solid CO₂ in coexistence with the vapor.

As was discussed in section 4.1, for many common adsorbates, a semi-logarithmic isotherm plot on carbon nanotube sorbents will show at least two easily resolvable substeps (at coverages below that corresponding to saturation of the bulk phase), corresponding to adsorption on the grooves and on the convex surfaces of the outer nanotubes in the bundles, respectively. Notable in figure 5.1 is the absence of any such substeps. The isotherms are smoothly convex to the logarithmic pressure axis for all coverages below that which corresponds to saturation. It can be said that the isotherms are smeared out relative to a situation where substeps might otherwise be expected. It is likely that this smearing is due to the strong adsorbate-adsorbate interaction via the quadrupole moment of CO₂; CO₂ molecules in the vapor and film interact more strongly with one another than they do with the surface of the nanotubes. The isotherms substeps that would correspond to the effect of having two groups of

different binding energy sites (namely, the grooves and outer convex regions) are smeared due to the strong interaction between the quadrupole moments.

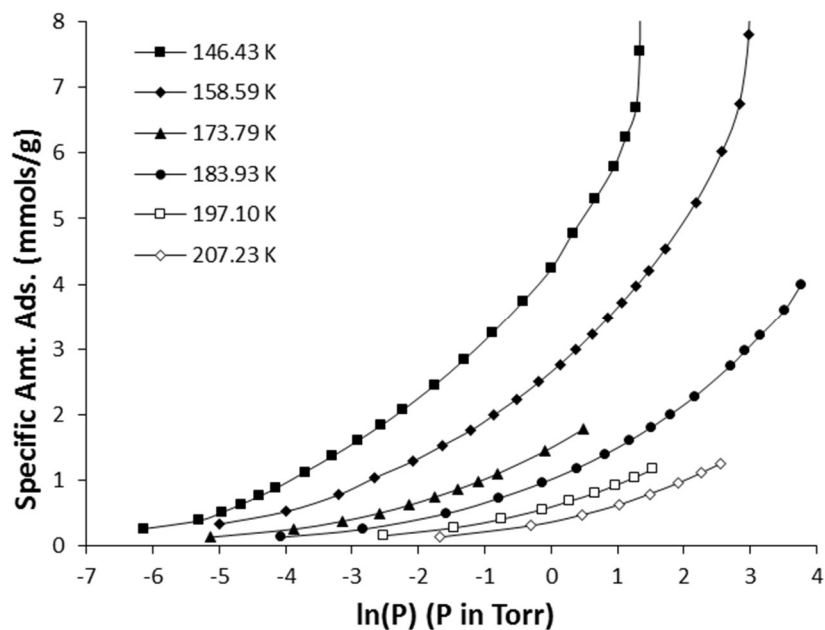


Figure 5.1: Semi-logarithmic isotherms of CO₂ adsorbed on purified HiPco SWCNT bundles.

Other adsorbates have shown degrees of smearing in semi-logarithmic isotherms when adsorbed on purified HiPco SWCNTs, namely certain linear alkanes of sufficient carbon chain length [58]. As shown in that same paper, as the chain length of the alkane adsorbate increases, the higher-coverage/lower-binding-energy substep corresponding to adsorption on the outer nanotube convex exterior regions, gradually becomes smeared out by degrees. This step is very pronounced for methane, somewhat pronounced for ethane and propane, and disappears entirely for butane. The lower-coverage/higher-binding-energy substep, however, is present and easily identifiable in all cases regardless of chain length. The smearing described in that paper was attributed to the size-entropy effect, which refers to an increasing contribution of the entropy dependent term to changes in the free energy (see section 2.2) due to the linearity and increased degrees of freedom of the alkane adsorbates

larger than methane. Essentially, even over a group of adsorption sites of similar binding energy the changing entropy term ($-T\Delta S$) causes the free energy to change enough from one point to the next on an isotherm that the chemical potential (which is proportional to $\ln P$) changes too much to show a near vertical substep. The smearing effect doesn't occur for substeps corresponding to the higher binding energy sites because in that case the U term of the free energy dominates and entropy effects aren't as noticeable. This smearing also becomes more prominent at higher temperatures [58] since the entropy is multiplied by temperature in the expression for free energy.

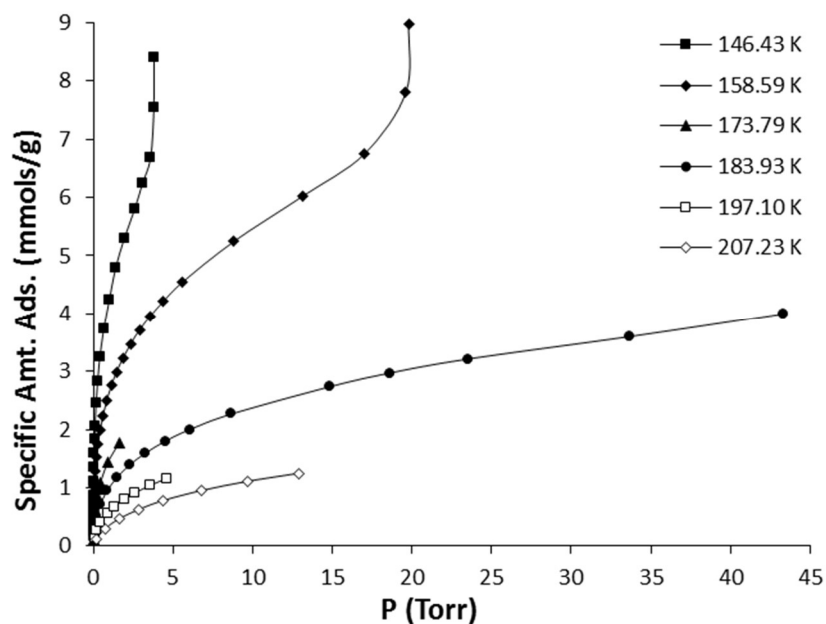


Figure 5.2: Linear isotherms of CO₂ adsorbed on purified HiPco SWCNT bundles. Isotherms are of Type II with a broad knee.

It seems that the effects of attractive adsorbate-adsorbate interactions for the CO₂ – SWCNT system produces smearing even more pronounced than the smearing described in the previous paragraph for the linear alkanes. In the alkane paper, the isotherms compared were all at a reduced

temperature of roughly 0.5. The reduced temperature is defined in this case as the ratio of the temperature of the isotherm to the critical temperature of the adsorbate. The critical temperature of CO₂ is 304 K [80], which makes the isotherm at 146 K at a reduced temperature of 0.48. This isotherm at 146 K in figure 5.1 shows no substeps, even for the higher binding energy groove phase. Technically, CO₂ is also a linear molecule and therefore it might be appropriate to propose that some of the smearing might come from the size-entropy effect or adsorbate reorientation. Since CO₂ is smaller than all of the linear alkanes, however, the effects of linearity are probably less important than the effects of permanent polarity.

The linear isotherms of figure 5.2 can perhaps be classified as Type II, with a very broad knee. Application of the BET method (even though nanotube bundles aren't homogeneous) to the isotherm at 158 K reveals a c value of approximately 54.

5.4 Effective Specific Surface Area

The Point-B, and BET, methods were both used to determine the effective specific monolayer capacity in a manner previously described. It should be noted that both methods suffer from inherent ambiguity. It can be seen from the data in figure 5.2 that the linear isotherms contain only very broad knees in the region following the Henry's law regime, making identification of the precise location of the point B problematic. In the case of the BET method, SWCNTs are energetically heterogeneous which makes application of that method a bit uncertain as well. In any case, figure 5.3 shows the identification of point B (a) and a BET linear plot (b), both for the CO₂ isotherm at 158 K. The Point B method yields an effective specific monolayer capacity of about 3.71 mmols/g. The value of the area per CO₂ molecule adsorbed is 15.7 Å² which comes from experiments on graphite [76]. It is assumed that the area per molecule adsorbed is the same in this case. The calculated effective specific surface area for the Point-B

methods yields a value of about 351 m²/g. The BET linear plot yields a value for effective specific monolayer capacity of about 3.46 mmols/g, which gives an effective specific surface area of 327 m²/g.

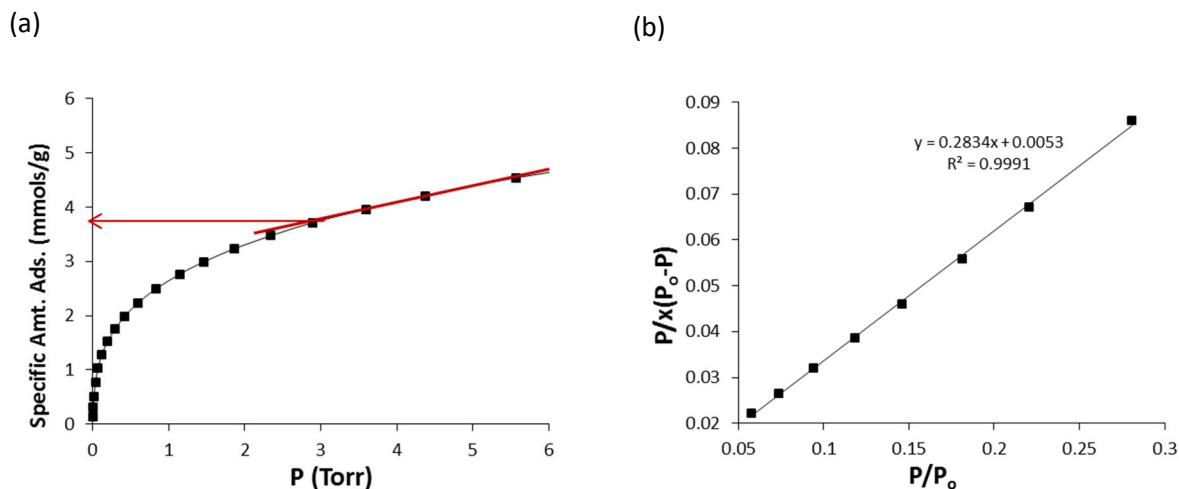


Figure 5.3: Effective monolayer capacity using data from the isotherm at 158 K ($T/T_c = 0.52$).

- (a) Point B Method (3.71 mmols/g, 351 m²/g)
- (b) BET linear plot (3.46 mmols/g, 327 m²/g, $c = 55$)

As stated in section 4.1, ESSA measurements for many adsorbates at similar reduced temperatures on close ended SWCNTs yield values that are very similar indicating that they have access to the same adsorption sites. On other samples of purified HiPco nanotubes, xenon and hydrogen [52], and ethane [81] yield ESSA values of 608, 594, and 643 m²/g, respectively. These values compare well with each other but are roughly twice the value measured here for CO₂ of 351 m²/g. It's plausible that the discrepancy is at least partly due to the inherent ambiguity of the location of point B and/or differences in the relative temperature of the isotherms from which the effective monolayers were determined. However, in even the most ambitiously liberal use of the point B method, the highest value of effective monolayer capacity in the 158 K isotherm is roughly 5 mmols/g which would lead to an ESSA of only 473 m²/g. That value is still much lower than the ESSA determined from xenon, hydrogen, and

ethane adsorption isotherms. It's likely that neither the Point-B, nor the BET, methods are suitable for determining effective monolayer capacities for isotherms in which adsorbate-adsorbate interactions are large, which is the case for CO₂ adsorption on SWCNTs.

5.5 Isosteric Heat of Adsorption

Isosteric heat vs. coverage and $\ln P$ vs $1/T$ plots are shown in figures 5.4 and 5.5, respectively. The overall shape of the isosteric heat vs. coverage plot is unusual. As discussed in section 4.1, the isosteric heat for most adsorbates on nanotube bundles typically decrease from a maximum at the lowest coverage to the minimum at the highest coverage (latent heat) with features in between corresponding to the adsorption sites for some adsorbates. Figure 5.4 shows that this obviously isn't the case here. At all but the lowest coverage of 0.2 mmols/g, the isosteric heat for CO₂ on SWCNTs is *lower* than the latent heat of deposition. This behavior is attributable to the quadrupole interaction between CO₂ molecules, which reduces the measured heat of adsorption at most coverages. As coverage increases, adsorbate-adsorbate interactions become more important and the measured isosteric heat of adsorption rises until bulk CO₂ is formed.

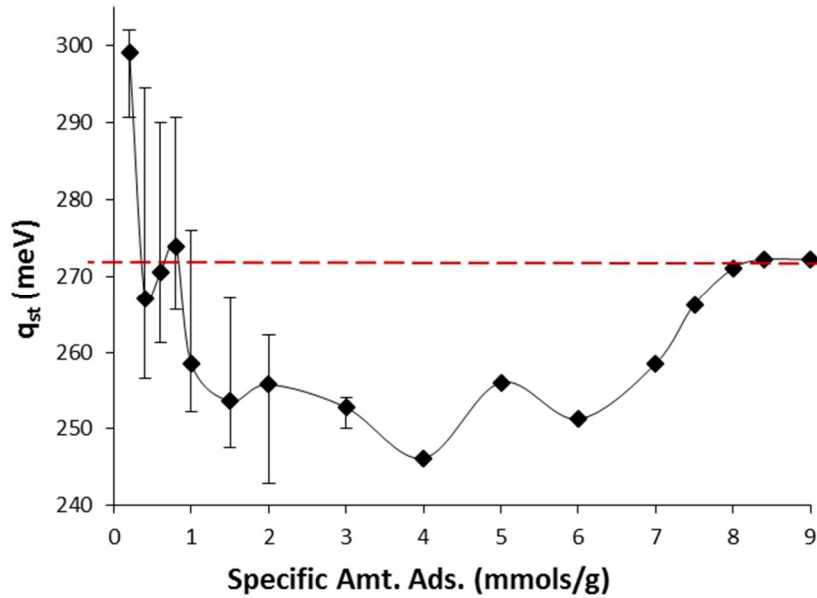


Figure 5.4: Isosteric Heat (q_{st}) as a function of coverage. The red dashed line indicates bulk latent heat.

The results here are qualitatively similar to those found by Bienfait, et. al, [57] for CO_2 adsorption in that the isosteric heat of adsorption is lower at most coverages than the latent heat for bulk CO_2 . In that paper it was speculated that a plateau in the isosteric heat data corresponded to adsorption in the grooves and some interstitial channels but the data was inconclusive. Terlain and Larher [76] found a heat of adsorption value for CO_2 adsorbed on graphite of about 260 meV (6 kcal/mole). That value is slightly above (or comparable to) the minimum in figure 5.4 from about 1.5 to 6 mmols/g of about 245 to 255 meV. For adsorption on the convex outer surfaces of the nanotubes in the bundles, one would expect the heat of adsorption to be slightly lower than for that on planar graphite. This might suggest that the broad minimum in figure 5.4 corresponds to adsorption on the outer convex surface sites of the nanotubes.

The highest value of approximately 283 meV at 0.2 mmols/g could be due to defects or irregularities in individual nanotube diameters which can cause a certain number of interstitial channels to become available for adsorption.

Attention should be drawn to the significant error bars, particularly in the lower coverage range. Deviations of the data points from the linear line of best fit can be seen in figure 5.5. No error bars were calculated for coverages at and above 4 mmols/g because, as can be seen in the $\ln P$ vs $1/T$ chart, only two isotherms were measured at those coverages. Even so, the general “u” shape of the isosteric heat vs. coverage plot remains intact if the error bars are considered. Additionally, the highest coverage limit of the isosteric heat of 272 meV corresponds well with the bulk heat of deposition for CO_2 of 272 meV [80].

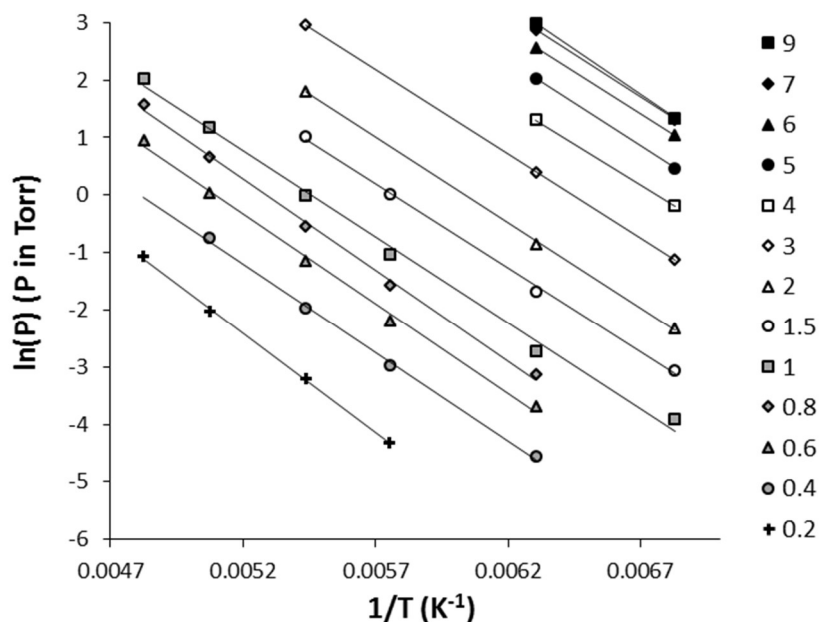


Figure 5.5: Natural logarithm of equilibrium pressure vs the inverse of temperature. Each line is at a constant coverage, shown on the right in units of mmols/g.

5.6 Kinetics of Adsorption

Figures 5.6 and 5.7 show the kinetic results for this system. The data in figure 5.6 come from the isotherm at 146 K. Figure 5.6a shows linear driving force model curves corresponding to points in the isotherm at selected coverages (the individual curves have been truncated for clarity). Figure 5.6b shows fractional pressure change curves (see section 3.8) for some of the points. The red line in figure 5.6a at a $\ln(1-\theta)$ value of approximately -4.61 indicates the value at which each curve reaches 0.99 fractional uptake, θ . From the data, it can be seen that the time to reach this value of $\ln(1-\theta)$ decreases as the point number, and thus the isotherm coverage, increases. However, at even lower values of $\ln(1-\theta)$, the slope is lower for the higher coverage points and the final approach to equilibrium lengthens dramatically in time. This happens in particular for points 18, 21, and 24 around a $\ln(1-\theta)$ value of roughly -5.5, which corresponds to a fractional uptake of 0.996. The fractional pressure change and time to reach equilibrium (red arrows) are displayed in figure 5.6b, where it can be seen that the time increases for the higher coverage points. The exact placement of the arrows which indicate equilibrium is somewhat up to interpretation given the amount of noise that comes into play for pressure measurements with such long relaxation times. Even considering the noise, it's clear that the wait time for the attainment of equilibrium is significantly longer at the higher coverages. The vertical axis is displayed with arbitrary units and the individual FPC plots have been displaced up or down for clarity.

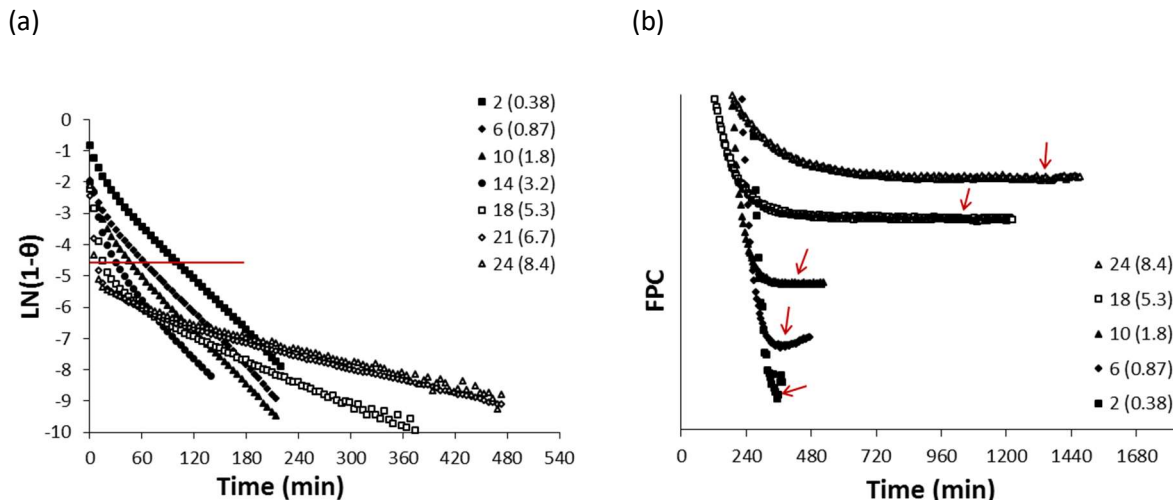


Figure 5.6: Kinetics of adsorption data for select points along 146 K isotherm. The point numbers are given in the legend, with coverage in parentheses in units of mmols/g.

- (a) Linear Driving Force model. The red line corresponds to $\theta=0.99$
- (b) Fractional Pressure Change in arbitrary units with plots displaced for clarity. The red arrows correspond to equilibrium.

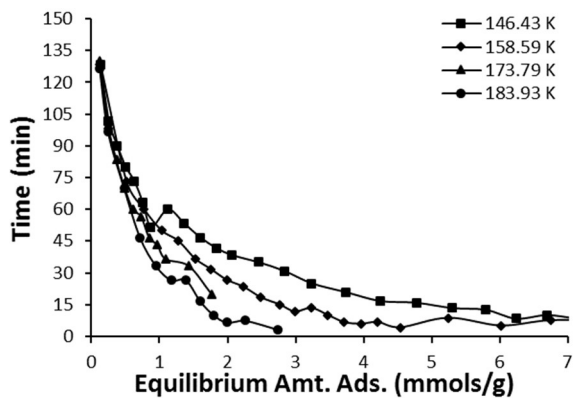
Figures 5.7a and 5.7b show a summary of kinetic results for four of the isotherms, all of which come from analyzing data such as that in figures 5.6 for each individual isotherm. All the isotherms show similar trends. The time to reach a fractional uptake of 0.99 for each point decreases as coverage increases and decreases as temperature increases at constant coverage, as shown in figure 5.7a. Figure 5.7b shows that the time to reach equilibrium starts at about 360 min (6 h) and stays relatively constant at low coverages, before increasing as coverage increases. Additionally, the higher the temperature of the isotherm, the lower the coverage at which the time increases sharply. Note that there is significant noise in the higher coverage equilibrium times, and the plots have been truncated for clarity. Even considering the noise, however, the time to reach equilibrium never drops as low as the times at the lowest coverages, for all the isotherms displayed here.

The kinetic trends in figure 5.7a for $\theta=0.99$ are the same as for the *equilibrium* adsorption kinetics for many spherical, or nearly spherical, adsorbates on close ended SWCNTs (as discussed in

section 4.1). It seems possible that up until the coverage (at each point along the isotherms) reaches a fractional uptake of 0.99, the kinetics are largely dictated by the vapor pressure in the ways that are analogous to the case for equilibrium kinetics for spherical adsorbates on homogeneous substrates; higher coverage means higher vapor pressure which results in more adsorbate-substrate collisions and faster kinetics and, similarly, higher temperature also means higher pressure and more collisions.

However, the equilibrium kinetic trends of figure 5.7b are different and the reasons for this are unclear. While it's true that the equilibrium trends of the linear alkanes larger than ethane adsorbed on close ended SWCNTs (see section 4.1) follow a similar trend to that of figure 5.7b, linearity can't be used to explain the kinetic behavior of CO₂ since it is a relatively small molecule (certainly smaller than ethane). Ethane on SWCNTs, follows the usual kinetic trends for spherical adsorbates on homogeneous substrates. It seems more plausible that the equilibrium kinetic behavior of CO₂, then, is the result of its adsorbate-adsorbate quadrupole interaction which becomes more and more important as coverage increases. This is seen by the sudden increase in wait times in figure 5.7b after a certain isotherm coverage is reached. At that coverage and beyond, the rate of uptake slows after a certain fractional uptake as is seen in figure 5.6a somewhat after the LDF plots drop below the red line.

(a)



(b)

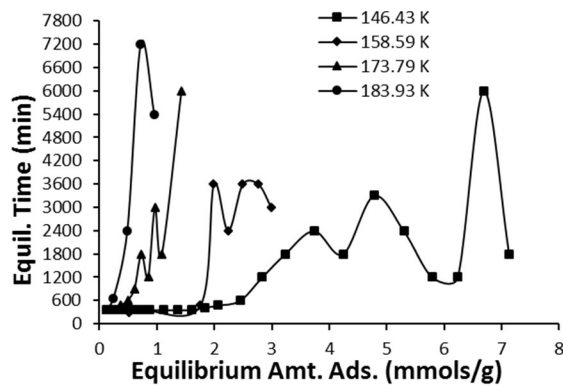


Figure 5.7: Summary of adsorption kinetics data for four isotherms. Wait time vs. equilibrium coverage.

(a) Time to reach $\theta = 0.99$.

(b) Time to reach equilibrium.

CHAPTER 6

ETHANE ADSORPTION ON AS-PRODUCED DAHLIA-LIKE CARBON NANOHORN AGGREGATES

6.1 Introduction

Ethane (C_2H_6) is the smallest of the saturated linear hydrocarbons, and its adsorption is an important process to explore for industrial reasons. Since ethane is a component of natural gas, it often needs to be separated from CH_4 , and CO_2 [6]. Ethene is also an important molecule in industry and can be obtained through the steam cracking of ethane; this is a process that results in an ethane/ethene mixture and the components need to be separated to obtain pure ethene [6]. Distillation is the current widely used method for ethane/ethene separation but it is a very energy intensive process which motivates the exploration of sorption processes to take its place [6].

The adsorption of many linear hydrocarbons, including ethane, has been studied using graphite [82] and SWCNTs [81] as substrates. Given that ethane is the smallest linear alkane, it can serve as a simple model for the adsorption of linear molecules in general. Conducting sorption measurements of ethane on aggregates of nanohorns allows us to explore experimentally the question of how linear molecules adsorb in conical pores.

6.2 Experimental Details

The dahlia-like nanohorn aggregates used in this experiment were not subject to chemical treatment. Because of this, the walls of the nanohorns were intact and the interiors of the nanohorns are not available for adsorption. The aggregates were heated mildly to 520 K under vacuum for 24 h in

order to clean the substrate. The mass of the sample was 0.0449 g. The gas used was research purity ethane (99.98%) purchased from Matheson.

6.3 Isotherms

Nine isotherms of ethane adsorbed on as-produced nanohorn aggregates (henceforth, abbreviated as 'Ethane-NH') are shown in figures 6.1 and 6.2, for temperatures ranging from 123 to 221 K. The triple and critical point temperatures for ethane are 91, and 305 K, respectively [83]. Consequently, the highest coverage vertical step above about 6 mmols/g for the isotherm at 164 K corresponds to the formation of bulk liquid ethane, and the measurement of saturated vapor pressure. The saturated vapor pressure was also obtained for the isotherm at 123 K for the purposes of temperature calibration, but the data point isn't shown here.

In figure 6.1, the semi-logarithmic isotherms for Ethane-NH are mostly smeared out. However, a gentle substep can be discerned in the isotherms at 123 K, 134 K, 144 K, and 164 K, in the coverage range of about 2 to 3 mmols/g. This substep corresponds to weaker binding energy sites located around the outer regions of the individual nanohorns, away from the conical interstitial sites. The isotherm at 175 K no longer shows this substep. The isotherms at 155, 205, and 221 K were not measured at sufficiently high coverages to include the region where the weaker binding energy substep would show. The isotherm at 190 K includes too few data points in that region to be clear either way. It appears that the weaker binding energy substep is smoothed entirely out at higher temperatures.

Also notably absent from the isotherms of figure 6.1 are any substeps that would correspond to the higher binding energy sites in the conical interstitial regions of the nanohorn aggregates, even for the higher temperature isotherms at low coverage.

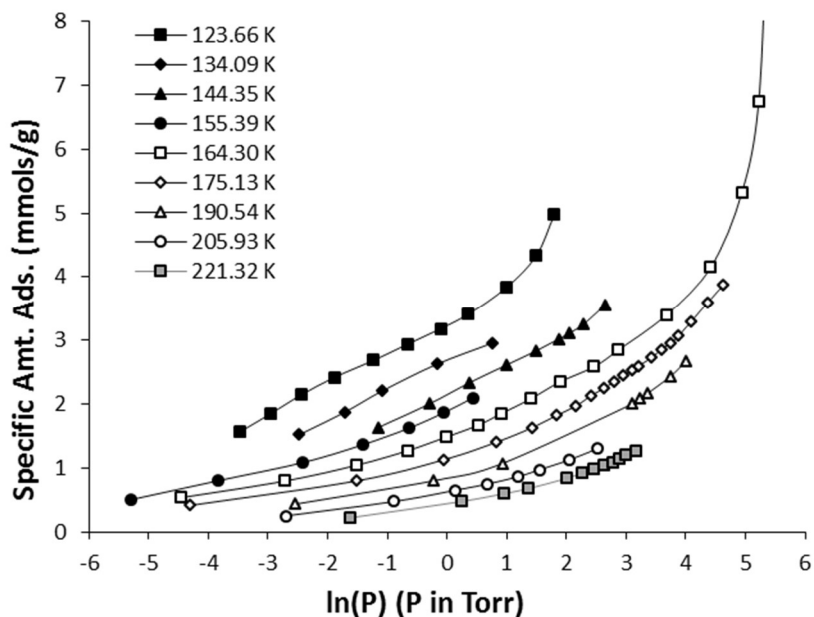


Figure 6.1: Semi-logarithmic isotherms of ethane adsorbed on as-produced dahlia-like carbon nanohorn aggregates.

In short, the weaker binding energy substep is present for the lower temperatures only, while the higher binding energy substep is absent entirely (*at least* in the temperature range from 155 to 221 K, and for the range of pressures we have studied).

The absence of the higher binding energy substep for isotherms of Ethane-NH is likely an indication that the morphology of dahlia-like nanohorn aggregates is such that the spread in adsorption site binding energies is too large. As the ethane molecules move farther inward into the depths of the conical pores, they see a continuously changing binding energy. This continuously changing binding energy leads to the smeared out isotherms. This is despite the fact that isotherms for both Ne, and CF_4 adsorbed on closed nanohorns [65] both show a high binding energy substep corresponding to adsorption in the conical interstitial pores. The reason that the ethane isotherms are more smeared out compared to Ne and CF_4 is that ethane is a linear molecule which provides an additional degree of freedom which leads to a larger spread in energy when compared to Ne, and CF_4 which are both

spherical (or effectively spherical). The adsorbed ethane molecules can rearrange themselves as a result of adsorbate-adsorbate interactions as more film is sorbed in the nanohorns.

The higher coverage substep for Ethane-NH corresponds to the outer cylindrical regions of the individual nanohorns where the binding energy is more constant. This more constant binding energy leads to the appearance of gentle substeps at the lower temperatures which are smeared as the temperature increases. This view is consistent with computer simulations which have been done for this system [84].

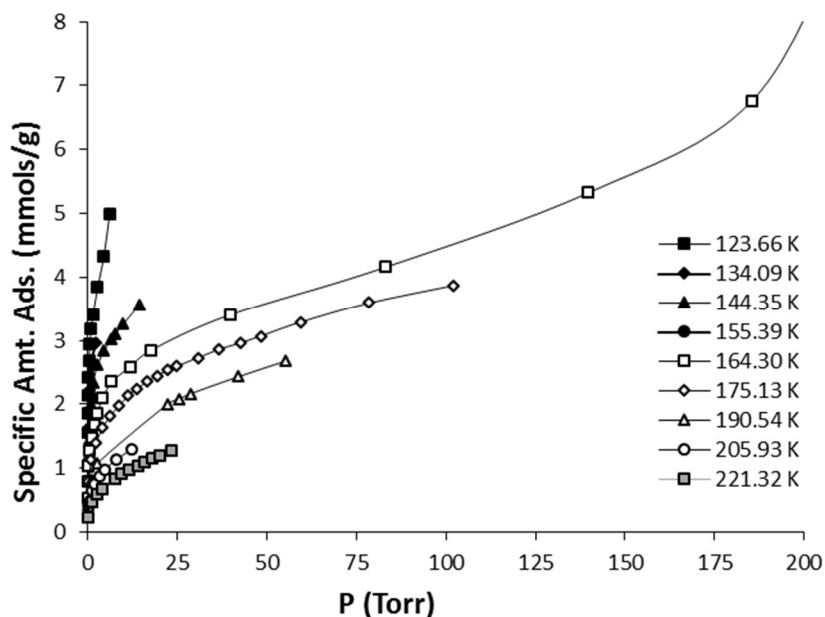


Figure 6.2: Linear isotherms for ethane adsorbed on as-produced dahlia-like carbon nanohorn aggregates.

6.4 Effective Specific Surface Area

Figure 6.3 shows the Point-B and BET linear plot methods for determining the effective monolayer capacity of Ethane-NH. The isotherm temperature selected was 164 K which corresponds to a relative temperature of $T/T_c = 0.54$. The value of effective monolayer capacity of 3 mmols/g using the Point-B method compares favorably to the value of 2.9 obtained from the BET linear plot. The area per

adsorbed ethane molecule is taken to be 21 \AA^2 which comes from experiments on graphite [85] where the adsorbed ethane molecules were lying flat with their long axes parallel to the surface. Using the value of 3 mmols/g from the Point-B method gives an effective specific surface area of $380 \text{ m}^2/\text{g}$. As discussed in section 4.2, the ESSA values for Ne, CO_2 , and CF_4 on closed nanohorns are 393, 358, and $288 \text{ m}^2/\text{g}$, respectively. The value for ethane falls between that of Ne, and CO_2 . Though the diameter of CF_4 is larger than the width of ethane, the area per ethane molecule adsorbed is larger than CF_4 , and it might be assumed that ethane would give a value of the ESSA that is smaller. A possible explanation is that a portion of the adsorbed particles are in the deep conical pores forming a volume of adsorbate in addition to a 2D film on the surfaces. Another possible explanation for the fact that ethane's ESSA is larger than CF_4 is due to differences in relative temperature or the fact that neither the Point-B nor BET linear plot methods are suitable for determining the effective monolayer capacity of linear molecules on dahlia-like carbon nanohorns.

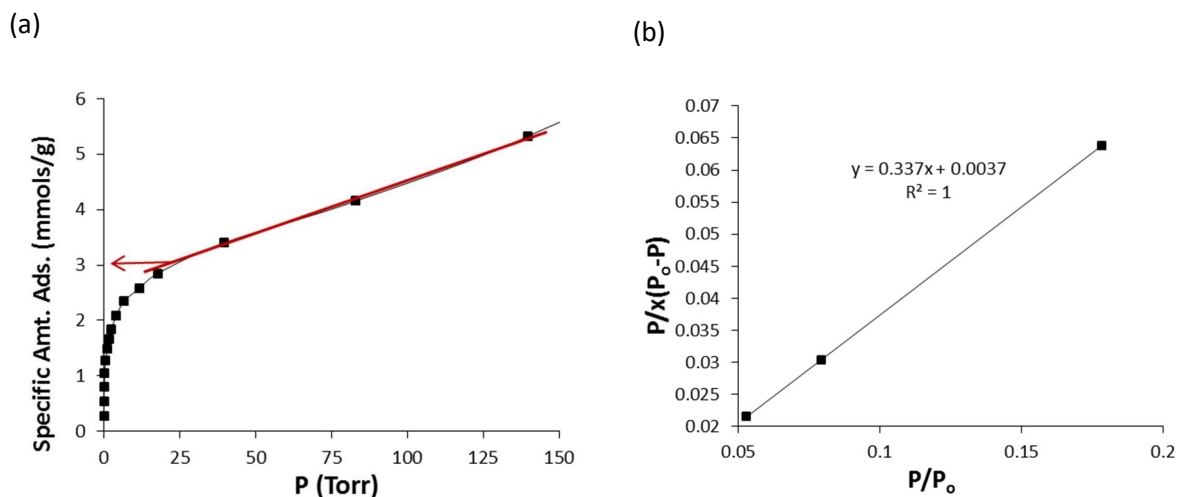


Figure 6.3: Determination of effective monolayer capacity using data from the isotherm at 164 K ($T/T_c = 0.54$)

- (a) Point-B Method (3 mmols/g, $380 \text{ m}^2/\text{g}$)
- (b) BET Method (2.9 mmols/g, $367 \text{ m}^2/\text{g}$, $c = 93$)

6.5 Isotheric Heat of Adsorption

Figures 6.5 and 6.6 show the isotheric heat as a function of coverage and $\ln(p)$ vs $1/T$ plots, respectively. The isotheric heat decreases monotonically as coverage increases. This behavior is typical of strongly binding adsorbates. Higher coverages were not included in the isotheric heat plot because only two isotherms were measured at coverages higher than about 3.3 mmols/g which causes the uncertainty to increase. The initial, steeply decreasing region below about 0.5 mmols/g corresponds to the highest binding energy sites for the isotherm coverages measured here. These high values likely result from adsorption in the deepest porous regions between the individual nanohorns.

A gently sloping plateau region can be identified at coverages from about 0.5 mmols/g to slightly less than 1.5 mmols/g. Comparison to figure 6.1 reveals that this plateau region includes coverages below the low binding energy substep; the isotherms show no discernible substeps in the regions corresponding to this plateau. It can be seen that the isotheric heat in this region decreases from a value of 264 meV down to a value of 218 meV. This high energy plateau is a result of adsorption in the conical interstitials near the bases of the individual nanohorns and the isotheric heat is sloping because the binding energy is changing as the conical regions widen out. Additionally, the linear ethane molecules have more degrees of freedom than a spherical adsorbate which introduces a further spread of energy. This can be seen by comparison to the isotheric heat of Ne and CF₄ when adsorbed on closed nanohorns; both show a very flat plateau corresponding to the lower binding energy site. Ethane adsorbed on bundles of closed ended carbon nanotube bundles shows a high energy isotheric heat plateau corresponding to adsorption in the 1-D groove phase at an energy of about 270 meV [58]. The isotheric heat of the interstitial conical region of nanohorn aggregates at 0.5 mmols/g seems to be roughly equivalent to the groove phase of nanotubes, for the case of ethane adsorption.

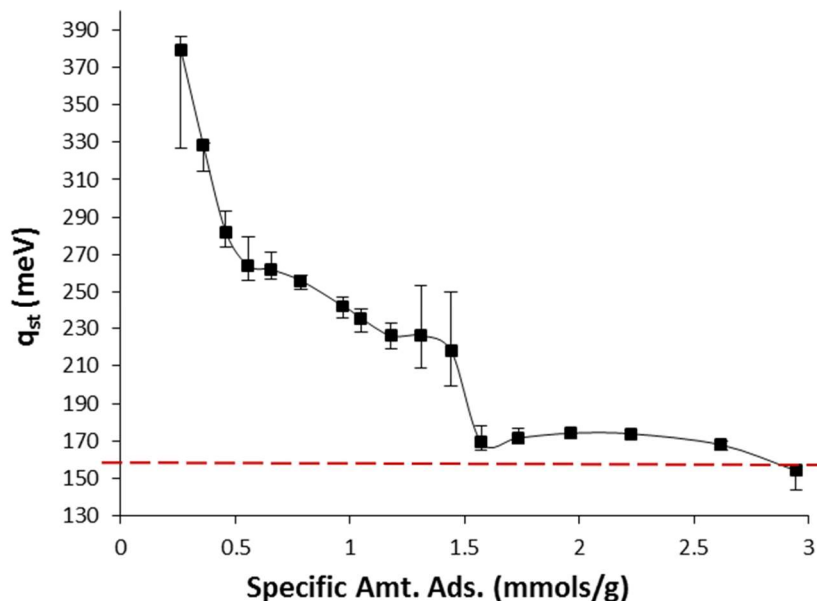


Figure 6.4: Isosteric Heat (q_{st}) as a function of coverage. The red dashed line indicates bulk heat of condensation for ethane.

The lowest energy plateau from 1.5 to 2.5 mmols/g corresponds to adsorption on the outer regions of the individual nanohorns, away from the conical interstitials. This plateau is much flatter than the higher energy plateau. The energy of this plateau is near 170 to 175 meV. After this plateau, the isosteric heat gradually decreases toward the value corresponding to bulk condensation. The values of the heat of condensation from [83] for ethane at the most similar temperature range to the current set of isotherms is reported as 159 meV (15.3 KJ/mole). The highest coverage value reported here is within 3% of that reported value, although higher coverages would probably be needed to be more certain of having an actual isosteric heat value corresponding to bulk saturation.

A line extrapolated from the three lowest coverage isosteric heat values in figure 6.4, to zero coverage can give us an estimate of the single particle binding energy for Ethane-NH. This is done via equation 2.7 where the value taken for γ is 2 [66], and T is the average temperature of the isotherms used in the isosteric heat calculations (in this case $T = 168.3$ K). The zero coverage limit is about 510

meV, and application of equation 2.7 yields a value for the binding energy of 481 meV. However, as can be seen in figure 6.4, the error bar at the lowest coverage is quite significant; it spans a range of approximately 60 meV. The reason for these large error bars can be seen in figure 6.5; only three isotherms were measured at that lowest coverage (0.26 mmols/g) and removing any one of the points will result in a large change of slope. Additionally, there isn't a good reason to assume that a linear extrapolation will give the correct form of the isosteric heat plot for lower coverages. This makes the value of the binding energy here, at best, an approximation.

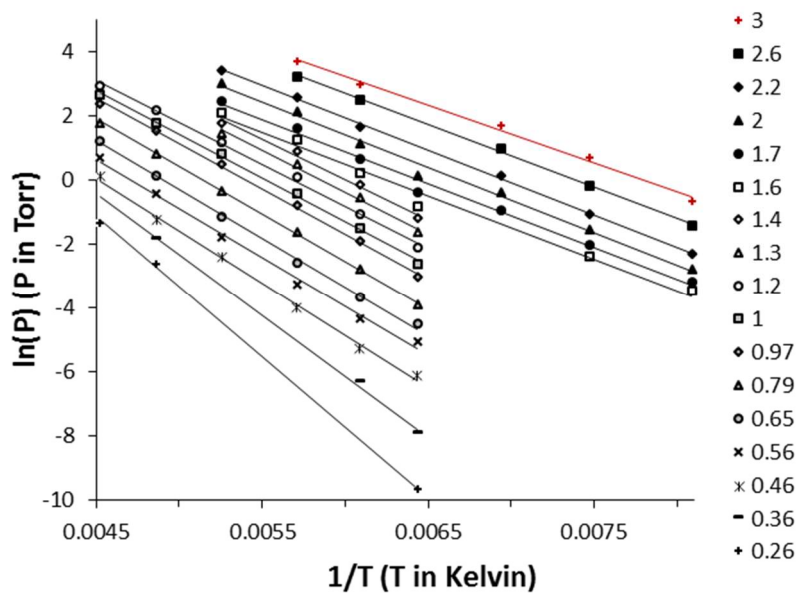


Figure 6.5: Natural logarithm of equilibrium pressure vs the inverse of temperature. Each line is at a constant coverage, shown on the right in the legend in mmols/g.

The value of the binding energy for ethane on graphite is 175 meV, which is close to the value reported here for ethane on the convex outer surfaces of the individual nanohorns. With the value calculated here, this represents an increase in the binding energy of 2.7 times for adsorption of ethane

in the deep porous regions of nanohorn aggregates relative to graphite. On nanotube bundles, the binding energy for ethane in the grooves was reported to be 1.76 times larger than ethane on graphite [81].

6.6 Kinetics of Adsorption

Figure 6.6a shows linear driving force plots (LDF) and figure 6.6b shows the fractional pressure change (FPC) for selected points along the isotherm at 164 K. The isotherm point numbers are indicated in the legend with the coverage in mmols/g in parentheses. In figure 6.6a the rate of adsorption is shown to slow down as the coverage increases, since the slope gradually lowers (after the initial sharp decrease). Figure 6.6b shows the wait time to equilibrium increasing dramatically as coverage increases. The wait time for point 3 at 1.04 mmols/g is about 8 h (see inset) while the wait time for point 8 at 2.09 mmols/g is about 200 h.

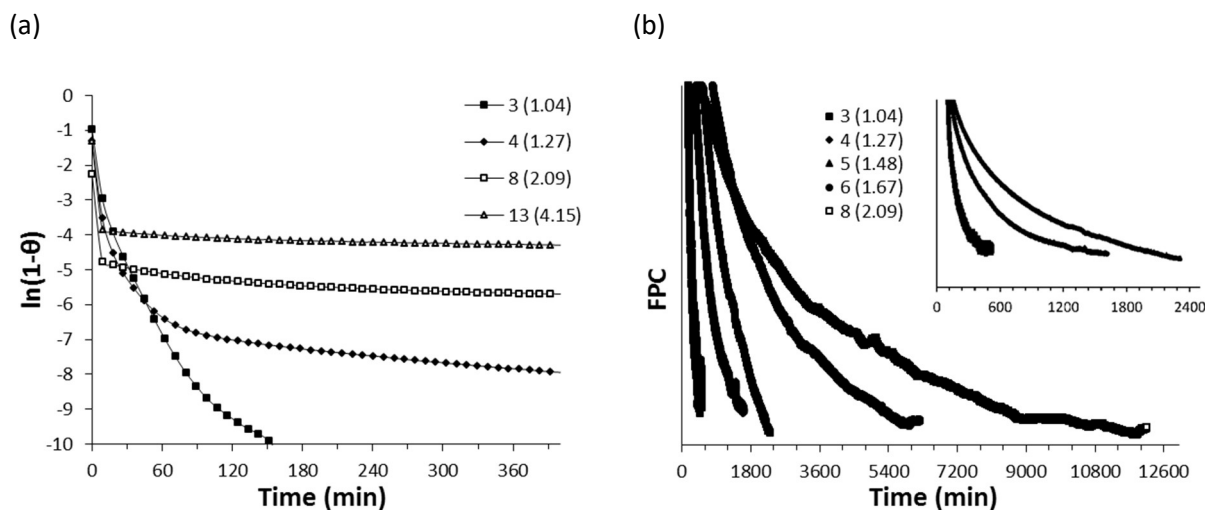


Figure 6.6: Kinetics plots for select points along the 164 K isotherm. Point numbers are indicated in the respective legends with the corresponding coverage in parentheses in mmols/g.

- (a) Linear driving force model for a few coverages. Only select points within each plot are shown.
 (b) Fractional pressure change in arbitrary units. Coverages increases from left to right. Points 3, 4, and 5 are shown in more detail in the inset.

Kinetic results are summarized in figure 6.7 for four of the isotherms from figure 6.1. In figure 6.7a, the time to reach a fractional coverage of 0.995 is displayed while in figure 6.7b, the time to reach equilibrium is displayed. The overall trend in both cases is similar; as coverage within an individual isotherm increases, so too does the wait time. This is apparent in figure 6.7b for equilibrium. In figure 6.7a, the isotherm at 155 K is almost constant throughout all coverages while for the other three isotherms, the first couple of points seem to *decrease* in wait time with increasing coverage. In those isotherms where the time to reach $\theta = 0.995$ decreases at first, it might be because the wait times in that regime are controlled by the increasing pressure.

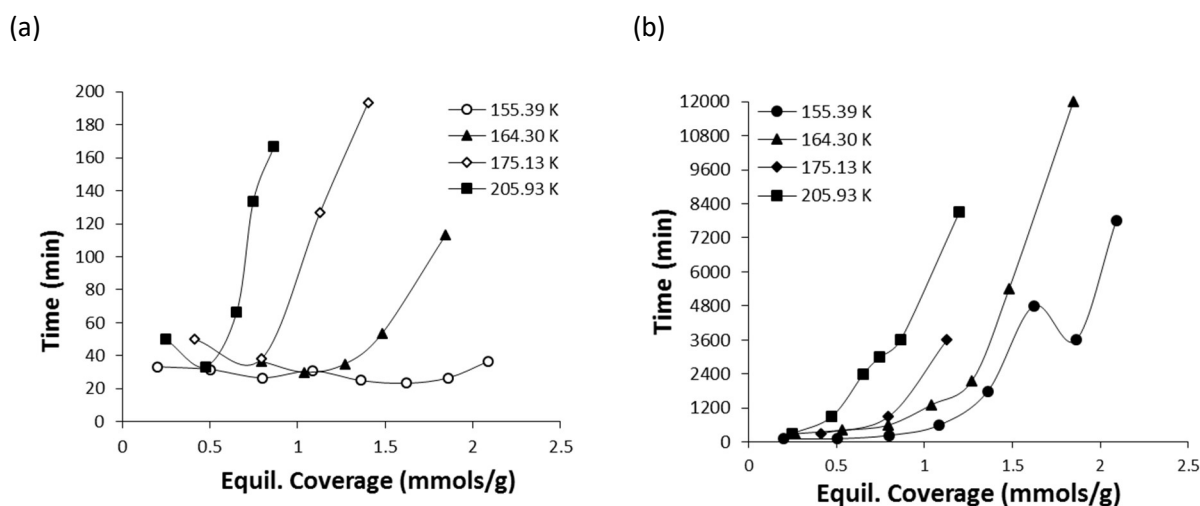


Figure 6.7: Kinetics for points along select isotherms as functions of equilibrium coverage.
 (a) Time to reach $\theta = 0.995$
 (b) Time to reach $\theta = 1$ (equilibrium). Due to increasing instrumental noise at higher coverages, plots have been truncated for clarity. Roughly up to the first effective monolayer is represented.

The kinetic behavior of the ethane-NH system differs from that of the ethane-SWCNT in at least three different ways: the overall magnitude of the wait times, the dependence of wait times on equilibrium coverage within an isotherm, and the dependence of wait times on temperature at

sufficiently high coverages. The wait times for ethane-NH are dramatically longer than for ethane-SWCNT. For ethane-SWCNT, the longest wait times for an isotherm measured at 160 K [60] at low the lowest coverage was about 400 min (6.7 h), which then decreased as coverage increased. Compare that to figure 6.6b for ethane-NH at 164 K where the wait time are longer at all coverages. The ethane-SWCNT equilibrium kinetics are similar to those of spherical adsorbates on planar substrates which were discussed in section 2.5. The trends of figure 6.7b are different for ethane-NH; they increase as coverage increases at constant temperature, and they also increase at constant coverage for increasing temperature (above a certain threshold coverage).

The likely reason for these differences comes down to the morphology of the nanohorn aggregates. The pores are conical, and there is a point at which the diameter of the pore is similar to the effective diameter of the ethane molecules which provides a situation where diffusion can play an important role in determining the adsorption kinetics. It's been shown that adsorption in pores can take much longer than adsorption on surface sites (or surface sites *and* groove sites, in the case of SWCNTs) [36]. This might help explain the general shape of the plots in figure 6.7b for each isotherm.

CHAPTER 7

ARGON ADSORPTION ON CHEMICALLY OPENED DAHLIA-LIKE CARBON NANOHORN AGGREGATES

7.1 Introduction

Argon is the third smallest spherical noble gas atom, being only larger than Neon and Helium. Unlike Helium and Neon, however, Argon is massive enough so that quantum effects do not have an appreciable effect on its adsorptive properties [82]. When adsorbed on graphite, it can form monolayer phases identified as gas, liquid, and incommensurate solid (its lattice structure differs from that of the graphite substrate), depending upon the temperature [82]. Since it is spherical, argon is a good adsorbate to help determine the effects adsorbate size (when compared to other noble gas adsorbates on the same substrate) on adsorption measurements. Also, since argon is spherical and non-polar, effects of substrate morphology on adsorption measurements can be more easily studied.

7.2 Experimental Details

The mass of the nanohorn sample was 0.1692 g. The aggregates were oxidized in air for nine hours in which the temperature was increased at a rate of 1° C per minute to a maximum of 550° C. They were then cooled by simply allowing them to naturally reach room temperature. This process opened up the nanohorns to allow access to the interior. The nanohorns were given to us from the Japan Science and Technology Agency. The argon used was purchased from Matheson Tri-Gas. It has a reported research grade purity (99.9999%) [86].

7.3 Isotherms

Eight isotherms were measured for Ar adsorbed on oxidized carbon nanohorn aggregates (Ar-ONH) in the temperature range of 71 to 127 K. These isotherms are shown semi-logarithmically in figure 7.1 and linearly in figure 7.2. The five lowest temperature isotherms were measured at pressures all the way up to saturated vapor pressure and the highest coverage vertical step at about 30 mmols/g and beyond corresponds to this. The triple point and critical temperature of Ar are 84 K, and 151 K, respectively. The three lowest temperature isotherms are below the triple point, meaning they saturate as solid argon at the highest coverage step.

Below the substep corresponding to saturation, there are two clearly resolvable substeps in the semi-log plots. Given that these are chemically opened nanohorn aggregates, these two substeps correspond to the four binding energy sites (figure 4.4). The highest-energy/lowest-coverage substep from about 2 to 8 mmols/g corresponds to adsorption in the interstitial and intra-nanohorn pores. The lower-energy/higher-coverage substep from about 15 to 25 mmols/g corresponds to adsorption on the interior and exterior surfaces. The high energy substep spans a coverage range of roughly 4 mmols/g while the low energy substep spans a coverage range of roughly 10 mmols/g, indicating that there are on the order of 2.5 times as many adsorption sites along the interior and exterior surfaces than the number of adsorption sites in the interstitial and intra-nanohorn pores.

Since four different adsorption sites for the open nanohorn aggregates have been identified, it might be worth checking to see if any further features are resolvable within the two broad binding energy substeps. S. M. Gatica et. al. [87] simulated Ne, Ar, CO₂, and CH₄ adsorption in carbon nanohorns in which the interior sites are available for adsorption as well as the exterior sites. In that paper, it is shown that for neon and argon, adsorption occurs first (that is, at a lower coverage) in the intra-nanohorn pores than it does in the interstitial pores (see figures 2 and 3 for neon and in figure 5 for argon in ref. 87). For neon in particular, there is a gentle substep in the simulated isotherm which

corresponds to adsorption in the intra-nanohorn pores, before the onset of adsorption in the interstitial pores.

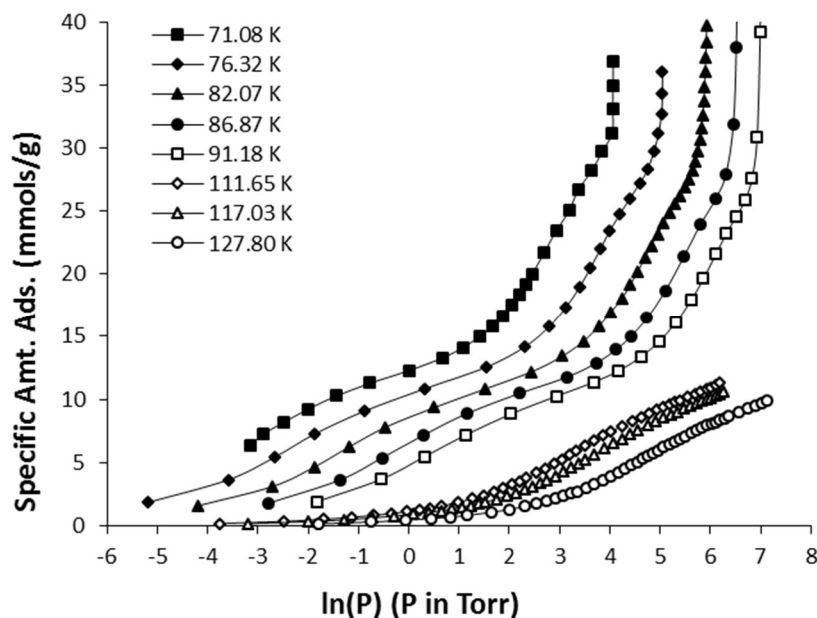


Figure 7.1: Semi-logarithmic isotherms of Ar adsorbed on opened dahlia-like SWCNH aggregates

A plot of the three highest temperature isotherms from figure 7.1 in the coverage range corresponding to the high energy substep is presented in figure 7.3, in more detail. No additional substeps or features are discernible in the semi-log isotherms. The lower temperature isotherms of figure 7.1 were not measured at low enough coverage or with a sufficient number of data points to discern if such features exist at those temperatures. It would be interesting to see if additional substeps would appear in the high binding energy substep for low temperature and low coverage isotherms of noble gases adsorbed on open carbon nanohorns.

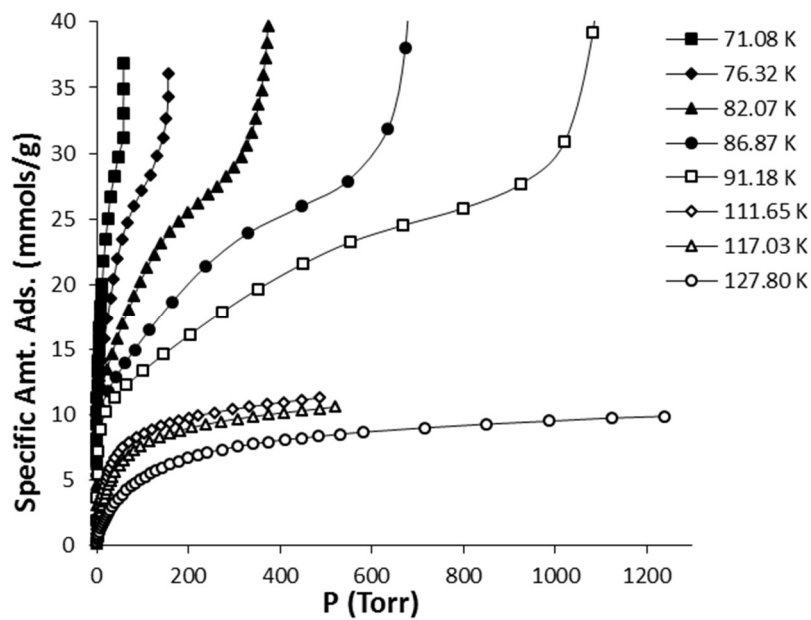


Figure 7.2: Linear isotherms of Ar adsorbed on opened dahlia-like SWCNH aggregates

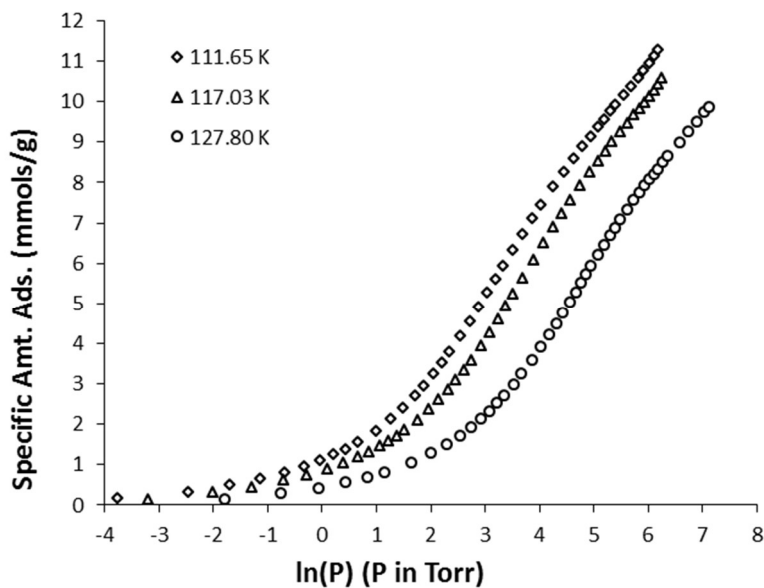


Figure 7.3: The three highest temperature isotherms from figure 7.1, in more detail.

7.4 Effective Specific Surface Area

Figure 7.4 demonstrates the Point-B (a), and BET (b), methods for determining the effective monolayer capacity of this system. The isotherm at 82.07 K was used in both cases. Given that the critical temperature for argon is 151 K, a temperature of 82.07 K corresponds to a relative temperature of about 0.54. The value used for the area per argon atom adsorbed was 13.2 m²/g [56]. The Point-B method yields a value for the effective monolayer of 13 mmols/g leading to a calculated value for the ESSA of 1033 m²/g. The BET linear plot gives a value of the effective monolayer of 15.7 mmols/g which leads to an ESSA of 1248 m²/g. The discrepancy of almost 20% between the two methods indicates the limitations of treating a porous sorbent as planar.

Favoring the Point-B calculated value for the ESSA of 1033 m²/g shows a favorable comparison to the previous study of Ne and CO₂ adsorption on open nanohorn aggregates [66]. As stated in section 4.2, the ESSAs reported for Ne and CO₂ on open nanohorns are 1077, and 850 m²/g, respectively. Argon, being intermediate in size between the two should give a value of ESSA that is also intermediate, which it does.

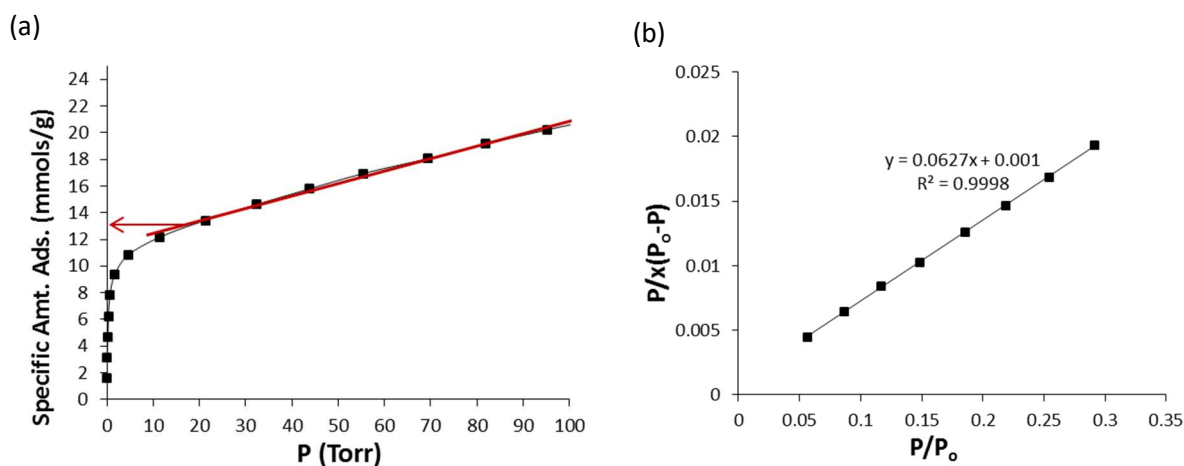


Figure 7.4: Effective monolayer capacity using data from the isotherm at 82.07 K ($T/T_c = 0.54$).

(a) Point-B Method (13 mmols/g, 1033 m²/g)

(b) BET linear plot. (15.7 mmols/g, 1248 m²/g, $c = 64$)

7.5 Isosteric Heat of Adsorption

The isosteric heat for Ar-ONH is shown in figure 7.5. Three plateau regions can easily be identified in the plot. The plateau from 3 to 13 mmols/g with an isosteric heat value of 115 meV corresponds to adsorption in the interstitial and intra-nanohorn pores, while the plateau from 15 to 27 mmols/g with an isosteric heat value of about 95 meV corresponds to adsorption on the interior and exterior surfaces. The plateau at 35 mmols/g and beyond corresponds to the heat of deposition for argon. The value determined here for the deposition is between 80 and 84 meV, while the value obtained from reference for this quantity is 79 meV [88].

The isosteric heat for argon adsorbed on graphitized carbon black extrapolated to zero coverage is about 102 meV (2.3 kcal/mole) [89]. This value is lower than the values calculated here for argon-ONH for the higher binding energy pores, and is similar to the value found for the lower binding energy surfaces. This makes sense given that the porous regions are going to have more carbon atoms attracting the adsorbate relative to a flat graphitic surface and will thus give rise to a higher isosteric heat. The surfaces (both inner and exterior) will show either a slightly higher, or slightly lower binding energy than flat graphite due to the either convex or concave curvature. Presumably, the combination of these two effects from the curved surfaces somewhat cancel out in the calculation and result in an isosteric heat that is similar to that found for argon on graphitized carbon black

On graphitized carbon black [89], it was speculated that the isosteric heat of argon initially increases because the adsorbed argon atoms increase the attraction between the vapor and the surface. This effect is noticeable because the surface of the graphitized carbon black substrate used in that study was energetically homogeneous. In the present case, the highest value of the isosteric heat at the lowest coverages for Ar-ONH is a result of adsorption in the narrowest region of the pores and in any structural defects that are present in the substrate. These regions get filled quite rapidly as coverage increases, hence the sharp drop before the first plateau.

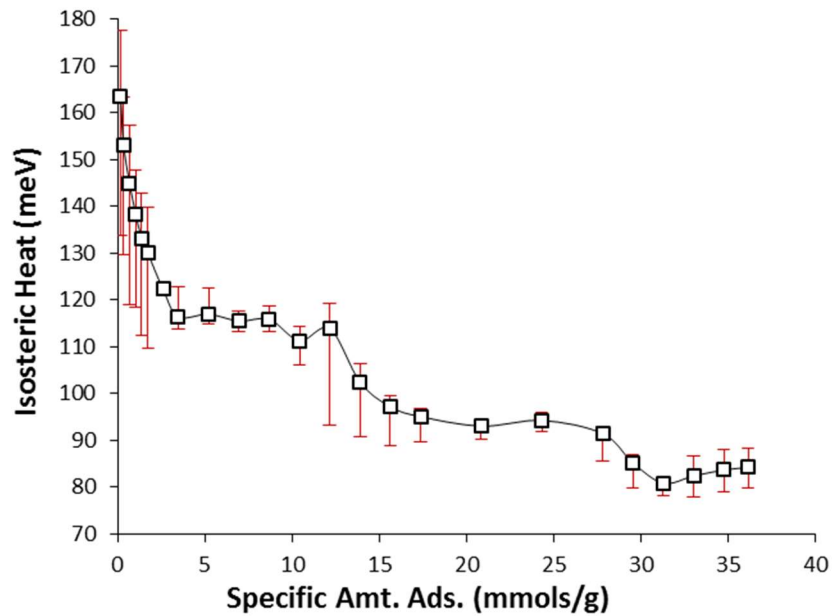


Figure 7.5: Isothermic heat as a function of coverage for Ar-ONH

The $\ln(P)$ vs $1/T$ plots in figure 7.6 show the number of isotherms used in the calculation of some of the data points of the isothermic heat of figure 7.5. The largest uncertainties on the order of 30 meV indicated by the error bars of figure 7.5 at the lowest coverages are a result of only three isotherms being measured in that region. Large uncertainties also seem to correspond to sloping regions in the isothermic heat plot in between the plateaus. The values corresponding to solid bulk formation contain uncertainties on the order of 8 to 10 meV which is again a result of only three isotherms being measured in that range. Even though a total of five isotherms were measured at saturation, only the three lowest isotherms are in the temperature range corresponding to solid formation. If the bulk value of the heat of condensation is measured for the two isotherms that reached saturation at temperatures above the triple point, a value of 74.7 meV is obtained.

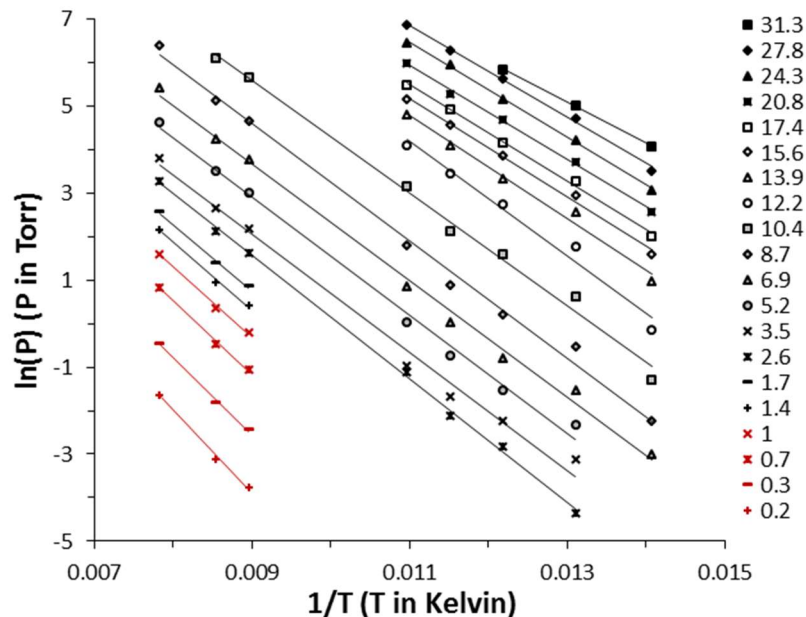


Figure 7.6: Natural logarithm of equilibrium pressure vs the inverse of temperature. Each line is at a constant coverage, shown on the right in the legend in mmols/g.

7.6 Kinetics of Adsorption

A fractional uptake of 0.999 was chosen to analyze the adsorption kinetics for this system. The results are displayed in figure 7.7. The fractional uptake is close enough to one to correspond well with equilibrium, which means that the kinetic data in figure 7.7 are essentially the equilibrium kinetics. For reasons previously discussed, finding the time at which equilibrium is reached can include too much noise to extract meaningful trends in the data, which is the case here. The trends in the kinetic data of figure 7.7 correspond to those which occur for adsorption of spherical adsorbates on planar substrates; as coverage and pressure increase for a given isotherm, the wait time decreases and as isotherm temperature increases for a given coverage, wait times also decrease.

Looking more closely at figure 7.7, a gentle plateau is discernible in the data for the isotherms at 76 and 82 K from about 4.5 to 7 mmols/g, which are coverages spanned by the high binding energy substeps of the corresponding isotherms of figure 7.1 and also by the first plateau region of the isosteric

heat plot of figure 7.5. However, this gentle plateau in the kinetic data is not present for the isotherms at higher temperatures. Perhaps at low enough pressures, groups of similar binding energy sites will result in similar wait times

The wait times for the four lowest temperature isotherms of figure 7.7 reach a minimum value of about 5 minutes at coverages of about 10 to 14 mmols/g. These coverages correspond roughly to the region in the isotherms of figure 7.1 intermediate between the two substeps where the effective monolayer is completed, and is also roughly intermediate between the first two plateaus in the isosteric heat plot of figure 7.4. After reaching this minimum value, the wait time stays essentially constant through the higher coverage substep all the way through to saturation.

The kinetic trends for the three higher temperature isotherms at 111, 117, and 127 K are similar, overall. The very steep drop in time in the low coverage regime from 0 up to 2 or so mmols/g corresponds to the region before the high energy substep of figure 7.1 and to the region of steep drop in the isosteric heat of figure 7.5, at low coverage. The kinetic plot for 111 K then smoothly approaches a minimum value of about 3 minutes at around a coverage of 6 mmols/g.

For the sake of comparisons, Figure 7.8a shows an isotherm at 23.3 K for neon adsorbed on oxidized carbon nanohorns (Ne-ONH), which was calculated from the same data set used for reference [66], as well as the isotherm for Ar-ONH at 76.32 K reproduced from figure 7.1. The substeps for Ne-ONH have the same interpretation as they do for Ar-ONH: the high binding energy substep at low coverage corresponds to adsorption in the interstitial and intra-nanohorn pores while the lower binding energy substep at higher coverage corresponds to adsorption on the inner and outer surfaces.

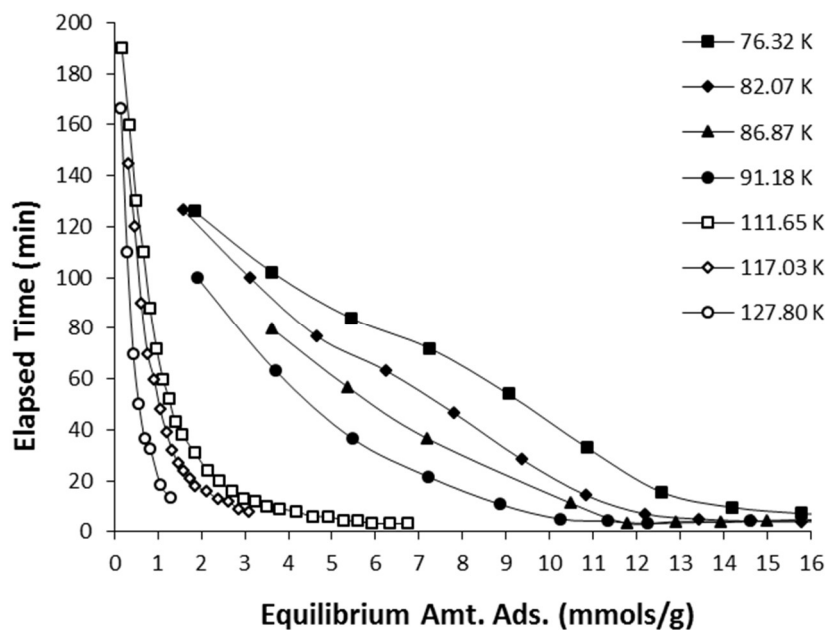


Figure 7.7: Time to reach $\theta = 0.999$ for points along select isotherms as functions of equilibrium coverage.

Figure 7.8b displays the adsorption kinetics for Ne-ONH using a fractional coverage of $\theta=0.999$ for four of the isotherms from reference [66]. The overall shape of the kinetic plots are very similar to those of figure 7.7; at the lower temperatures there is a sharp decrease followed by a plateau in the coverage range of the high binding energy sites, followed by a sharp decrease to the minimum at roughly the coverages corresponding to the region in between the two binding energy sites (near one effective monolayer). The plateau is progressively smoothed out as temperature increases and has disappeared entirely by a temperature of 35 K which, again, is a similar trend to figure 7.7.

The critical temperature for neon is 44.5 K [66], which means that the isotherm kinetic plots of figure 7.8b occur at a relative temperature range of 0.47 to 0.9. The relative temperature range spanned by the data in figure 7.7 for Ar-ONH is from 0.5 to 0.85. Thus, the kinetic data shown are at similar relative temperature ranges for both systems. This is also true of the two isotherms of figure 7.8a which,

again, occur at similar relative temperatures. Although the neon isotherm spans a larger specific coverage range due to its smaller size, the pressures at which each substep in the respective isotherms occur are similar; the high binding energy substep is at a $\ln(P)$ value of about -3 while the lower binding energy substep is at a $\ln(P)$ value of about 3.5 in both cases.

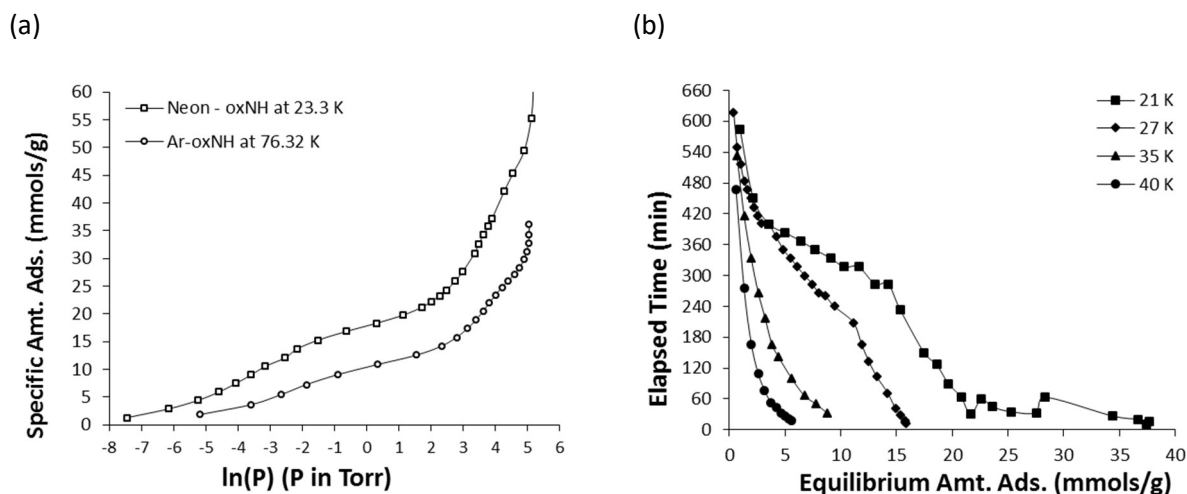


Figure 7.8: Neon data

(a) Isotherm of neon adsorbed on oxidized (opened) dahlia-like nanohorn aggregates at approximately 23.3 K compared to an isotherm of argon from figure 7.1.

(b) Kinetics for neon on opened nanohorns; elapsed time indicates the time to reach a fractional uptake of $\theta=0.999$ for all points plotted.

The primary difference between the kinetic results of figures 7.8b and 7.7 is the magnitude of the wait times at corresponding features in the isotherms. For instance, the time to reach $\theta=0.999$ at the gentle plateau corresponding to high binding energy sites for Ar-ONH is approximately 80 minutes while the corresponding wait time for Ne-ONH is approximately 300 to 400 minutes. The wait times in general are greater for Ne-ONH than they are for Ar-ONH. This is somewhat unexpected in light of a study that has been conducted in our lab comparing the kinetics of adsorption for argon and CF_4 adsorbed on the same sample of chemically opened nanohorns [90]. Wait times for CF_4 are greater than for argon at

corresponding isotherm features and relative temperatures and it was argued in that paper that the reason for this difference is that CF_4 is the larger adsorbate and therefore has more difficulty accessing the interior porous regions through holes in the nanohorns.

Because the substeps are occurring at similar pressures in figure 7.8a, it is likely that the ratio of binding energy to temperature are similar for both Ar-ONH and Ne-ONH. The differences in binding energy and temperature can't be used to explain the difference in wait times. If the binding energies were the cause of the difference, we would expect to see shorter wait times for neon since it has a smaller binding energy (see equation 2.14), which is not what the data shows. Additionally, since we are comparing wait times at corresponding features in the isotherms (the high binding energy substep, for instance) the difference in wait times is likely also not caused by differences in the fractional coverage of equation 2.14, since they are comparable.

If the size difference between neon and argon is the reason that neon adsorption involves longer wait times, it seems possible that it is partly because neon is accessing small diameter microporous regions deep in the nanohorn aggregates that are not accessible by argon. In such a case where the pore is just large enough to allow guest particles to enter, diffusion is an activated process (see equation 2.17). It's been shown [36] [91] that activated diffusion processes can greatly slow down adsorption kinetics when the adsorbate diameter is similar to the pore diameter. It's also been shown experimentally that neon wait times can exceed those of argon during high pressure and temperature (supercritical) adsorption on carbon molecular sieves [92]. The reason for longer wait times for neon in that paper was attributed, at least in part, to activated diffusion for neon when entering the small micropores of the carbon molecular sieve. The activation energy for argon was too high for it to adsorb in the same micropores as neon which had a slightly lower activation energy. The comparison is cautious, however, since the experimental conditions of that paper are at higher pressures and

temperatures and with a different carbon material as the adsorbent, but it demonstrates in principle that smaller adsorbates can have slower kinetics under certain conditions.

It would be interesting to determine how other noble gas adsorbates (such as Xe, or Kr) on opened nanohorn aggregates would compare kinetically to the current data sets of Ne and Ar.

CHAPTER 8

O₂ ADSORPTION ON ZEOLITIC IMIDAZOLATE FRAMEWORK-8

8.1 Introduction

Simulated and experimental oxygen isotherms have been measured with ZIF-8 as the adsorbent in reference [70]. In that study, two isotherms were measured at 77.3 and 90.2 K using an automated sorption analyzer with low temperatures attained using baths of liquid N₂ and Ar, respectively. An extra substep was identified in the isotherm data and was attributed to the increased accessible surface area following the gate opening process of the ZIF-8 framework. Given that the isotherms were measured at temperatures corresponding to cryogenic liquid, the temperature range is somewhat limited. The purpose of the current work was to extend the number of isotherms and the temperature range over which the O₂ – ZIF-8 system was measured to investigate the temperature dependence of the gate opening transition.

8.2 Experimental Details

0.1893 grams of powdered ZIF-8 [93] was loaded into a stainless steel cell sealed with a copper gasket. It was then heated under vacuum to a temperature of 170° C for a period of about 24 hours. After the heating and subsequent cooling to room temperature, the cell was sealed off and transferred to the experimental adsorption setup without exposing the ZIF-8 to air.

8.3 Isotherms

The isotherms of Oxygen adsorbed on ZIF-8 (O_2 – ZIF-8) are presented in figures 8.1 and 8.2. Seven isotherms were measured between the temperatures of 62 and 93 K. The triple point and critical point temperatures for O_2 are 54.33 and 154.58 K [94], respectively. As a result, the vertical substeps at the highest coverages correspond to formation of bulk liquid oxygen in coexistence with the gas.

Two other substeps are present in most of the isotherms in figure 8.1. The lower coverage substep at approximately 5 to 15 mmols/g corresponds to adsorption of oxygen on ZIF-8 AP (O_2 – ZIF-8 AP). The mid coverage substep at roughly 18 to 21 mmols/g for all but the highest temperature isotherm corresponds to adsorption of oxygen on ZIF-8 HP (O_2 – ZIF-8 HP). The increased uptake is a result of the gate-opening (G.O.) process and the increased effective surface area that then becomes accessible by the adsorbate is comparable to the oxygen isotherms in reference [70].

Looking more closely at the G.O. related substep shows that it gets closer and closer to the saturation step as temperature increases. For the 89 K isotherm the substep is barely discernible and has disappeared entirely for the 93 K isotherm. This is not necessarily an indication that the G.O. process would not occur at and beyond temperatures of roughly 93 K for oxygen adsorption, just that saturated vapor pressure is reached first. If more isotherms were to be measured at even lower temperatures, it's possible that the extra substep would also disappear as it blends into the substep corresponding to the AP structure. The pressures at lower temperatures than 62 K were too low for our setup to accurately measure for the present experiment however, so such isotherms were not attained.

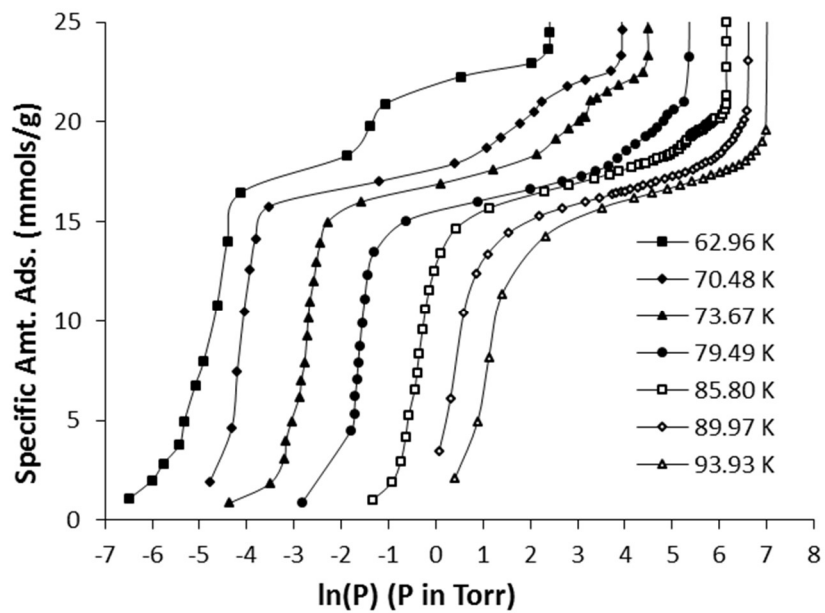


Figure 8.1: Semi-log plots of isotherms of oxygen adsorbed on ZIF-8

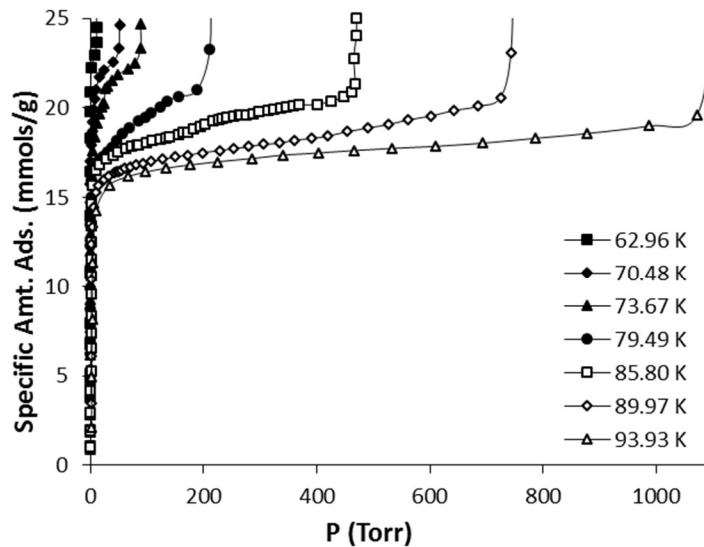


Figure 8.2: Linear plots of isotherms of oxygen adsorbed on ZIF-8. The isotherms here are of Type I, indicating microporosity.

8.4 Effective Specific Surface Area

Figure 8.3 shows the Point-B and BET methods for obtaining the effective monolayer capacity using the isotherm data at 62.96 K. Given that the linear isotherm fits well the Type I archetype, the “knee” is very sharp and the location of Point-B is clearly discernible as can be seen in figure 8.3a. The Point-B method yields an effective monolayer capacity of about 22 mmols/g while the BET linear plot method yields a value of 18.9 mmols/g. The area per molecule of O₂ on the surface of graphite obtained from [95] of 12.5 Å²/molecule. From this, the ESSA for ZIF-8 was calculated to be 1421 m²/g from the BET linear plot method and 1656 m²/g from the Point-B method.

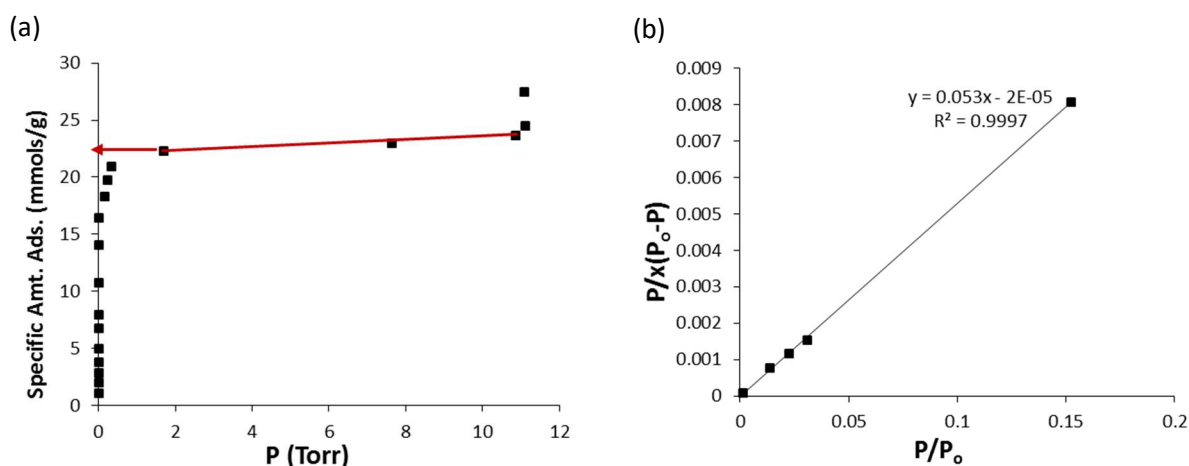


Figure 8.3: Isotherm data at 62.96 K used to determine the effective monolayer capacity for the O₂ – ZIF-8 system ($T/T_c = 0.41$).

(a) Point-B method (22 mmols/g, 1656 m²/g)

(b) BET linear plot method (18.9 mmols/g, 1421 m²/g)

The value of the effective monolayer capacity obtained from the Point-B method is higher than the coverage corresponding to the gate opening substep of the 62.96 K isotherm. As a result, the ESSA value of 1656 m²/g includes the effective surface area that becomes available after the transition. On

the other hand, the BET method yields an effective monolayer capacity just below the coverage corresponding to the gate opening substep, and therefore the value of 1421 m²/g does not include the extra effective surface area that becomes available after the structural transition. The discrepancy between the two is not surprising considering that neither the BET nor the Point-B methods are meant to deal with flexible frameworks.

8.5 Isothermic Heat of Adsorption

In figure 8.4a is the plot of isosteric heat vs. coverage for this system. Most notable is the rather large peak which reaches a maximum value of about 167 meV at 16 mmols/g. The coverage at this peak coincides roughly with the beginning of the substep corresponding to gate opening in the isotherms of figure 8.1. At coverages from 5 to 10 mmols/g, the isosteric heat is relatively constant at 115 meV. At and beyond 24 mmols/g, bulk liquid saturation is attained at a value of about 76 meV. The reported value for the heat of condensation of O₂ is 70.7 meV [94] which is within 7 % of our measured value.

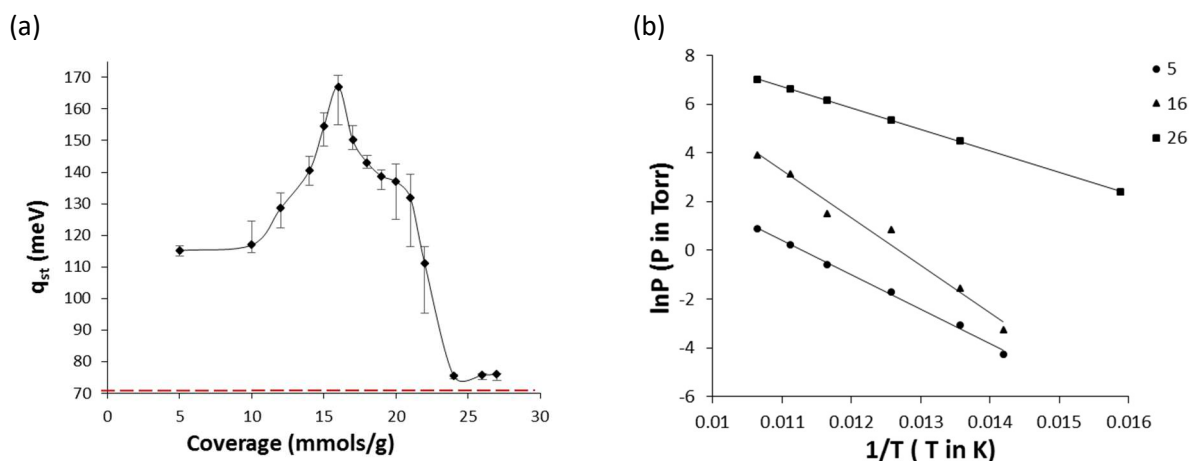


Figure 8.4: Oxygen Data

(a) Isothermic Heat of Adsorption vs. coverage in mmols/g. Red dashed line indicates the heat of condensation for O₂.

(b) $\ln P$ vs $1/T$ plots for selected coverages which are given in the legend at the upper right in mmols/g.

A form of the Clausius-Clapeyron equation (equation 2.8) can be used to obtain an estimate of the heat of the structural transition for the O₂ – ZIF-8 system. This has been done previously for adsorption in other gate opening MOFs [96], and the rationale in that reference for such a procedure is that Clausius-Clapeyron relations exist in both 2D and 3D and that an adsorbed film is intermediate between those two extremes. A film transition should thus be explained by a Clausius-Clapeyron equation. An additional assumption in that same reference is that the total heat of adsorption during the gate opening transition (ΔH_{GO}) is a combination of the heat of structural transition ($\Delta H_{trans.}$) plus the heat of adsorption for the extra adsorption sites that become available during the transition (which in this case is ΔH_{HP} where HP refers to the ZIF-8 HP structure). This is summarized in the following equation:

$$\Delta H_{GO} = \Delta H_{trans.} + \Delta H_{HP} \quad (8.1)$$

With regards to the current data set, what this means is that we can get an estimate for the heat of the structural transition from the data of figure 8.4a. A further assumption that we must make is that the adsorption sites of the ZIF-8 HP structure have a similar heat of adsorption as the adsorption sites of the ZIF-8 AP structure, which are roughly 115 meV in figure 8.4a. The maximum height of the peak is about 167 meV, which we can substitute for ΔH_{GO} in equation 8.1. This gives a value for the heat of structural transition of approximately 47 ± 10 meV. The uncertainty is a result of considering the error bars of figure 8.4, which are obtained in the manner previously described in section 3.6.

It appears from figure 8.4b that the line corresponding to the gate opening transition at 16 mmols/g will intersect the line corresponding to bulk saturation (26 mmols/g) at temperatures higher than those explored in this study. Similarly, that same line will intersect the line corresponding to 5 mmols/g at temperatures lower than those explored here. The outcome of this is that the gate opening substep will likely disappear at temperature above roughly 93 K and somewhat below roughly 62 K as

has been mentioned in section 8.3. Plotting the $\ln P$ vs $1/T$ lines in this way provides a method for predicting the temperature range at which the extra gate opening related substep will appear in the isotherms. For instance, if the lines at 16 and 5 mmols/g are extended to higher temperature, they will intersect at a temperature of approximately 61 K. If isotherms of oxygen on ZIF-8 were measured at that temperature and lower, it is likely that no gate opening related substep would appear.

8.6 Kinetics of Adsorption

Linear driving force plots for a few select points from the 70.48 K isotherm are presented in figure 8.5. Figure 8.5a includes points in the coverage range below that of the gate opening substep. It can be seen that the rate of adsorption increases as coverage increases. This is the same trend that would be expected for the case of spherical adsorbates on planar substrates, which has been discussed previously. Figure 8.5b includes points corresponding to the coverage range of the gate opening related substep. For points 13 and 14 it can be seen that they have an inflection roughly around the 45 to 60 minute mark, after which the rate of uptake greatly slows down. The rate constant (k) for point 13 after the 60 minute mark is 0.006 1/min which will be compared to CO_2 – ZIF-8. Hints of this behavior can be seen for the other points, but not nearly as dramatically. It seems likely that this slowing down of the kinetics is related to the structural transition in some way. The isotherms of figure 8.2 are of Type I indicating microporosity. Micropores can present a situation where diffusion is greatly slowed down if the pore width is similar to adsorbate size and this can have an effect on the adsorption kinetics in which wait times are greatly increased [36] [91]. If, during or after the gate opening, many adsorption sites suddenly become available in the ZIF-8 HP structure, it seems plausible that accessing these new sites in the micropores might take longer than accessing sites immediately prior to gate opening.

Kinetic results are summarized for three isotherms in figure 8.6 which shows the wait times for two different fractional coverages (0.99 and 0.997) obtained from LDF plots for three temperatures from the full data set of figure 8.1. Up until the coverage corresponding to gate opening, the trends are similar to the case for adsorption of spherical adsorbates on planar surfaces as discussed in section 2.5. However, the kinetics show a very pronounced non-monotonicity in the coverage region corresponding to the gate opening transition (about 22 mmols/g) for the two lowest temperatures at a fractional coverage of 0.997 (figure 8.5b). The non-monotonicity is much less pronounced at around 18 or 20 mmols/g for the isotherm at 93 K, which also exhibits a much less pronounced gate opening substep in the isotherm of figure 8.1 at that temperature. At a fractional coverage of 0.99 (figure 8.6a), the non-monotonicity is not as apparent for any of the isotherms. There is a slight bump in the 70.48, and 93.93 K isotherms at a coverage of about 20 mmols/g which could also be associated with gate opening.

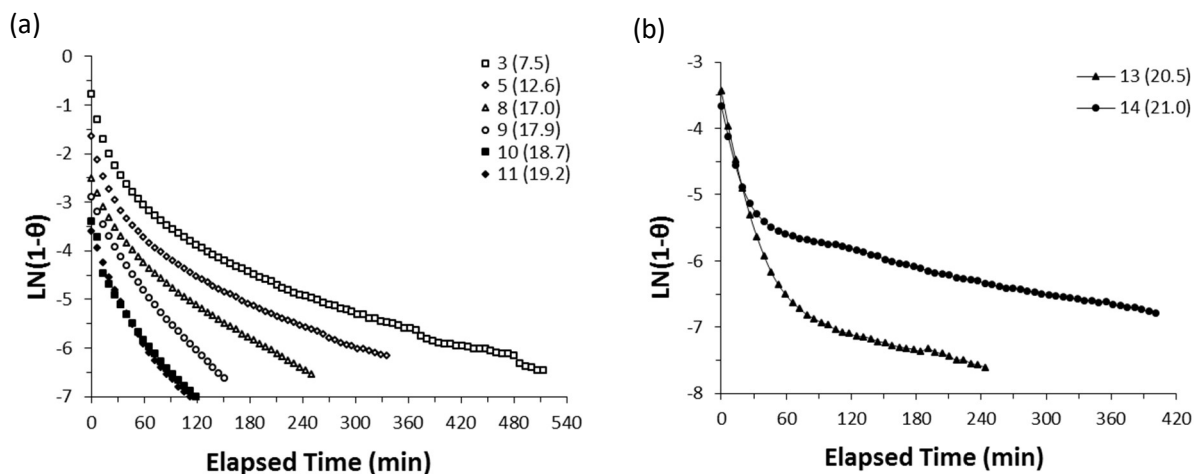


Figure 8.5: Linear Driving Force plots for select points along the 70.48 K isotherm. The point numbers corresponding to the isotherm in figure 8.1 (with coverage in parentheses in mmols/g) are given in the legend. Only every 20th point is presented in each plot for clarity.

- (a) Points at coverages below the gate opening related substep
- (b) Points in the coverage range of the gate opening related substep

Presumably, gate opening doesn't have an effect on the adsorption kinetics until each dose of gas in the gate opening region gets very close to the equilibrium coverage. This can be seen more explicitly by looking at figure 8.5b again. The inflection that was described two paragraphs ago for point number 14 at 21 mmols/g doesn't occur until after an LDF value of -5.5 which corresponds to a fractional uptake of 0.995. At lower fractional uptakes, the LDF plots for points 13 and 14 would fit well in figure 8.5a which showed faster kinetics as coverage increased. It's not until *after* the inflections in figure 8.5b that the non-monotonicity is noticeable, particularly for point 14.

It seems there are two different regimes in the kinetics here. For the first 45 to 60 minutes, the kinetics become faster as coverage is increased in a manner similar to that of spherical adsorbates on planar substrates. This is a common trend. Then after the 45 to 60 minute mark, for certain points in the coverage region corresponding to gate opening, the kinetics slow down as the effects of gate opening become more important in determining the rate of uptake than the effects of increasing isotherm pressure. A similar situation arises for the other isotherms of figure 8.1 which show the gate opening substep, although the 70.48 K isotherm was the focus here.

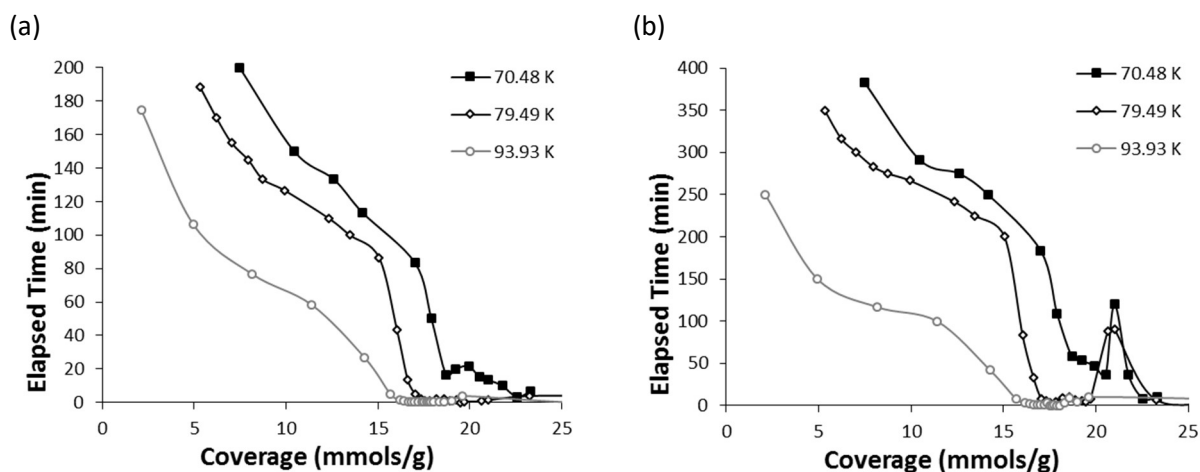


Figure 8.6: Kinetics of Adsorption for points along select isotherms for O_2 – ZIF-8. For the sake of clarity, only three isotherms were chosen to be displayed.

(a) Time vs. equilibrium coverage for 0.99 fractional uptake for each point

(b) Time vs. equilibrium coverage for 0.997 fractional uptake for each point

CHAPTER 9

CO₂ ADSORPTION ON ZEOLITIC IMIDAZOLATE FRAMEWORK-8

9.1 Introduction

As mentioned in section 5.1, metal organic frameworks are one of the key materials being considered as potential solid adsorbents in many carbon capture applications. Strategies to improve capacity, selectivity, and heats of adsorption for MOF sorbents include activation of open metal sites, and tailoring of the structure via pre-synthetic modification of the organic ligands, and post-synthetic functionalization [1].

Molecular dynamics simulations, have shown that gate opening occurs for the CO₂-ZIF-8 system at high pressure [97]. By contrast, experimental isotherms for CO₂-ZIF-8 do not show an additional substep related to gate opening for this system [97]. In Chapter 8 it was shown that the gate opening related substep for O₂-ZIF-8 disappears at temperatures at and greater than about 93 K, and would also likely disappear at temperatures below about 61 K. It's possible that for the case of the CO₂-ZIF-8 system, the temperature range over which the experimental isotherms have been measured thus far in the literature is simply outside of the range that would show the additional substep. This is motivation for further study to extend the range over which isotherms have been measured for the CO₂-ZIF-8 adsorption system, which has been done in the current study.

9.2 Experimental Details

The sample used was 0.1876 grams of powdered ZIF-8 [93]. It was heated to a temperature of 170° C for roughly 24 hours in a high vacuum environment prior to the adsorption experiment which served to activate the ZIF-8. It was then sealed and transferred in vacuum to the experimental chamber.

9.3 Isotherms

Ten adsorption isotherms for the CO₂ – ZIF-8 system are reported in figure 9.1 at temperatures from 133 K to 237 K. All these isotherms with the exception of the ones at 217 and 237 K are lower than the triple point temperature of 216.59 K [80]. The saturated vapor pressure was reached for all but the two highest temperature isotherms. Saturation corresponds to the formation of solid carbon dioxide in the experimental cell. This occurred at a coverage of roughly 12.5 mmols/g and is indicated by the sudden vertical step. At lower coverages from about 2 to 8 or 9 mmols/g, a quasi-vertical substep is present which corresponds to adsorption on the ZIF-8 AP structure.

There's no clear indication of any substeps in any of the isotherms of figure 9.1. Though slightly disappointing, this does not by itself mean that gate opening is not occurring upon sorption of CO₂, just that the isotherms aren't particularly sensitive to the structural transition. The other possibility is that the temperature range over which such a gate-opening sensitive substep would appear in the isotherms is either above or below the range measured here. We, however, do not believe that this is the case. Evidence suggesting that gate-opening might be occurring in this temperature range is presented in the following sections.

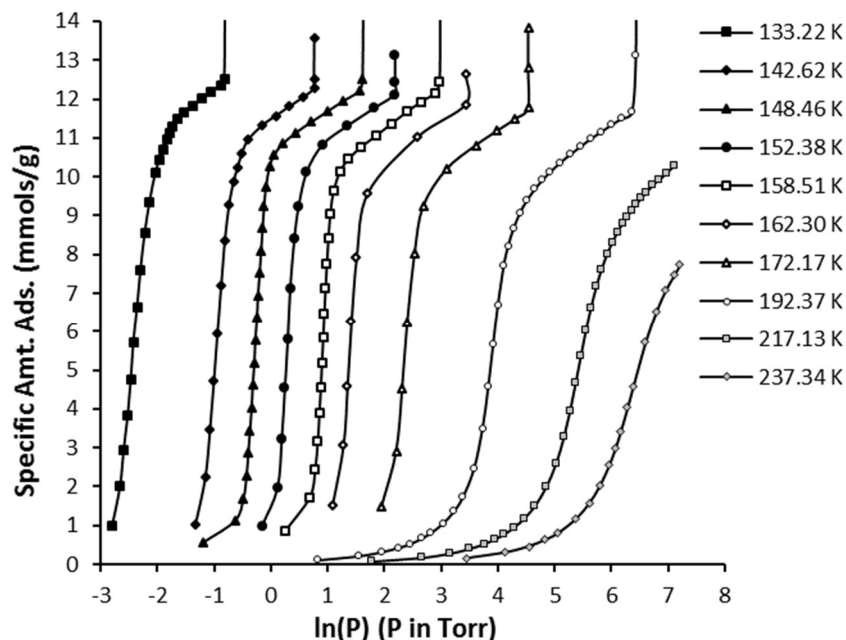


Figure 9.1: Semi-log plots of isotherms of Carbon Dioxide adsorbed on ZIF-8

9.4 Effective Specific Surface Area

The ESSA was calculated from effective monolayer capacities determined from both the Point-B and BET methods as shown in figure 9.2. There is a rather large, and perhaps alarming, discrepancy between the two methods. The Point-B method yields an effective monolayer capacity of 11.3 mmols/g which corresponds to an ESSA of 1068 m²/g. This value seems reasonable when compared to the ESSA determined from isotherms of Xenon on ZIF-8 of 1278 m²/g [73].

The BET method, however, yields an effective monolayer of 6.7 mmols/g which corresponds to an ESSA of 633 m²/g which is a 41% difference relative to the value from the Point-B method. As can be seen in figure 9.2b the BET linear plot isn't really linear within the typical P/P₀ range of .05 to .35. The four data points that were used for the calculation are indicated by the line and corresponding linear fit equation and R² value in figure 9.2b. A similar situation arises for other temperatures; the BET method is likely not suitable for surface area determinations for this system. The discrepancy between the ESSA

values determined from the two methods for the O₂ – ZIF-8 system in section 8.4 is much smaller: about 14%. Given that the substrate is the same and both particles are small and linear, it seems plausible that the larger discrepancy for the CO₂ – ZIF-8 system is related to the permanent quadrupole moment of the carbon dioxide molecule and increased adsorbate-adsorbate interactions.

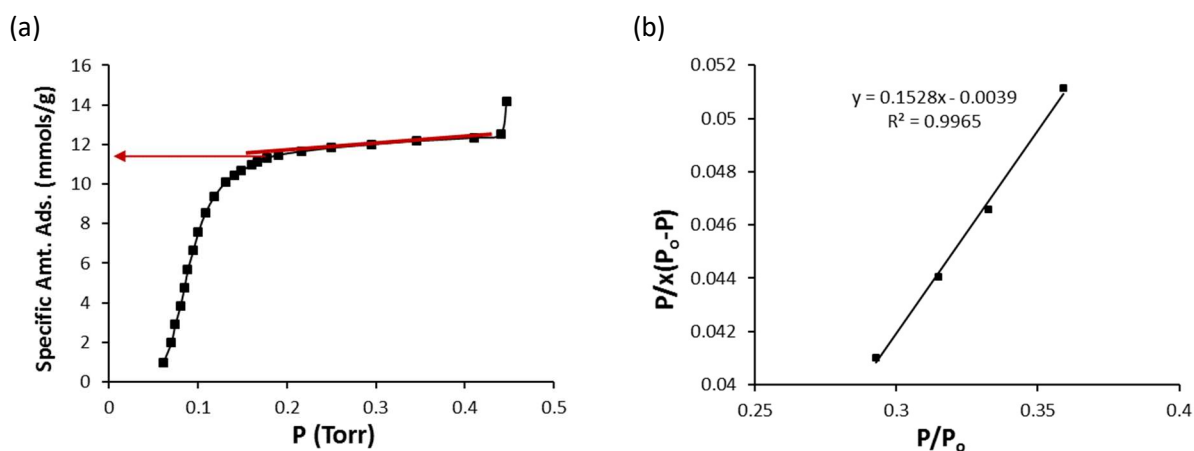


Figure 9.2: Isotherm data at 133.22 K ($T/T_c = 0.44$) used to determine the effective monolayer capacity for the CO₂ – ZIF-8 system.

(a) Point-B method (11.3 mmols/g, 1068 sq.m/g)

(b) BET linear plot method (6.7 mmols/g, 633 sq. m/g)

9.5 Isothermic Heat of Adsorption

Isosteric heat vs. coverage is presented in figure 9.3a. There are three regions of interest. Up until about 10 mmols/g the trend rises steadily because as more carbon dioxide adsorbs onto the surface, the attraction between film and vapor grows. This is a result of adsorbate-adsorbate interactions due to the large quadrupole moment of CO₂. Essentially, the molecules in the vapor are more attracted to the molecules which have already been adsorbed than they are to the bare surface, hence the steadily rising heat of adsorption. This is similar to the CO₂-SWCNT system. At a coverage of about 13 mmols/g and beyond, bulk saturation with the formation of solid CO₂ is evidenced by the

measurement of the heat of sublimation. The value measured here for the heat of sublimation is 270 meV which correspond very well with the value reported from NIST of 272.52 meV.

In the coverage range between 10 and 13 mmols/g a clear peak is present in the data. This peak is similar to that seen for the isosteric heat vs. coverage plot of O₂ on ZIF-8 in figure 8.4a. For O₂ on ZIF-8, the isosteric heat peak occurred at coverages similar to the gate opening related substep in the isotherms. Here, for CO₂ on ZIF-8, there is no such substep in the isotherms but the isosteric heat peak can still plausibly be attributed to the sorption induced gate opening effect of ZIF-8.

Following the same line of reasoning from section 8.5, we can get an estimation for the heat of structural transition of ZIF-8 during the adsorption of CO₂ using equation 8.1. ΔH_{GO} is the height of the peak, which in this case is 300 meV. For ΔH_{HP} we can once again make the assumption that the heat of adsorption for the sites that become available as a result of the structural transition is equal to the heat of adsorption for the ZIF-8 AP structure. The blue line in figure 9.3 is interpolated between the isosteric heat values at 8 and 13 mmols/g. It is essentially a best guess at what the isosteric heat would be if the peak were not present. At 11.5 mmols/g, the value of isosteric heat indicated by the interpolation is about 260 meV, which will be taken as ΔH_{HP} for the sake of calculating ΔH_{GO} . This gives an upper bound for the value for ΔH_{GO} of 40 meV. The value of the upper bounds for the heat of the structural transition induced by oxygen (section 8.5) and xenon [73] adsorption are 47 ± 10 meV and 36 meV, respectively. These values all compare favorably, but it should be noted these values are all approximations.

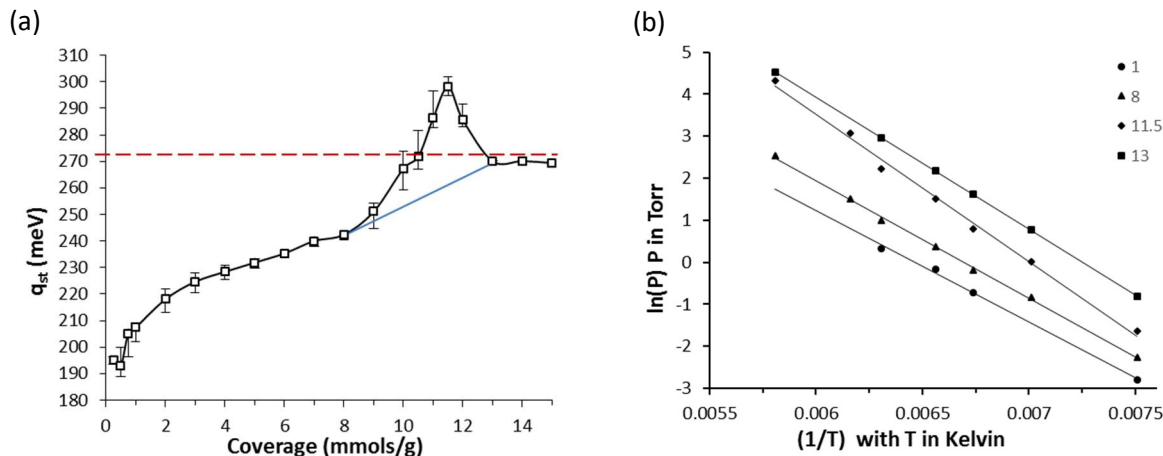


Figure 9.3:

(a) Isosteric Heat of Adsorption in meV vs. coverage in mmols/g. Red dashed line indicates the heat of sublimation for CO_2 . Blue line is an interpolation between the q_{st} values at 8 and 13 mmols/g.

(b) $\ln(P)$ vs $1/T$ plots for selected coverages which are given in the legend at the upper right in mmols/g.

$\ln(P)$ vs. $1/T$ plots from the Clausius Clayperon equation are shown in figure 9.3b for the coverages 1, 8, 11.5, and 13 mmols/g. The line which yields the peak in figure 9.4a is seen to be steeper than the lines representing the heats of adsorption at the other coverages, as would be expected if gate-opening were taking place at that coverage. This can be compared to the case for oxygen in section 8.5, and a similar analysis can be done in the present case to get an estimate of the range of temperatures over which the structural transition might be represented in the data. The line in figure 9.3b representing the peak will intersect the line at bulk saturation (13 mmols/g) at approximately 204 K. Similarly, the line representing the peak will intersect the line at the coverage immediately prior to the peak (8 mmols/g) at approximately 121 K. Two of the isotherms in figure 9.1 are above 204 K but unfortunately, due to limitations of the experimental setup, were not measured all the way to saturation. It would be interesting to measure adsorption isotherms for the CO_2 – ZIF-8 system all the way to saturation outside of this range of temperatures (that is, above 204 K and below 121 K) to see what effects, if any, it would have on the experimentally measured data.

9.6 Kinetics of Adsorption

Figure 9.4a shows linear driving force plots for select pressure plots for the isotherm at 133 K. A slight lengthening for the plot for point 16 at 11.3 mmols/g (open circles) can be discerned where it crosses over the plot for point 11. It's possible that this slight slowing down of the kinetics is related to the gate opening transition in the same way as for the case of O₂-ZIF-8 although here it is much less pronounced. The rate constant, k , calculated for point 16 from 20 to 70 minutes is 0.04 1/min. Comparing this to the rate constant calculated for O₂-ZIF-8 of 0.006 1/min in the gate opening region reveals that CO₂ is adsorbing much faster.

The kinetics are summarized as usual in figure 9.4b for a fractional coverage of 0.995 which is essentially equilibrium. There is a clear non-monotonicity at around 10 to 11 mmols/g indicated by the red arrow for the three temperatures shown. This is not that dissimilar to the non-monotonicity in the O₂ kinetic data of figure 8.6b with the exception that in the present case of CO₂, the non-monotonicity is not as pronounced. I attempted to find wait times at different fractional coverages for CO₂ but at no fractional coverage did the kinetic trends show a non-monotonicity any more pronounced than that shown in figure 9.4b. Although the CO₂ kinetics are much less sensitive to the effects of gate opening than the O₂ kinetics, it's still plausible that the non-monotonicity is related to gate opening given that it occurs in the region of the peak in the isosteric heat and appears similarly at multiple temperatures.

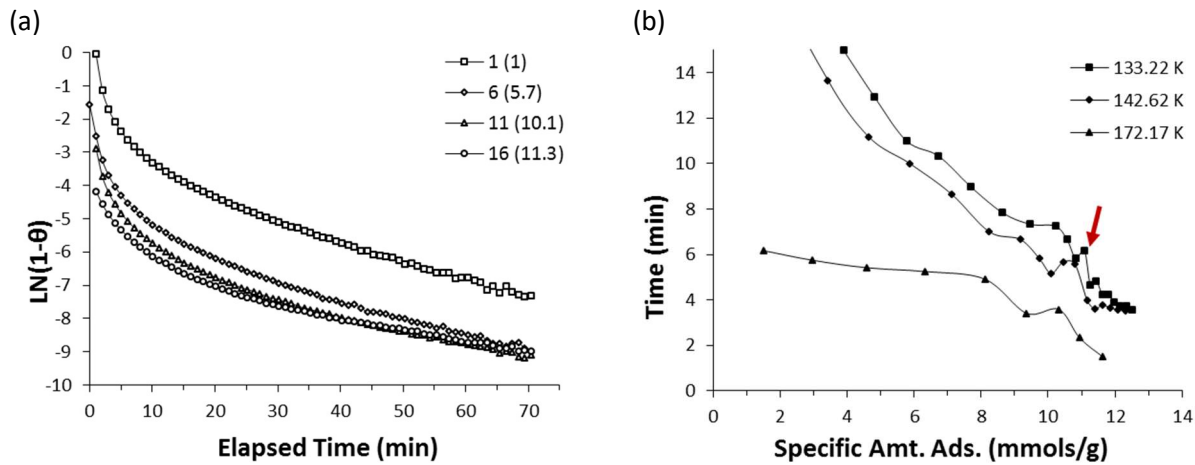


Figure 9.4: Kinetics of adsorption data for select points along the 133.22 K isotherm.

- (a) LDF model plots. The point numbers correspond to the isotherm in figure 9.1 (with equilibrium coverage in parentheses in mmols/g) in the legend.
- (b) Time to reach fractional coverage of 0.995 for three of the temperatures. The arrow indicates a region of non-monotonicity which may correspond to the gate opening effect.

CHAPTER 10

SUMMARY AND CONCLUSIONS

Many adsorbate-substrate combinations were explored in this dissertation. CO₂ – SWCNT was a system with a linear adsorbate possessing a permanent polarity adsorbing on a substrate with shallow linear pores and convex surface sites. Ethane-NH was a system with a linear molecule adsorbing on a very porous substrate with conical pores, convex surface sites, and a somewhat high surface area. Ar-ONH was a system with a spherical atom adsorbing on a highly porous substrate with two different sets of conical porous regions, and convex/concave surface sites. O₂ – ZIF-8 and CO₂ – ZIF-8 were both systems with relatively small, linear (with CO₂ possessing its permanent quadrupole moment) molecules adsorbing on a flexible microporous framework material with a very high effective surface area.

10.1 Isotherms

The isotherm types for all linear isotherms (coverage vs. P) from this dissertation, and c values for some of the isotherms, are summarized in table 10.1. Adsorption studies on the carbon materials (nanotubes and nanohorns) all yielded Type II isotherms. As stated in chapter 1, a Type II isotherm corresponds to theoretical multilayer adsorption on a planar substrate which lacks stepwise behavior due to the assumption in the BET theory that all layers after the first have an isosteric heat equal to the heat of condensation for the gas being used. Of course, none of the carbon materials used here as substrates were planar. The fact that they revealed Type II isotherms is likely a result of the inhomogeneity of binding energies felt by the adsorbates. This inhomogeneity effectively destroys any chance that the adsorbate will form in a stepwise behavior and thus the linear isotherms smoothly approach saturation after the *effective* monolayer is completed. The c values of table 10.1 are consistent

with the Type II isotherm designations. Evidently, according to the BET theory, these are all strongly binding systems. Otherwise they would show up as Type III isotherms with no sharp bend, and would have much lower c values.

Table 10.1: Linear isotherm types based on IUPAC designations for all systems and c values for some systems used in this dissertation. Temperature scaled relative to the critical temperature is shown in parentheses next to the c values.

System	Isotherm Type	c value (T_r)
CO ₂ - SWCNT	Type II	55 (0.52)
Ethane – NH	Type II	93 (0.54)
Ar - oNH	Type II	64 (0.54)
O ₂ – ZIF-8	Type I	-
CO ₂ – ZIF-8	Type I	-

For the two studies on ZIF-8, linear isotherms are of Type I which indicates microporosity. No c values are reported for these two studies in table 10.1 because the BET linear plot intercept is negative and the calculation of c is not reliable. An interesting difference between the linear isotherms of O₂ and CO₂ on ZIF-8 is the derivative of the isotherm (equation 2.13) in the Henry’s Law regime. For O₂, the derivative of the isotherm is an average of about 1300 mmols/gTorr for the isotherm at a reduced temperature of 0.41 while for CO₂ it is only 178 mmols/gTorr at a reduced temperature of 0.44. Essentially, the O₂ isotherm is much steeper in the Henry’s Law regime than CO₂. This type of behavior in the Henry’s Law regime was noted by [70], when comparing O₂ and Ar adsorption on ZIF-8 to CO, and N₂. The steeper slope for O₂ and Ar was attributed to the smaller sizes of those two adsorbates relative to CO and N₂ which showed much more gradual adsorption. Effects due to polarity were ruled out as an explanation for the differing slopes in the low loading region based on computer simulations. It seems likely that something similar is happening for the current data sets of O₂ and CO₂ on ZIF-8 although effects due to the relatively large quadrupole moment of CO₂ can’t be necessarily ruled out. Oxygen,

being the smaller adsorbate, packs more efficiently into the ZIF-8 AP structure than CO₂ which leads to a steeper low loading region in the isotherm.

Semi-logarithmic isotherms (coverage vs. $\ln P$) for all the systems studied showed a wide variety of features. Since none of the substrates used were planar, substeps in the isotherms corresponded to groups of adsorption sites of similar binding energy. The degree to which substeps appeared discernible in the data depended largely on the morphological details of the adsorbent as well as the physical characteristics of the adsorbate. Isotherms of Ar-ONH for instance displayed very well defined substeps even though the potential felt by the argon adsorbate varies along the length of the conical regions of the open nanohorn aggregates. This is likely because argon is a relatively small, spherical adsorbate which packs efficiently into the pores. Smearing of isotherm substeps occurred to a large extent for both CO₂ – SWCNT and Ethane – NH. For Ethane – NH this was due to adsorbate linearity and the highly porous and energetic inhomogeneity of the nanohorn aggregates. For CO₂ – SWCNT, the smearing of the isotherms was largely due to the permanent quadrupole moment of CO₂ since the SWCNT substrate displays fairly well defined binding energy sites in other cases. Many factors related to the physical properties of the adsorbate and the morphological details of the substrate can conspire to destroy substeps in adsorption isotherms, as was seen in this dissertation.

For O₂-ZIF-8, the substep corresponding to the AP structure was well defined while the substep corresponding to the gate opening and subsequent availability of adsorption sites in the HP structure was discernible to a degree which depended on the temperature of the isotherm. For CO₂-ZIF-8, only the substep corresponding to adsorption on the AP structure was discernible while at no temperature did there appear a gate-opening related substep even though evidence suggests that gate-opening is likely taking place.

10.2 Effective Specific Surface Area

Surface area measurement for all the systems studied here are summarized in Table 10.2. The smallest discrepancy between the two methods used (Point-B and BET) occurs for the CO₂-SWCNT and Ethane-NH systems. These are also the two systems with the highest low coverage binding energy which likely occurs from adsorption in interstitial defects of the carbon material used as adsorbents. The largest deviation comes from the CO₂-ZIF-8 system.

Table 10.2: Summary of surface area measurements. Monolayer data is in mmols/g and ESSA data is in m²/g. Data used in the calculations were taken from isotherms in the range of roughly 0.4 to 0.54 T/T_c.

System	Point-B Method		BET Method		% Discrepancy
	Monolayer	ESSA	Monolayer	ESSA	
CO ₂ -SWCNT	3.7	351	3.5	327	6.8
Ethane-NH	3	380	2.9	367	3.4
Ar-ONH	13	1033	15.7	1248	20
O ₂ -ZIF-8	22	1656	18.9	1421	14
CO ₂ -ZIF-8	11.3	1068	6.7	633	41

10.3 Isothermic Heat

All of the isothermic heat plots are shown in figure 10.1 a and b. For the sake of comprehensibility, the plots have been scaled by their respective effective monolayers (as determined by the Point-B method) so they all fit on the same graph without sacrificing legibility.

The isothermic heat plots for CO₂-SWCNTs, Ethane-NH, and Ar-ONH in figure 10.1a all display a maximum at the lowest coverages measured. This is likely due to defects in the carbon materials which give rise to high binding energy adsorption sites. Ethane-NH and Ar-ONH also both show plateaus in their respective plots corresponding to groups of adsorption sites of similar binding energy. For Ar-ONH

the plateaus are quite clear and level whereas for Ethane-NH the lower coverage plateau is smeared out. This is due to a combination of the linearity of ethane and the spread in energy of the conical regions of the nanohorn aggregate. Argon packs in much more efficiently and therefore shows a more uniform binding energy. CO₂-SWCNTs on the other hand, does not show any clear plateaus and in fact displays an atypical “u” shape, the minimum of which has been attributed to the increased adsorbate-adsorbate interactions resulting from its permanent quadrupole moment. In effect, the polarity and linearity of adsorbate molecules, as well as a large spread in binding energies due to the morphological details of the substrate wash out not only features in the isotherms, but also features in the isosteric heat vs. coverage plots.

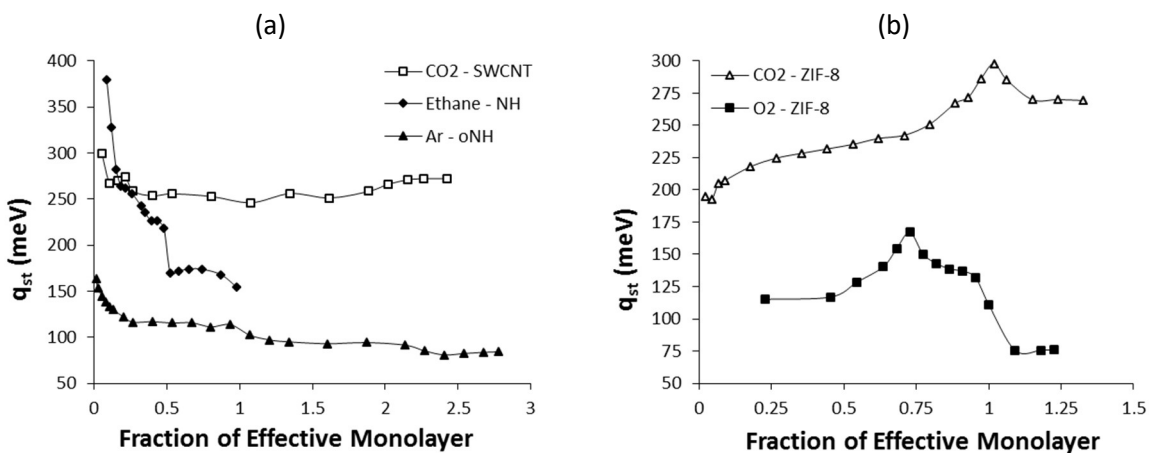


Figure 10.1: Isosteric heat vs. fraction of the effective monolayer capacity for all of the studies in this dissertation.

- (a) Carbon based sorbents
- (b) ZIF-8 sorbent

The isosteric heat plots for O₂-ZIF-8, and CO₂-ZIF-8 in figure 10.1b are quite different given the peak which results from the gate opening process for O₂ and potentially for CO₂. In addition, there is no maximum at low coverage for either study as there are in the studies involving the carbon-based materials. This is perhaps due to a more uniform structure of ZIF-8 with fewer defects when compared

to the carbon materials. It could be argued that for the case of O₂-ZIF-8, the coverage at which the isosteric heat was calculated simply isn't low enough to see a low coverage maximum. However, it's quite clear for the case of CO₂-ZIF-8 that there is no maximum in the isosteric in the low coverage regime. With the exception of the peak, nowhere is the isosteric heat higher than the latent heat of condensation, which is not uncommon for CO₂ adsorption.

10.4 Kinetics of Adsorption

I analyzed the kinetics for all the studies in this dissertation by making use of the linear driving force model. One way of looking at the kinetics is by analyzing the shape of the linear driving force plots. With the exception of the region corresponding to equilibrium ($\theta = 1$) where the data becomes too noisy and sensitive to have any physical meaning, the rate of mass uptake with respect to time is reflected in the slope of the plots of $\ln(1-\theta)$ vs. time. Larger negative slope corresponds to a faster pressure drop while smaller negative slope corresponds to a slower pressure drop. Therefore, while the linear driving force model doesn't always provide a good fit to the data, it is nonetheless very useful in clearly showing how the rates of sorption change with respect to time or isotherm equilibrium coverage and fractional uptake, and to plot multiple data sets in one comprehensible graph. A change in the slope (or k-value) of the $\ln(1-\theta)$ vs. time plots is likely indicative of a change in the mechanism controlling the rate of adsorption even if the fundamental details of such a mechanism aren't always clear.

In all of the systems, there is an initial sharp drop in the $\ln(1-\theta)$ vs. time plots which corresponds to the initial opening of valve 3 and the subsequent drop in pressure as the gas in the dosing volume expands into the cell. In all cases, the rate of this expansion induced pressure drop increases as the vapor pressure increases. After this initial sharp drop, the rate of pressure drop is associated with sorption and/or other physical processes related to the adsorbate/substrate interactions or adsorbate

re-orientation. In some cases, the rate of uptake simply increases as pressure increases for the entire coverage range. In other cases, the rate of uptake does the opposite and decreases as pressure increases. The rate controlling mechanism can also change for certain fractional uptake and isotherm coverages. These trends were plotted for all the systems studied here.

For CO₂-SWCNTs and Ethane-NHs, the kinetics of adsorption were shown to be fairly complex with changes in the trends noted and speculated on in their respective sections. The Ar-ONH kinetics show wait times which decrease (at a fractional uptake arbitrarily close to 1) as equilibrium pressure increases whether temperature or coverage is held constant. This is likely a result of increasing vapor pressure. Also, the magnitude of the wait times for Ar-ONH are much shorter than those for CO₂-SWCNTs and Ethane-NH. The reasons for this are likely that Ar is a smaller, spherical atom without any sort of appreciable polarity and therefore packs more efficiently than the linear adsorbates. A direct comparison of wait times between these systems is difficult since the substrates are all different, however. For that reason, in part, Ar-ONH was compared to data from a previous experiment of the smaller Neon adsorbing on a different sample of oxidized (open) nanohorns where I hypothesized that the longer wait times for neon depended in part on the presence of small micropores only accessible by neon and not argon.

The kinetic results for CO₂-ZIF-8 and O₂-ZIF-8 were primarily focused on the effect of gate opening. Plots of $\ln(1-\theta)$ vs. time for these two systems (figures 8.5 and 9.4a) after a certain coverage have an inflection and “cross over” the plots at lower coverage. For O₂-ZIF-8, the sudden slowing down of the kinetics is likely related to gate opening since it occurs at the same coverage as the extra substep in the isotherms. The rate constants were compared for both systems and revealed that CO₂ adsorbs much faster on/in ZIF-8 in the gate opening region relative to O₂ at similar reduced temperatures. This is another cautious comparison, however, since the pressure range is different for each system in the isotherm region where the k values were calculated.

10.5 Concluding Remarks

The practical applications in science and engineering that depend in part on adsorption processes are numerous. Many of these applications have been mentioned (and some described to varying degrees) in relevant sections of this dissertation and include gas storage (sections 1.1 and 4.1), gas mixture separation (sections 1.1 and 6.1), chemical sensing (section 4.1), drug delivery (section 4.2), molecular filtration (section 4.1), molecular sieving (sections 4.2 and 7.6), and chemical catalysis (sections 4.2 and 4.3). Experimental studies of the physics of adsorption can be useful in determining the suitability of materials for certain applications such as those listed.

The focus of this dissertation was the thermodynamics and kinetics of adsorption and it is clear from trying to understand the data that those two topics should not be studied in isolation from each other. The attainment of equilibrium is an important requirement in attempting to make conclusive explanations of the thermodynamics of adsorption and conversely, the thermodynamic properties of the adsorbate will play a large part in the kinetics and the attainment of equilibrium. It is at times difficult to give a conclusive physical explanation for such behavior from purely experimental data although an attempt was made in the respective sections for all of the systems presented. One definite conclusion, however, is that when studying the adsorption kinetics, it is important to let the system come to equilibrium at every isotherm point rather than imposing an insufficient wait time which might give misleading kinetic *and* thermodynamic results. In many other studies of adsorption thermodynamics (some of which were cited throughout this dissertation), kinetic data is either absent entirely or only briefly mentioned. This certainly does not invalidate those studies, but it does highlight a void in the published research which could be filled by more thorough studies where adsorption thermodynamics and kinetics are presented together.

REFERENCES

- [1] M. Mohamedali, D. Nath, H. Ibrahim and A. Henni, "Chapter 6: Review of Recent Developments in CO₂ Capture Using Solid Materials: Metal Organic Frameworks," in *Greenhouse Gases*, Intech, 2016, pp. 115-154.
- [2] C.-H. Yu, C.-H. Hagan and C.-S. Tan, "A Review of CO₂ Capture by Absorption and Adsorption," *Aerosol and Air Quality Research*, vol. 12, pp. 745-769, 2012.
- [3] T. Duren, L. Sarkisox, O. M. Yaghi and R. Q. Snurr, "Design of New Materials for Methane Storage," *Langmuir*, vol. 20, pp. 2683-2689, 2004.
- [4] P. Jena, "Materials for Hydrogen Storage: Past, Present, and Future," *J. Phys. Chem. Lett.*, vol. 2, pp. 206-211, 2011.
- [5] R. T. Yang, *Gas separation by adsorption processes*, Boston: Butterworth Publishers, 1987.
- [6] P. Q. Liao, W. X. Zhang, J. P. Zhang and X. M. Chen, "Efficient Purification of Ethene by an Ethane-Trapping Metal-Organic Framework," *Nat. Commun.*, vol. 6, p. 8697, 2015.
- [7] M. Rafti, V. Krungleviciute and A. D. Migone, "Low-pressure experiments on Ar-CH₄ gaseous mixtures adsorption over exfoliated graphite: Evidence of kinetic selectivity shift," *Chem. Phys. Lett.*, vol. 554, pp. 67-71, 2012.
- [8] D. Banerjee, C. M. Simon, A. M. Plonka, R. K. Motkuri, J. Liu, X. Chen, B. Smit, J. B. Parise, M. Haranczyk and P. K. Thallapally, "Metal-organic framework with optimally selective xenon adsorption and separation," *Nature Comm.*, 2016.
- [9] N. M. Mubarak, E. C. Abdullah, N. S. Jayakumar and J. N. Sahu, "An Overview on Methods for the Production of Carbon Nanotubes," *J. Ind. Eng. Chem.*, vol. 20, pp. 1186-1197, 2014.
- [10] Y. Wang and J. T. W. Yeow, "A Review of Carbon Nanotubes-Based Gas Sensors," *Journal of Sensors*, 2009.
- [11] M. Yudasaka, S. Iijima and V. H. Crespi, "Single-Wall Carbon Nanohorns and Nanocones," *Topics Appl. Physics*, vol. 111, pp. 605-629, 2008.
- [12] K. Ajima, M. Yudasaka, T. Murakami, A. Maigne, K. Shiba and S. Iijima, "Carbon Nanohorns as Anticancer Drug Carriers," *Mol. Pharm.*, vol. 2, no. 6, pp. 475-480, 2005.
- [13] K. S. Park, Z. Ni, A. P. Cote, J. Y. Choi, R. Huang, F. J. Uribe-Romo, H. K. Chae, M. O'Keeffe and O. M. Yaghi, "Exceptional Chemical and Thermal Stability of Zeolitic Imidazolate Frameworks," *Proc. Natl. Acad. Sci.*, vol. 103, pp. 10186-10192, 2006.

- [14] L. W. Bruch, M. W. Cole and E. Zaremba, "Chapter 2: Interactions," in *Physical Adsorption: Forces and Phenomena*, Mineola, Dover Publications Inc., 2007.
- [15] L. W. Bruch, M. W. Cole and E. Zaremba, "Chapter 1: Monolayer Physics," in *Physical Adsorption: Forces and Phenomena*, Mineola, Dover Publications Inc., 2007.
- [16] J. G. Dash, "Chapter 2: The Atomic Basis of Adsorption," in *Films on Solid Surfaces*, New York, Academic Press Inc., 1975.
- [17] D. M. Ruthven, "Chapter 2: Physical Adsorption and the Characterization of Porous Adsorbents," in *Principles of Adsorption and Adsorption Processes*, New York, John Wiley & Sons Inc., 1984.
- [18] L. W. Bruch, M. W. Cole and E. Zaremba, "Chapter 4: Monolayer Films: Theoretical Context," in *Physical Adsorption: Forces and Phenomena*, Mineola, Dover Publications Inc., 2007.
- [19] J. G. Dash, "Chapter 5: Thermodynamics of Noninteracting Monolayers," in *Films on Solid Surfaces*, New York, Academic Press Inc., 1975.
- [20] S. J. Gregg and K. W. Sing, "Chapter 4: The Physical Adsorption of Gases by Microporous Solids," in *Adsorption, Surface Area and Porosity*, London, Academic Press, 1967.
- [21] S. Brunauer, P. H. Emmett and E. Teller, "Adsorption of Gases in Multimolecular Layers," vol. 60, no. 309-319, 1938.
- [22] S. J. Gregg and K. W. Sing, "Chapter 2: Physical Adsorption of Gases by Non-porous Solids," in *Adsorption, Surface Area and Porosity*, London, Academic Press, 1967.
- [23] J. G. Dash, "Chapter 9: Heterogeneous Films," in *Films on Solid Surfaces*, New York, Academic Press Inc., 1975.
- [24] S. J. Gregg and K. W. Sing, "Chapter 1: Introduction," in *Adsorption, Surface Area and Porosity*, London, Academic Press, 1967.
- [25] S. J. Gregg and K. W. Sing, "Chapter 3: The Physical Adsorption of Gases by Porous Solids," in *Adsorption, Surface Area and Porosity*, London, Academic Press, 1967.
- [26] J. G. Dash, "Chapter 4: The Statistical Thermodynamics of Physisorption," in *Films on Solid Surfaces*, New York, Academic Press Inc., 1975.
- [27] L. W. Bruch, M. W. Cole and E. Zaremba, "Appendix B," in *Physical Adsorption: Forces and Phenomena*, Mineola, Dover Publications Inc., 2007.
- [28] R. K. Pathria, "Chapter 5: Formulation of Quantum Statistics," in *Statistical Mechanics, 3rd Ed.*, Amsterdam, Elsevier, 2011.
- [29] R. Baierlein, "Chapter 7: The Chemical Potential," in *Thermal Physics*, Cambridge, Press Syndicate of the University of Cambridge, 1999.

- [30] S. J. Gregg and K. W. Sing, "Chapter 5: Methods Based on the Gibbs Adsorption Isotherm," in *Adsorption, Surface Area and Porosity*, London, Academic Press, 1967.
- [31] J. G. Dash and J. Ruvalds, "An Introduction to the Thermodynamics of Surfaces," in *Phase Transitions in Surface Films*, New York, Plenum Press, 1980.
- [32] R. Baierlein, "Chapter 12: Phase Equilibrium," in *Thermal Physics*, Cambridge, Press Syndicate of the University of Cambridge, 1999.
- [33] S. E. Weber, S. Talapatra, C. Journet, A. Zambano and A. D. Migone, "Determination of the binding energy of methane on single-walled carbon nanotube bundles," *Phys. Rev. B.*, vol. 61, no. 19, p. 151, 2000.
- [34] R. K. Pathria and P. D. Beale, "Chapter 4: The Grand Canonical Ensemble," in *Statistical Mechanics, 3rd Ed.*, Amsterdam, Elsevier, 2011.
- [35] J. G. Dash, "Chapter 7: Solid Phases Melting Phenomena," in *Films on Solid Surfaces*, New York, Academic Press, 1975.
- [36] J. T. Burde and M. M. Calbi, "Physisorption Kinetics in Carbon Nanotube Bundles," *J. Phys. Chem*, vol. 111, pp. 5057-5063, 2007.
- [37] D. S. Rawat, V. Krungleviciute, L. Heroux, M. Bulut, M. M. Calbi and A. D. Migone, "Dependence of Single-Walled Carbon Nanotube Adsorption Kinetics on Temperature and Binding Energy," *Langmuir*, vol. 24, pp. 13465-13469, 2008.
- [38] D. M. Ruthven, "Chapter 5: Diffusion in Porous Media," in *Principles of Adsorption and Adsorption Processes*, New York, John Wiley & Sons Inc., 1984.
- [39] S. Sircar and J. R. Hufton, "Why Does the Linear Driving Force Model for Adsorption Kinetics Work?," *Adsorption*, vol. 6, pp. 137-147, 2000.
- [40] D. M. Ruthven, "Chapter 6: Kinetics of Sorption in Batch Systems," in *Principles of Adsorption and Adsorption Processes*, New York, John Wiley Inc., 1984.
- [41] H. K. Chagger, F. E. Ndaji, M. L. Sykes and K. M. Thomas, "Kinetics of Adsorption and Diffusional Characteristics of Carbon Molecular Sieves," *Carbon*, vol. 33, no. 10, pp. 1405-1411, 1995.
- [42] E. H. Kennard, "Section 39," in *Kinetic Theory of Gases: With an Introduction to Statistical Mechanics, 1st Ed., 2nd Imp.*, New York, McGraw-Hill Book Company Inc., 1938.
- [43] E. H. Kennard, "Sections 184-186," in *Kinetic Theory of Gases: With an Introduction to Statistical Mechanics, 1st Ed., 2nd Imp.*, New York, McGraw-Hill Book Company Inc., 1938.
- [44] T. Takaishi and Y. Sensui, "Thermal Transpiration Effect of Hydrogen, Rare Gases and Methane," *Trans. Faraday Soc.*, vol. 59, pp. 2503-2514, 1963.

- [45] G. M. Thomson, "The Antoine Equation for Vapor-Pressure Data," Ethyl Corporation, Detroit, 1980.
- [46] P. J. Linstrom and W. G. Mallard, "Chemistry WebBook," NIST, 2016. [Online]. Available: <http://webbook.nist.gov/chemistry/>.
- [47] P. H. Emmett and S. J. Brunauer, "The Use of Low Temperature van der Waals Adsorption Isotherms in Determining the Surface Area of Iron Synthetic Ammonia Catalysts," *Am. Chem. Soc.*, vol. 59, pp. 1553-1564, 1937.
- [48] P. M. Ajayan and T. W. Ebbeson, "Nanometre-Size Tubes of Carbon," *Rep. Prog. Phys.*, vol. 60, pp. 1025-1062, 1997.
- [49] S. Iijima, "Helical Microtubules of Graphitic Carbon," *Nature*, vol. 354, pp. 56-58, 1991.
- [50] S. Iijima and T. Ichihashi, "Single-Shell Carbon Nanotubes of 1-mm Diameter," *Nature*, vol. 363, pp. 603-605, 1993.
- [51] A. D. Migone and S. Talapatra, "Gas Adsorption on Carbon Nanotubes," *Encycl. of Nanoscience and Nanotech*, vol. 3, pp. 749-767, 2004.
- [52] D. S. Rawat, L. Heroux, V. Krunglvičute and A. D. Migone, "Adsorption of Xenon on Purified HiPco Single Walled Carbon Nanotubes," *Langmuir*, vol. 22, pp. 234-238, 2006.
- [53] S. Talapatra, A. Z. Zambano, S. E. Weber and A. D. Migone, "Gases Do Not Adsorb on the Interstitial Channels of Closed-Ended Single-Walled Carbon Nanotube Bundles," *Phys. Rev. Lett.*, vol. 85, pp. 138-141, 2000.
- [54] S. Talapatra and A. D. Migone, "Existence of Novel Quasi-One-Dimensional Phases of Atoms Adsorbed on the Exterior Surface of Close-Ended Single Wall Nanotube Bundles," *Phys. Rev. Lett.*, vol. 87, 2001.
- [55] L. Heroux, V. Krunglvičute, M. M. Calbi and A. D. Migone, "CF₄ on Carbon Nanotubes: Physisorption on Grooves and External Surfaces," *J. Phys. Chem*, vol. 110, pp. 12597-12602, 2006.
- [56] V. Krunglvičute, L. Heroux, S. Talapatra and A. D. Migone, "Gas Adsorption on HiPco Nanotubes: Surface Area Determinations, and Neon Second Layer Data," *Nano Lett.*, vol. 4, no. 6, pp. 1133-1137, 2004.
- [57] M. Bienfait, P. Zeppenfeld, N. Dupont-Pavlovsky, M. Muris, M. R. Johnson, T. Wilson, M. DePies and O. E. Vilches, "Thermodynamic and Structure of Hydrogen, Methane, Argon, Oxygen, and Carbon Dioxide Adsorbed on Single-Wall Carbon Nanotube Bundles," *Phys. Rev. B.*, vol. 70, 2004.
- [58] D. S. Rawat, T. Furuhashi and A. D. Migone, "Adsorption Characteristics of Linear Alkanes Adsorbed on Purified HiPco Single-Walled Carbon Nanotubes," *J. Phys. Chem. C*, vol. 114, pp. 20173-20177, 2010.
- [59] D. S. Rawat, M. M. Calbi and A. D. Migone, "Equilibration Time: Kinetics of Gas Adsorption on

- Closed-and-Open Ended Single-Walled Carbon Nanotubes," *J. Phys. Chem. C*, vol. 111, pp. 12980-12986, 2007.
- [60] D. S. Rawat and A. D. Migone, "Non-Monotonic Kinetics of Alkane Adsorption on Single-Walled Carbon Nanotubes," *J. Phys. Chem. C*, vol. 116, pp. 975-979, 2012.
- [61] S. Iijima, M. Yudasaka, R. Yamada, S. Bandow, K. Suenaga, F. Kokai and K. Takahashi, "Nano-Aggregates of Single-Walled Graphitic Carbon Nano-Horns," *Chem. Phys. Lett.*, vol. 309, pp. 165-170, 1999.
- [62] D. Kasuya, M. Yudasaka, K. Takahashi, F. Kokai and S. Iijima, "Selective Production of Single-Wall Carbon Nanohorn Aggregates and Their Formation Mechanism," *J. Phys. Chem. B.*, vol. 106, pp. 4947-4951, 2002.
- [63] T. Azami, D. Kasuya, R. Yuge, M. Yudasaka, S. Iijima, T. Yoshitake and Y. Kubo, "Large-Scale Production of Single-Wall Carbon Nanohorns with High Purity," *J. Phys. Chem. C*, vol. 112, pp. 1330-1334, 2008.
- [64] J. Xu, M. Zhang, M. Nakamura, S. Iijima and M. Yudasaka, "Double Oxidation with Oxygen and Hydrogen Peroxide for Hole-Forming in Single Wall Carbon Nanohorns," *Appl. Phys. A*, vol. 100, pp. 379-383, 2010.
- [65] V. Krungleviciute, M. M. Calbi, J. A. Wagner and A. D. Migone, "Probing the Structure of Carbon Nanohorn Aggregates by Adsorbing Gases of Different Sizes," *J. Phys. Chem. C*, vol. 112, pp. 5742-5746, 2008.
- [66] V. Krungleviciute, C. A. Ziegler, S. R. Banjara, M. Yudasaka, S. Iijima and A. D. Migone, "Neon and CO₂ Adsorption on Open Carbon Nanohorns," *Langmuir*, vol. 29, pp. 9388-9397, 2013.
- [67] V. Krungleviciute, A. D. Migone, M. Yudasaka and S. Iijima, "CO₂ Adsorption on Dahlia-Like Carbon Nanohorns: Isothermic Heat and Surface Area Measurements," *J. Phys. Chem. C*, vol. 116, pp. 306-310, 2012.
- [68] O. M. Yaghi, M. O'Keeffe, N. W. Ockwig, H. K. Chae, M. Eddaoudi and J. Kim, "Reticular Synthesis and the Design of New Materials," *Nature*, vol. 423, pp. 705-714, 2003.
- [69] S. A. Moggach, T. D. Bennett and A. K. Cheetham, "The Effect of Pressure on ZIF-8: Increasing Pore Size with Pressure and the Formation of a High-Pressure Phase at 1.47 GPa," *Angew. Chem. Int. Ed.*, vol. 48, pp. 7087-7089, 2009.
- [70] C. O. Ania, E. Garcia-Perez, M. Haro, J. J. Gutierrez-Sevillano, T. Valdes-Solis, J. B. Parra and S. Calero, "Understanding Gas-Induced Structural Deformation of ZIF-8," *J. Phys. Chem. Lett.*, vol. 3, pp. 1159-1164, 2012.
- [71] L. Zhang, Z. Hu and J. Jiang, "Sorption-Induced Structural Transition of Zeolitic Imidazolate Framework-8: A Hybrid Molecular Simulation Study," *J. Am. Chem. Soc.*, vol. 135, pp. 3722-3728,

2013.

- [72] H. Tanaka, S. Ohsaki, S. Hiraide, D. Yamamoto, S. Watanabe and M. T. Miyahara, "Adsorption-Induced Structural Transition of ZIF-8: A Combined Experimental and Simulation Study," *J. Phys. Chem. C*, vol. 118, pp. 8445-8454, 2014.
- [73] D. Gallaba and A. D. Migone, "Evidence of Gate-Opening on Xenon Adsorption on ZIF-8: An Adsorption and Computer Simulation Study," *J. Phys. Chem. C*, vol. 120, pp. 16649-16657, 2016.
- [74] D. Fairen-Jimenez, R. Galvelis, A. Torrisi, A. D. Gellan, M. T. Wharmby, P. A. Wright, C. Mellot-Draznieks and T. Duren, "Flexibility and Swing Effect on the Adsorption of Energy-Related Gases on ZIF-8: Combined Experimental and Simulation Study," *Dalton Trans.*, vol. 41, pp. 10752-10762, 2012.
- [75] L. E. Drain, "Permanent Electric Quadrupole Moments of Molecules and Heats of Adsorption," *Trans. Faraday Soc.*, vol. 49, pp. 650-654, 1953.
- [76] A. Terlain and Y. Larher, "Phase Diagrams of Films of Linear Molecules with Large Quadrupole Moments (CO₂, N₂O₂, C₂N₂) Adsorbed on Graphite," *Surface Science*, vol. 125, pp. 304-311, 1983.
- [77] E. J. Bottani, V. Bakaev and W. Steele, "A Simulation/Experimental Study of the Thermodynamic Properties of Carbon Dioxide on Graphite," *Chem. Eng. Sci.*, vol. 49, pp. 2931-2939, 1994.
- [78] M. Cinke, J. Li, C. W. Bauschlicher Jr., A. Ricca and M. Meyyappan, "CO₂ Adsorption in Single-Walled Carbon Nanotubes," *Chem. Phys. Lett.*, vol. 376, pp. 761-766, 2003.
- [79] M. J. Bronikowski, P. A. Willis, D. T. Colbert, K. A. Smith and R. E. Smalley, "Gas-Phase Production of Carbon Single-Walled Nanotubes from Carbon Monoxide via the HiPco Process: A Parametric Study," *J. Vac. Sci. Technol. A*, vol. 19, no. 4, pp. 1800-1805, 2001.
- [80] P. J. Linstrom and W. G. Mallard, "Chemistry WebBook: Carbon Dioxide," NIST, 2016. [Online]. Available: <http://webbook.nist.gov/cgi/cbook.cgi?ID=C124389&Mask=4>.
- [81] D. S. Rawat and A. D. Migone, "Phases of Ethane Adsorbed on Purified HiPco Single-Walled Carbon Nanotubes," *Phys. Rev. B*, vol. 75, 2007.
- [82] L. W. Bruch, M. W. Cole and E. Zaremba, "Chapter 6: Monolayer Examples," in *Physical Adsorption: Forces and Phenomena*, Mineola, Dover Publications Inc., 1997.
- [83] P. J. Linstrom and W. G. Mallard, "Chemistry WebBook: Ethane," NIST, 2016. [Online]. Available: <http://webbook.nist.gov/cgi/cbook.cgi?ID=C74840&Mask=4#Thermo-Phase>.
- [84] B. A. Russell, A. D. Migone, J. Petucci, M. M. Calbi, M. Yudasaka and S. Iijima, "Ethane Adsorption on Aggregates of Dahlia-Like Nanohorns: Experiments and Computer Simulations," *Phys. Chem. Chem. Phys.*, vol. 18, pp. 15436-15446, 2016.
- [85] J.-M. Gay, J. Suzanne and R. Wang, "Phase Transitions, Thermodynamics, and Structural Analysis of

- Ethane Films Adsorbed on Graphite," *J. Chem. Soc., Faraday Trans.*, vol. 82, pp. 1669-1684, 1986.
- [86] "High Purity Gases and Gas Mixtures: Argon," Matheson, 2017. [Online]. Available: <http://www2.mathesongas.com/pdfs/products/Argon-Pure-Gas.pdf>.
- [87] S. M. Gatica, A. Nekhai and A. Scrivener, "Adsorption and Gas Separation of Molecules by Carbon Nanohorns," *Molecules*, vol. 21, p. 662, 2016.
- [88] "Gas Encyclopedia: Argon," Air Liquide, 2016. [Online]. Available: <https://encyclopedia.airliquide.com/argon>.
- [89] J. R. Sams, G. Constables and G. D. Halsey, "Adsorption of Argon on Graphitized Carbon Black: Surface Area, Heats and Entropies of Adsorption," *J. Phys. Chem*, vol. 66, no. 11, pp. 2154-2158, 1962.
- [90] B. A. Russell, P. Khanal, M. M. Calbi, M. Yudasaka, S. Iijima and A. D. Migone, "Sorption Kinetics on Open Carbon Nanohorn Aggregates: The Effect of Molecular Diameter," *Molecules*, vol. 21, p. 521, 2016.
- [91] J. M. Vann, S. L. Molnar and M. M. Calbi, "Equilibration Process During Gas Uptake Inside Narrow Pores," *Phys. Chem. Chem. Phys.*, vol. 17, pp. 13021-13027, 2015.
- [92] C. R. Reid, I. P. O'koye and K. M. Thomas, "Adsorption of Gases on Carbon Molecular Sieve Used for Air Separation. Spherical Adsorptives as Probes for Kinetic Selectivity," *Langmuir*, vol. 14, pp. 2415-2425, 1998.
- [93] "ZIF-8 Purchased as Basolite Z1200: Produced by BASF," Sigma-Aldrich, 2017. [Online]. Available: <http://www.sigmaaldrich.com/catalog/product/aldrich/691348?lang=en®ion=US>.
- [94] P. J. Linstrom and W. G. Mallard, "Chemistry WebBook: Oxygen," NIST, 2016. [Online]. Available: <http://webbook.nist.gov/cgi/cbook.cgi?ID=7782-44-7>.
- [95] M. F. Toney and S. C. Fain, "Low-Energy Electron Diffraction Study of Molecular Oxygen Physisorbed on Graphite," *Phys. Rev. B*, vol. 36, pp. 1248-1258, 1987.
- [96] S. Sircar, S. Pramanik, J. Li, M. W. Cole and A. D. Lueking, "Corresponding States Interpretation of Adsorption in Gate-Opening Metal-Organic Framework Cu(dhbc)2(4,4'-bpy)," *Journal of Colloid and Interface Science*, vol. 446, pp. 177-184, 2015.
- [97] T. Chokbunpiam, S. Fritzsche, C. Chmelik, J. Caro, W. Janke and S. Hannongbua, "Gate Opening Effect for Carbon Dioxide in ZIF-8 by Molecular Dynamics - Confirmed but at High CO₂ Pressure," *Chem. Phys. Lett.*, vol. 648, pp. 178-181, 2016.

VITA

Graduate School
Southern Illinois University

Brice A. Russell

Brussell85@outlook.com

Southern Illinois University Carbondale
Bachelor of Science, Physics, May 2011

Southern Illinois University Carbondale
Master of Science in Physics, December 2013

Special Honors and Awards:

Dissertation Research Assistantship Award

Dissertation Title:

An Experimental Study of the Effects of Substrate Porosity, Morphology, and Flexibility on the Equilibrium Thermodynamics and Kinetics of Adsorption for Atomic and Molecular Adsorbates

Major Professor: Aldo D. Migone

Publications:

B. Russell, J. Villaroel, K. Sapag, A. D. Migone, "O₂ Adsorption on ZIF-8: Temperature Dependence of the Gate-Opening Transition", *J. Phys. Chem. C.*, 2014, 118 (49), pp 28603-28608.

A. Albesa, B. Russell, J. L. Vicente, M. Rafti, "Low pressure equilibrium binary argon-methane mixture adsorption on exfoliated graphite: Experiments and simulations", *Chem. Phys. Lett.* 2016, 650, pp 130-137.

B. A. Russell, P. Khanal, M. M. Calbi, M. Yudasaka, S. Iijima, A. D. Migone, "Sorption Kinetics on Open Carbon Nanohorn Aggregates: The Effect of Molecular Diameter", *Molecules*, 2016, 21 (4), 521.

B. A. Russell, A. D. Migone, J. Petucci, M. M. Calbi, M. Yudasaka, S. Iijima, "Ethane Adsorption on Aggregates of Dahlia-Like Nanohorns: Experiments and Computer Simulations", *Phys. Chem. Chem. Phys.*, 2016, 18, 15436.

B. A. Russell, A. D. Migone, "Low temperature adsorption study of CO₂ in ZIF-8", *Micro. Meso. Mater.* 246, 2017, 178-185.